Reducing Particulate Matter Emissions from a Wood-Fired Hydronic Furnace: Computational Fluid Dynamics Modeling and Analysis

Paul Eric Glanville

A thesis submitted in partial fulfillment
of the requirements for the degree of

Master of Science in Mechanical Engineering

University of Washington

2008

Program Authorized to Offer Degree:
Mechanical Engineering

University of Washington
Graduate School

This is to certify that I have examined this copy of a master's thesis by

Paul Eric Glanville

and have found that it is complete and satisfactory in all respects,
and that any and all revisions required by the final
examining committee have been made

Committee Members:

_____
John C. Kramlich

_____
Michael J. Kirby

_____
James J. Riley

Date :_____

TABLE OF CONTENTS

Page

List of Figures iv

List of Tables viii

List of Commonly Used Variables x

Chapter 1: Introduction 1

1.1 Biomass at Home 3

1.2 Approaching the Problem 5

1.2.1 A Problem of Fluid Mechanics 6

Chapter 2: Theory and Literature Review 8

2.1 Wood Chemistry and Combustion 8

2.1.1 The Structure of Wood 9

2.1.2 Wood Chemistry 12

2.1.3 Wood Combustion 15

2.1.3.1 Heating and Drying Stage 16

2.1.3.2 Solid Phase Pyrolysis 17

2.1.3.3 Gas Phase Pyrolysis and Oxidation 22

2.1.3.4 Char Oxidation 26

2.2 Particulate Matter Formation and Oxidation 27

2.2.1 Particulate Matter Formation Theory 28

2.2.2 Particulate Matter Formation and Combustion Theory 30

2.3 Heat Transfer 32

2.4 Fluid Mechanics of Buoyancy-Driven Diffusion Flames 33

2.4.1 Buoyant Reacting Plumes: Theory & Experimental Evidence 34

2.4.2 Combustion Theory and Modeling 35

2.4.2.1 The Mixture Fraction Model 37

2.4.3 Turbulence Modeling of the Flow Field 40

2.4.3.1 The k-ε Model 43

2.4.3.2 Large Eddy Simulation 46

2.4.4 Turbulence-Chemistry Interaction 48

2.5 Final Remarks 51

Chapter 3: Data Acquisition 52
3.1 The Model 100 Outdoor Wood-fired Hydronic Heater 52
3.2 Testing Methods 54
3.2.1 Environmental Protection Agency Method 28 55
3.2.2 Experimental Data Acquisition 58
3.3 Discussion of Testing 60
3.3.1 Potential Sources of Error 61
Chapter 4: Benchmark Modeling and Analysis 62
4.1 Benchmark Testing 62
4.1.1 Initial Test Results 62
4.2 Data Analysis 65
4.2.1 System Stoichiometry and Air-to-Fuel Ratio 65
4.2.2 Energy Budget of the Model 100 67
4.2.3 Particulate Matter and CO Oxidation 72
4.3 CFD Modeling Decisions and Initialization 74
4.3.1 The FLUENT CFD Software Package 74
4.3.2 Convergence and Accuracy 75
4.3.3 Grid Development 77
4.3.4 Modeling Decisions 78
4.3.5 Boundary Conditions 80
4.3.6 Simulation Strategy 84
4.4 Benchmark Modeling Results 85
4.5 Discussion of Simulation Results 93
Chapter 5: Operational Modifications 103
5.1 Experimental Testing and CFD Simulation 103
5.1.1 Test Method, Simulation Details, and Boundary Conditions 103
5.1.2 Experimental Testing and Simulation Results 104
5.2 Certified Test Results and Analysis 108
5.2.1 Subsequent Cribwood Test Results 110
5.3 Operational Modifications Discussion 111

Chapter 6: Physical Modifications 113
6.1 Analysis of Alternative Designs 113
6.1.1 Tube Bank Redesign 114
6.1.2 Flow Obstructions 116
6.1.3 Secondary Air Jet Penetration 117
6.1.4 CO Oxidation 118
6.2 CFD Simulation of Redesigned Geometries 119
6.2.1 Outline of Experimental Geometries and Preliminary Simulation 120
6.2.1.1 Secondary Air Placement 120
6.2.1.2 Baffle Design 121
6.2.2 Simulation Setup and Results 124
6.3 Experimental Test Results and Analysis 128
6.4 Summary of Physical Modifications 132
Chapter 7: Concluding Remarks 133
7.1 Wood Combustion 133
7.2 CFD Simulation 133
7.3 OWHH PM Emission Reductions and Further Recommendations 134
7.4 Final Thoughts 135
Bibliography 137
Appendix A 141
Appendix B 143
B.1 Internal Heat Transfer 143
B.2 First Law Energy Budget 147
B.2.1 Heat of Reaction 148
B.2.2 Stack and Skin Losses 149
B.2.3 Heat of Drying and Pyrolysis 150
B.2.4 Heat to Internal Loop 151
Appendix C 152
Appendix D 153

LIST OF FIGURES

Figure Number Page

Figure 1.1 Typical OWHH Configuration 3

Figure 1.2 Material and Heat Flow Diagram of Wood Combustion 5

Figure 2.1 Microscopic Structure of Softwood Cells 10

Figure 2.2 Hardwood Structure Diagram 11

Figure 2.3 Microscopic Structure of Hardwood Cells 11

Figure 2.4 Cellulose Chemical Structure 12

Figure 2.5 Galactoglucumannan Structure 13

Figure 2.6 Glucuronoxylan Structure 13

Figure 2.7 One Proposed Structure of Lignin 14

Figure 2.8 Method 28 Test Crib Configuration 16

Figure 2.9 Movement of Combustion, Pyrolysis, and Drying Fronts 21

Figure 2.10 Adiabatic Flame Temperature versus Moisture Content 22

Figure 2.11 Aldehyde Diagram 23

Figure 2.12 Burn Rate for Volatile and Char Oxidation Dominated Stages 27

Figure 2.13 Image of Soot Particles 28

Figure 2.14 Breakdown of Organic Carbon by Mass 29

Figure 2.15 Pyrene Structure 30

Figure 2.16 Anthracene Structure 30

Figure 2.17 Schematic of Look-up Table Creation 49

Figure 3.1 Overall Schematic of Model 100 Operation 53

Figure 3.2 Typical Method 28 Test Crib 55

Figure 3.3 Typical Method 5G Particulate Sampling Train 57

Figure 3.4 Labels of Thermocouple Locations 58

Figure 3.5 Test Facility Photo Highlighting Orifice Meter 59

Figure 4.1 Firebox, Secondary, and Stack Temperatures of Initial Crib Test 63

Figure 4.2 Skin and Loop Temperatures of Initial Crib Test 63

Figure 4.3 Dry Gas Mole Fractions of CO_2 and CO of Initial Crib Test 64

Figure 4.4 Scale Reading of the Initial Crib Test 64
Figure 4.5 Phi and Measured PM Emissions Rate of Initial Crib Test 66
Figure 4.6 Calculated vs. Measured O_2 Stack Concentrations for Initial Crib Test 67
Figure 4.7 Calculated and Measured Heat Transfer to Internal Fluid Loop 68
Figure 4.8 Total Convective Heat Flux of Each Regime 69
Figure 4.9 Cartoon of the OWHH Energy Budget 70
Figure 4.10 Energy Budget of The Model 100 OWHH 70
Figure 4.11 Percent PM Oxidation versus Temperature and O_2 Concentration 73
Figure 4.12 Meshed Computational Domain of Model 100 77
Figure 4.13 Look Up Table for Runs 1, 2, 3, and 10 82
Figure 4.14 Look Up Table for Runs 4 82
Figure 4.15 Look Up Table for Runs 5 83
Figure 4.16 Look Up Table for Runs 6 83
Figure 4.17 Look Up Table for Runs 7 84
Figure 4.18 Internal Temperatures of Test Data vs. Simulations 86
Figure 4.19 Contours of Z_{mean} on Iso-surfaces of Scalar Dissipation = 0.01 [s^{-1}] for Run 7 87
Figure 4.20 Stack Species Concentrations of Test Data vs. Simulations 88
Figure 4.21 Run 8 Z-dir Contour of Reaction 1 Rate [kgmol/m^3 s] 90
Figure 4.22 Run 8 Z-dir Contour of Forward Reaction 4 Rate [kgmol/m^3 s] 90
Figure 4.23 Run 8 Z-dir Contour of Arrhenius Forward Reaction 4 Rate [kgmol/m^3 s] 91
Figure 4.24 Run 8 Z-dir Contour of Turbulent Forward Reaction 4 Rate [kgmol/m^3 s] 92
Figure 4.25 Run 4 Z-dir Contour of Vorticity Magnitude [s^{-1}] 94
Figure 4.26 Run 8 Z-dir Contour of Vorticity Magnitude [s^{-1}] 94
Figure 4.27 Run 10 Z-dir Contour of Soot Density [kg/m^3] 95
Figure 4.28: Contours of Temperature (K) on Iso-surface of Reaction 3 Rate = 0.001 [kgmol/m^3 s] for Run 8 97
Figure 4.29: Contours of Temperature (K) on Iso-surface of Reaction 3 Rate = 0.001 [kgmol/m^3 s] for Run 9 97
Figure 4.30 Pathlines for Run 8 98

Figure 4.31 Pathlines for Run 9 99
Figure 4.32 Run 9 Z-dir Contour of Subgrid Filter Length [in] 100
Figure 5.1 Scale Reading and Calculated Phi for Experimental Testing 105
Figure 5.2 Internal Temperatures for Experimental Testing 105
Figure 5.3 Dry Gas Mole Fractions of CO_2 and CO for Experimental Testing 106
Figure 5.4 Internal Temperatures of Experimental Test Data and Simulations vs. Phi 106
Figure 5.5 Mixture Fraction Variance Along Entrance to Tube Bank 107
Figure 5.6 Internal Temperatures for Certified Testing 108
Figure 5.7 Dry Gas Mole Fractions of CO_2 and CO and Phi for Certified Testing 109
Figure 5.8 Calculated and Measured Heat Transfer to Internal Fluid Loop 109
Figure 5.9 Energy Budget During Certified Testing 110
Figure 5.10 Phi During Cribwood Certified Test – Category 4 111
Figure 6.1 Internal Geometry of Model 100 114
Figur3 6.2 Heat Rate Delivered to Tube Bank vs. Surface Area 115
Figure 6.3 Photos of Original and Redesigned Tube Banks 116
Figure 6.4 Internal Geometry of Airbox and Baffles of Configuration 1 117
Figure 6.5 Jet Penetration For Various Exit Velocities 118
Figure 6.6 Time to Oxidize CO by Order of Magnitude 119
Figure 6.7 Pathlines & Particle Trajectories for Flush (Top) & Non-flush (Bottom) Gate Style Baffles 122
Figure 6.8 Rendering of Impaction Style Baffle Configuration 123
Figure 6.9 Internal Temperatures for Simulation of Physical Modifications 125
Figure 6.10 Dry Gas Mole Fraction for Simulations of Physical Modifications 126
Figure 6.11 Eddy Dissipation Rates for Physical Modifications & Benchmark Runs 128
Figure 6.12 Heat Output to Internal Loop for Physical Modifications Testing 129
Figure 6.13 Stack Temperatures for Physical Modifications Testing 129
Figure 6.14 Internal Temperatures of Configurations 2 and 3 130
Figure 6.15 Dry Gas Mole Fractions of CO and O_2 for Physical Modifications Testing ... 131

Figure 6.16 Calculated Phi for Physical Modifications Testing 131
Figure B.1 Label of Thermocouple Locations 143
Figure B.2 Cartoon of the OWHH Energy Budget 148
Figure B.3 C_p Variability Over Observed Firebox & Stack Temperature Range 149
Figure D.1 Z-dir O_2 Mole Fraction Contours for Configuration 1 153
Figure D.2 Z-dir O_2 Mole Fraction Contours for Configuration 2 153
Figure D.3 Z-dir O_2 Mole Fraction Contours for Configuration 3 154
Figure D.4: Z-dir Temperature (K) Contours for Configuration 1 154
Figure D.5: Z-dir Temperature (K) Contours for Configuration 2 155
Figure D.6: Z-dir Temperature (K) Contours for Configuration 3 155
Figure D.7: Pathlines for Configuration 1 156
Figure D.8: Pathlines for Configuration 2 156
Figure D.9: Pathlines for Configuration 3 157

LIST OF TABLES

Table Number Page

Table 1.1 Categories of Test Method 28 4

Table 1.2 NESCAUM Model Rule Restrictions 4

Table 2.1 Proximate and Ultimate Analysis of Wood Fuels 15

Table 2.2 Minimum Pyrolysis Temperatures 18

Table 2.3 Pyrolysis Products of Cellulose and Xylan 20

Table 2.4 Approximations of Primary Combustion Fuel Mixture 25

Table 2.5 Four Step Global Mechanisms 26

Table 2.6 Governing Equations for Laminar Regime 41

Table 2.7 Favre Averaged Navier-Stokes Equations with Enthalpy and Species Transport . 42

Table 2.8 LES Filtered Navier-Stokes Equations 47

Table 3.1 Summary of Measurement Methods 61

Table 4.1 Summary of Benchmark Modeling Runs 78

Table 4.2 Comparative Summary of Benchmark Model Runs 102

Table B.1 Coefficients for C_p Calculation 146

ACKNOWLEDGEMENTS

The author wishes to extend his gratitude to his committee members, especially to his advisor Professor John C. Kramlich who has offered much advice and expertise on the breadth of subjects explored in this study. Special thanks are owed the Michael J. Kirby as well, for sharing his wealth of knowledge of experimental techniques and OWHH operation. Additional thanks are owed to technical support from Dr. Renata Bura, Dr. James Riley, K. Boyd Fackler, and the staff of Greenwood Technologies. This work was supported through a Research & Technology Development grant, administered by the Washington Technology Center and funded in part by Greenwood Technologies and the University of Washington.

LIST OF COMMONLY USED VARIABLES

A	Arrhenius Pre-exponential Constant, Area
E_A	Activation Energy
ER	Mass Fuel-to-Air Equivalence Ratio
C	Specific Heat, Species Molar Concentration
D	Mass Diffusivity, Diameter
g	Gravitational Acceleration
h	Convective Heat Transfer Coefficient, Enthalpy
i	Molar Oxygen-to-Fuel Ratio
k	Thermal Conductivity, Turbulent Kinetic Energy, Kinetic Constant
L, ℓ	Length, Characteristic Length
m	Mass
M	Molecular Weight
N, n	Moles
MC_d	Moisture content on dry basis
MC_w	Moisture content on wet basis
P	Total Pressure, Partial Pressure
q, Q	Energy
R	Gas Constant, Radius, Rate of Species/Soot Creation/Destruction
S	Generic Volumetric Source Term
t	Time
T	Temperature
u	Velocity
V	Volumetric Flow Rate
X	Species Mass Fraction
Y	Species Mole Fraction
Z	Mixture Fraction

α	Thermal Diffusivity
β	Thermal Expansion Coefficient
δ	Kronecker Delta
ε	Emissivity, Turbulent Dissipation Rate
Θ	Molar Air-to-Fuel Ratio to reach measured stack conditions
μ	Dynamic Viscosity
ν	Kinematic Viscosity, Stoichiometric Coefficient
ϱ	Density
φ	Molar Air-to-Fuel Equivalence Ratio
σ	Stefan-Boltzmann Constant
τ	Stress Tensor
χ	Scalar Dissipation Rate

Chapter I: Introduction

Fire, or specifically the uncontrolled combustion of biomass, is considered by many to be our first technology, with evidence of its use estimated as early as 500,000 years ago [16]. While uncontrolled fire remains one of nature's most destructive forces, it has been tamed over many millennia to provide heat, light our homes, cook our food, and give birth to many industries. Its paramount importance is epitomized in the Ancient Greek Myth of Prometheus, who stole fire from Zeus and delivered it to early mankind, thus ensuring the success of their civilization. Wood proved to be the most useful biomass fuel, with hardwoods or softwoods in abundance within a majority of the world's latitude bands. It has a high energy density of roughly 8,550 Btu per lb on a dry basis, and an added use as a structural material.

In the more recent past, biomass has been replaced by a slew of fossil fuels of much higher energy densities and ease of transport. The engine of modern industry has been fueled by coal, natural gas, and crude oil ever since. The use of these fuels has resulted in unintended consequences, many of which we are only beginning to understand. First and foremost is that these resources are finite, as the time scales associated with their creation and current rates of their consumption is so vastly different as to render their use utterly unsustainable. These resources are also geographically limited to few concentrated reserves, which has lead to the uneasy economic symbiosis between the politically unstable Petro-states and the insatiable Western nations. Additionally, the global scientific community is increasingly concerned with the ramifications of Global Climate Change, due to the emission of carbon dioxide at a rate far outpacing the Earth's natural carbon cycle. Thus to keep up with the increasing and progressively more Westernized global population, the world's energy demands must be supplied by sustainable and domestically available resources with minimal impact to the environment.

The search for such a fuel has returned our attention to biomass, as it is a renewable resource without the intermittency problems of wind or solar. The use of biomass for direct combustion or conversion to liquid biofuels is sustainable and its supply is domestically available, notably in the Pacific Northwest. However, it is worth mentioning that members of the scientific community remain in disagreement over the degree that biomass may be

considered "carbon-neutral", i.e. whether that the carbon dioxide emitted during combustion will be taken in by other plants on a relatively short time scale. There is no disputing the advantage over fossil fuels, as in the creation of Greenhouse Gas (GHG) emission inventories many organizations do not require biomass-related emissions to be included with the site-wide GHG emissions [11]. Therefore in the face of this uncertainty, the current challenge is to minimize the environmental impact by reducing emissions of the "traditional" air pollutants to levels comparable to or better than fossil fuels.

Of the six criteria pollutants identified in the 1970 Clean Air Act, those of primary interest to biomass combustion are oxides of nitrogen (NOx), carbon monoxide (CO), and particulate matter (PM). NOx is a primary constituent of urban smog and is most commonly formed in any high temperature combustion environment. CO is emitted due to incomplete combustion. Upon inhalation it occupies with sites normally used to transport oxygen in the blood, forming carboxyhemoglobin. This reduces the oxygen carrying capacity of the blood, leading to death at high concentrations and/or long exposure durations. PM is also emitted due to incomplete combustion, which results in reduction in visibility and increased cloud seeding. Additionally, inhalation of PM from biomass combustion is not unlike that of tobacco, which causes or aggravates many lung conditions including lung cancer.

The technology of biomass for electricity production is well developed, where it presently contributes a total of 61.879 TWh [52] (17% of renewable electricity generation and 1.5% of total electrical production). It is also converted to ethanol for transportation fuel, where it currently contributes 3.4 billion gallons [53] (2% of total demand) to the total domestic demand. For electricity generation, wood and wood waste is a large renewable energy source, second only to large hydro. Biomass in transportation sector is, however, not as mature and is a recent source of controversy. In particular, the ethanol derived from corn has an unfavorable bioenergy output to fossil energy input ratio of 1.36. Biofuels do have a promising outlook, as current research estimates that cellulosic feedstocks will reach a ratio of 10.3 when employed in the future [53]. The continuing rise in the price of crude oil, natural gas, and coal coupled with the impending Federal carbon tax or cap and trade system suggest continued market penetration of biomass into these two sectors. The proverbial "low hanging fruit" with respect to reduction of criteria pollutant emissions have already

been picked, as the installed electricity generation is subjected to New Source Review (NSR) of the Clean Air Act.

1.1 Biomass at Home

Wood is also a significant source of heat for residences, used at 18% of single-family homes in the U.S. totaling 0.36 Quadrillion Btus (105.5 TWh thermal) [51]. Fireplaces and wood stoves are the most common means of consuming wood, however the former is more aesthetically pleasing than effective and the latter is not primarily a heat source. Less common but more efficient, the outdoor wood-fired hydronic heater (OWHH) is a centralized means of heat extraction for residences, agricultural operations, and small commercial buildings. This device is also known as an outdoor wood furnace or boiler, which is a misnomer as the OWHH does not boil water. The OWHH is used typically as illustrated in Figure 1.1, heating a continuous internal water loop from which the home's water circulation loop draws its heat. It can directly compete with conventional natural gas, LPG, and fuel oil fired heating devices, and is the vehicle to return biomass as a primary domestic fuel. As the OWHH is growing in popularity in response to environmental concerns and rising conventional fuel costs, reduction of NOx, CO, and PM from these devices is needed.

Figure 1.1: Typical OWHH Configuration [29]

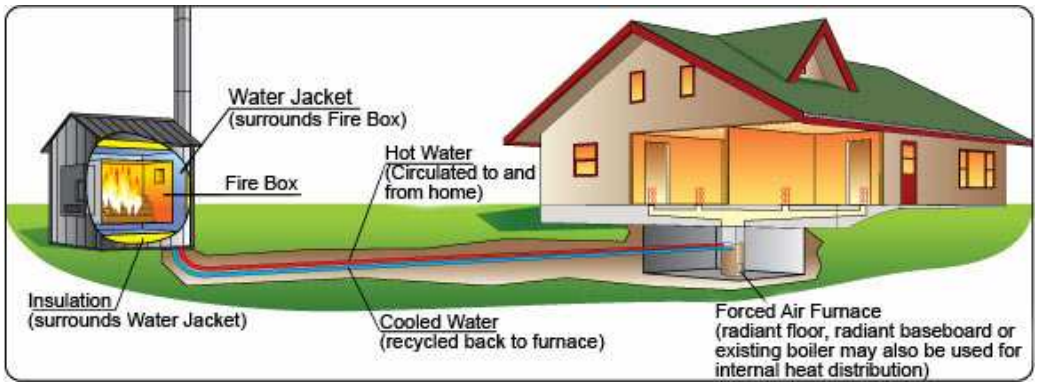

The U.S. Environmental Protection Agency (EPA) does not yet directly regulate OWHHs as it does coal-fired power plants or other traditional source of criteria air

pollutants, due to the fact that its primary use is on private property. However, the health risks associated with PM emitted from residential wood combustion, especially during an atmospheric inversion, have prompted many local air pollution regulatory agencies to enforce "Burn Bans" [43]. While operation of an OWHH results in NOx and CO emissions as well, current attention focuses on first on these PM related health effects. In light of these concerns and to accommodate the increasingly environmentally conscious consumer, the EPA has established a voluntary PM emissions reduction program for OWHH manufacturers. Those OWHH models certified under this program meet the Phase 1 Emissions Level of 0.6 lbs PM per million Btu (MMBtu) input, as assessed by the EPA Test Method 28: *Measurement of Particulate Emissions and Heating Efficiency of Outdoor Wood-Fired Hydronic Heating Appliances* [55]. This emissions level is assessed as a weighted average of four different heating loads outlined in Table 1.1, not unlike that of engine duty cycles.

Table 1.1: Categories of Test Method 28 [55]

Category	Percentage of Maximum Rated Output	Year-Round Weighting Factors	Seasonal Weighting Factors
1	<15%	0.437	0.175
2	16 to 24%	0.238	0.275
3	25 to 50%	0.275	0.450
4	100%	0.050	0.100

The Northeast States for Coordinated Air Use Management (NESCAUM) has developed a stricter model rule outlined in Table 1.2, to be adopted by state and local authorities. This is a significant challenge for the OWHH industry, for which at the start of this study only one unit was certified per the EPA Phase 1 Emissions Level and the subject of this study [39], the Greenwood Technologies Model 100, had an unadjusted Category 4 emission rate of 1.043 lb/MMBtu input.

Table 1.2: NESCAUM Model Rule Restrictions [39]

	Overall Emissions Limit	Emission Rate Limit	Adoption Date
Phase I	0.44 lb PM/MMBtu input	N/A	March 31, 2008
Phase II	0.32 lb PM/MMBtu output	15 g/hr	March 31, 2010

1.2 Approaching the Problem

In the OWHH, the wood is burned as a batch process in a fixed-bed combustor, where the fuel load is replenished roughly every 8-12 hours. While batch systems are easy for the consumer to use, this presents a challenge to the engineer to design a system optimized for different stages of wood combustion. Wood is generally considered to burn in four distinct, but overlapping stages [48]:

1) Heating and drying – Moisture is driven off and the solid fuel is brought to the temperature needed to begin pyrolysis
2) Solid-phase pyrolysis – Thermal degradation of organic material begins, releasing high molecular weight volatile species
3) Gas-phase pyrolysis and oxidation – Further degradation of volatile species occurs and radical species are generated, which combine with oxygen at the flame front to form product species
4) Char oxidation – Once volatiles are driven off, direct combustion of black carbon occurs

Spatially, the movement of heat, species, and air is summarized Figure 1.2 [48]. This offers a clearer picture on how to address PM reduction. The simplest method would be that of prevention, not creating the PM in the first place. This requires a fine tuning of the fuel and air mixing, especially during the gas phase oxidation stage.

Figure 1.2: Material and Heat Flow Diagram of Wood Combustion [48]

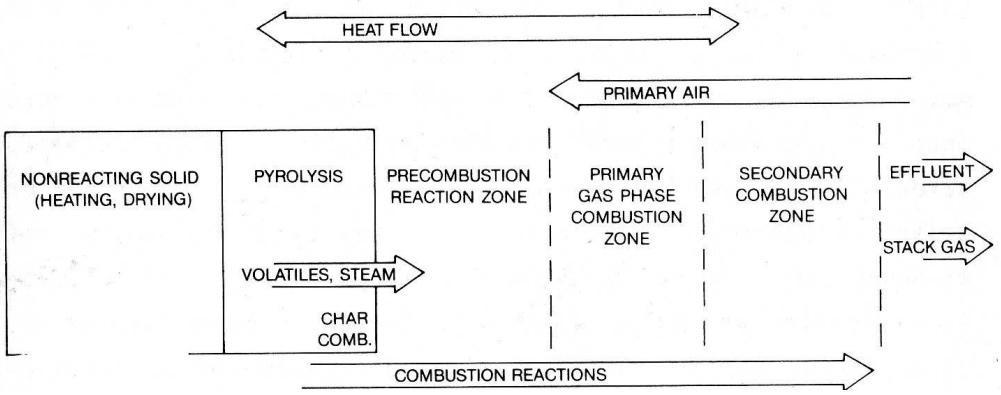

For many OWHHs, the length of the flow path between the primary combustion zone and the exhaust exit is a dozen feet or more, to accommodate the necessary heat exchanger surface area. In the likely case that indeed PM does form, this introduces the opportunity for mitigation. The old adage is for complete combustion, one needs time, temperature, and turbulence, which leads to several mitigation methods. The exhaust path prior to heat extraction, after which oxidation reactions will slow down greatly, may be lengthened to provide additional particle burnout time. Exhaust gas heat loss may be prevented to keep post-flame temperatures above those required for particle burnout and for CO oxidation, (the latter is not a regulated emission, but good CO burnout leads to an improvement in efficiency). Poor primary flame mixing, which may be expected from natural draft flames such as those found in the Model 100, will create fuel rich parcels in the exhaust. These may be broken up and burned by enhancing flow path mixing with obstructions and secondary air introduction.

1.2.1 A Problem of Fluid Mechanics

To fully describe the operation of the OWHH from first principles and explore the different prevention and mitigation scenarios with respect to PM emissions and improved efficiency would be an intractable task. So called "back of the envelope" calculations may provide order of magnitude information, and analysis of particular segments of the OWHH's operation may provide theoretical insight, but a more efficient plan of attack is that of combined modeling and experimentation. Data sets from initial experimentation are used to validate the initial model, scenarios are explored with the model, experiments verify the suggested prevention or mitigation measures, and the model is again validated, and so on.

Computational Fluid Dynamics (CFD) is to be used, as the continuing rise in the processor speed and memory of desktop computers allows for computationally demanding models to be run with greater and greater resolution and fidelity. In the past few decades when CFD codes became more accessible, they were applied to similar problems dealing with coal-fired boilers. They have not, however, been applied to fixed-bed wood combustion until very recently. This is due to both the recent renewed interest in biomass as a fuel and

complexities associated with the buoyancy driven flows not seen inside of forced-draft pulverized coal-fired boilers. The abovementioned pollutant mitigation measures strongly suggest that the flow field of the OWHH will be of great interest, and the investigation of the effect of physical modifications is cheaper to employ in the computational than in the laboratory domain. CFD provides numerical solutions to the Navier-Stokes equations that express conservation of mass and momentum, along with other equations of interest relating to energy conservation, radiation, species transport, variables relating to turbulence, and scalars of interest. All models require simplifying assumptions, and thus the results represent an approximation of the physics. Thus, all results must be scrutinized with respect to the appropriateness of the assumptions under the particular situation being modeled.

Thus, in the effort to reduce PM emissions and improve efficiency of the Model 100 OWHH to meet present and upcoming emissions standards, we return to the study of mankind's oldest technology, fire. Fire is more accurately described as a buoyancy (rather than momentum) dominated diffusion flame and represents a classic feedback mechanism. The sufficiently hot pyrolysis gases released by the wood produce a gaseous flame at the fuel/air interface, irradiating the wood, producing more pyrolysis gas, and so on. Of the flow field, the key mechanisms characterizing the flame are the entrainment rate of the oxidizer and the buoyancy effects on the volumetric heat release which are both found to simultaneously enhance and diminish the completion of combustion. It is ironic that some of the most modern sophisticated computer software and hardware are required to approach a complete description of this long exploited natural phenomenon.

Chapter II: Theory and Literature Review

CFD modeling of biomass combustion, in particular fixed-bed systems, has only recently begun to receive attention. This is largely due to the resurgence of biomass as a viable fuel. Despite the market penetration of biomass as a fuel for the electricity and transportation sector in the U.S., much of the recent work has come from international institutions. Researchers from such parts of the world as India, Sweden, Finland, and Italy have performed CFD studies of fixed-bed wood combustion, perhaps due to their respective governments' more aggressive policy towards promoting biomass or the increased local abundance and/or usage of biomass compared to that of the United States. The increasing availability of powerful computing resources and sophisticated of-the-shelf CFD packages have also contributed to this recent interest. There is not yet agreement on the best method to simulate OWHH operation, however similar themes arise.

In determining how to appropriately model the operation of the OWHH with the goals of PM emission reduction and improved efficiency, four separate facets must be addressed: (1) how to chemically characterize the wood during the various phases of the burn, (2) how to characterize the PM formation and oxidation, (3) how to assess the heat transfer within the unit, and (4) how to accurately capture the physics of the flow field and its effect on the previous three facets. As mentioned previously, to do so from first principles in a comprehensive model is intractable at present. Therefore, a discussion of the theory and recent work in the literature of each facet is required before we may discuss how they interface to make decisions on how they are to be modeled.

2.1 Wood Chemistry and Combustion

Much like its better understood cousin coal, wood is a remarkably heterogeneous organic solid fuel. Its complete chemical composition is approximated and varies greatly from species to species and from region to region. The wealth of knowledge of the anatomy of wood and its chemical composition is owed to botanists and the timber and paper industries alike. Many volumes have been written on this subject. When considering wood combustion, the most important properties are the elemental composition and the heating

value. These are both macroscopic properties, and thus much of the literature on the details of wood chemistry is of less importance to one who is simply burning the wood. Therefore, while the scope of this study will not require all of the details of this section, it is worthwhile to explore the reasons behind why the wood combustion behaves the way it does.

2.1.1 The Structure of Wood [9]

Trees vary greatly in size and in composition, however with respect to wood most often used as fuel, they have nearly uniform structure. Internally all vascular plants have two types of transport tissue, xylem and phloem. The xylem tissue primarily transports water and the phloem transports nutrients, particularly sugars. In a tree, the xylem tissue is the wood and the phloem is beneath the bark where growth occurs, interestingly from which the two words of Greek origin get their names. As the xylem tissue, or wood tissue, makes up the majority of that which is used as a fuel, it will be the focus of this study. OWHHs, such as the Model 100, are designed to burn cordwood, which has the bark intact, however structurally or chemically ignoring the bark is not expected to affect this study.

Wood is characterized by long, elongated cells running along the axis of the stem, or trunk in the case of the sections used commonly for fuel. These cells allow for speedy vertical transport of water, radial transport of nutrients, and also as serve as structural members. This prevents usage of typically isotropic properties, such as thermal conductivity and mass diffusivity. As expected, the drying of the wood occurs directionally as well and must be taken into account when determining a sample's moisture content.

These cells emanate radially from the center, or pith, of the tree trunk. During each growth season, roughly May to September for higher latitudes in the Northern Hemisphere, the tree will grow radially one layer. In order to facilitate this growth when sunshine is plentiful, the cells are larger in order to transport the water needed in the 'earlywood'. As the days grow shorter towards autumn, the growing slows and smaller cells are created to assure structural integrity during the winter, in the 'latewood'. The smaller latewood cells are darker than the earlywood cells, forming the annual rings many are familiar with shown in Figure 2.1 [57]. Rays also form, which are radial channels used to transport sugars from the foliage back to the tree and water from the roots to the foliage and growth regions.

Figure 2.1: Microscopic Structure of Softwood Cells [57]

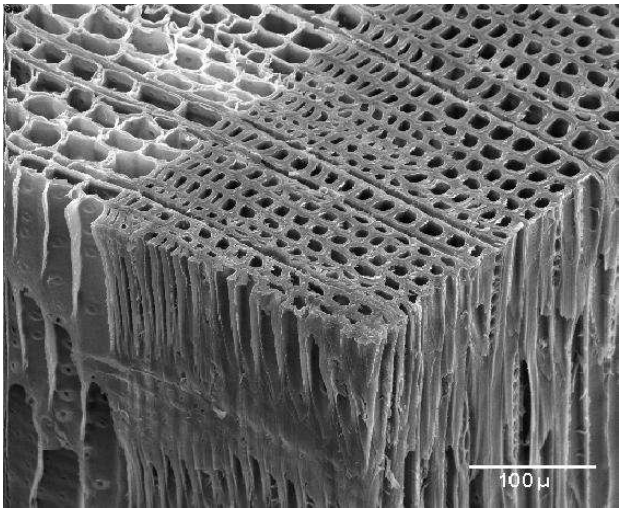

As the tree ages, two distinct radial zones are created, the sapwood and heartwood. The heartwood is the inner zone, composed of dead tissue which performs storage and structural functions. The outer zone, sapwood, is living and performs the majority of transport functions. The sapwood has significantly higher moisture content and lower extractive oils content, hence its distinctly lighter color.

There are distinct differences in wood structure between the two classes of trees, softwoods (gymnosperms, conifers, or evergreens) and hardwoods (angiosperms or deciduous trees). There exist roughly 530 species of softwoods and 30,000 species of hardwoods, the diversity of hardwoods being seen in tropical latitudes. Softwoods are composed of 90-95% tracheids, the abovementioned long vertically oriented cells, and 5-10% rays. There are also a small amount of resin canals that provide resin upon surface injury of the tree, which are similar in orientation as rays but much larger in size. These canals are not cells themselves, rather functional gaps between cells. At this point, it is apparent that Figure 2.1 is a softwood. Hardwoods are more complex, composed of libriform cells, or fiber tracheids, vessels, and rays which can be seen in Figure 2.2 & 2.3 [48, 4]. Libriform cells are similar to but shorter than softwood tracheids, and are tasked more with structural integrity than water transport. Vessels, which take up to 25% of the cross-sectional area, serve as major water transport corridors and are especially needed during the creation of leaves in the early growing season. Hardwood rays are similar in function and size to softwoods, however there are much more of them, as up to 30% of the stem volume.

Figure 2.2: Hardwood Structure Diagram [48]

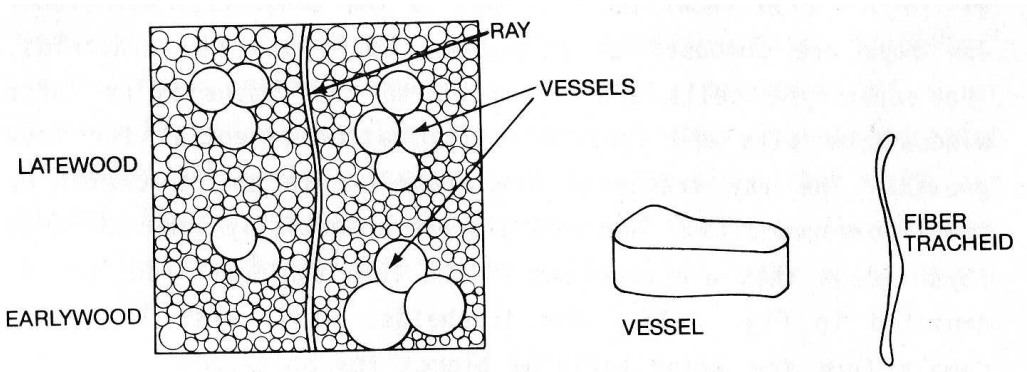

Figure 2.3: Microscopic Structure of Hardwood Cells [4]

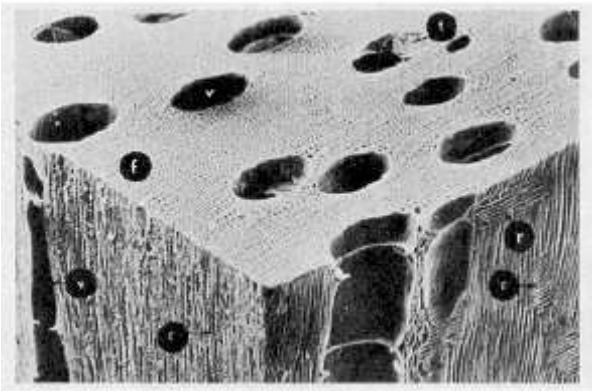

The structure of wood as it relates to its combustion has the most bearing during the heating and drying stage. Water may be classified into two groups relating to how it is held within the wood, free water is held in the tracheids and vessels by capillary mechanisms and bound water has been adsorbed into the cellular structure. The bound water in the wood reaches the fiber saturation point, usually 23 to 25% by total wet weight basis, which is the point where the force required to hold the bound water in hydrogen bonds is balanced by the force of physical swelling required by the cells. Moisture above this point will be absorbed as free water. A significant amount of the free water is released when the tree is felled and it is exclusively bound water that remains in seasoned wood. For comparison, the EPA Method 28 requires that the wood fuel charge have between 19 and 25% on a dry weight basis [55].

2.1.2 Wood Chemistry [9]

Wood, like other forms of life, is largely comprised of carbon, hydrogen, oxygen, smaller amounts of nitrogen and sulfur, and trace amounts of chlorine and mineral matter. Botanically speaking, it is a combination of cellulose, hemicelluloses, lignin, various extractives, and water for which the relative percentages of each of these vary from sample to sample. Cellulose and hemicelluloses are often collectively referred as holocellulose. The function of these groups within the tree is analogous to that of a granola bar, holocellulose, largely by cellulose individually, would represent the seeds and nuts providing structure, lignin would represent the honey holding everything together, and finally the extractives would be the preservatives and additional coloring. The relative makeup of wood is roughly 45% cellulose, 30% hemicelluloses, and 25% lignin on a dry basis with extractives removed. Both hardwoods and softwoods will have similar cellulose content, however hardwoods will have less lignin and more hemicelluloses than softwoods. It is worth discussing the structure of cellulose, hemicelluloses, and lignin in some detail.

Cellulose is the backbone of wood, providing its rigid structure and supporting the tree's height. It is a well understood chemically and has the same structure in softwoods and hardwoods. Shown in Figure 2.4, cellulose is a polymer chain of roughly 10,000 β-D glucopyranose molecules forming a homopolysaccharide. Each individual glucose sugar unit has the formula $C_6H_{12}O_6$. Between adjacent cellulose chains, the OH and CH_2OH groups are where the bound water is held by Van der Waals forces and hydrogen bonding. As the water is adsorbed, heat is released and the cellulose bonds relax, causing the abovementioned swelling.

Figure 2.4: Cellulose Chemical Structure [9]

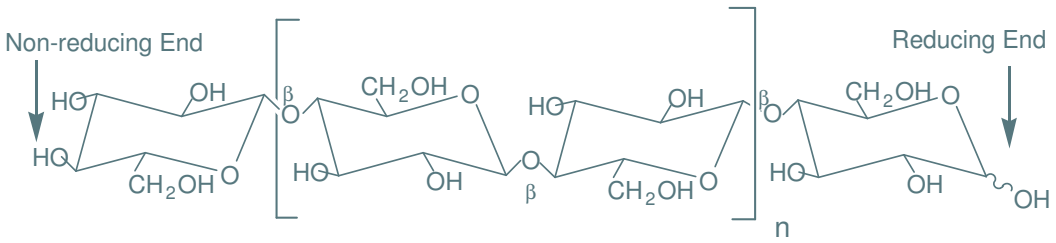

Hemicelluloses are a large class of molecules that differ from softwoods to hardwoods. They are composed of 6 carbon sugars, like cellulose, and also 5 carbon sugars. However, they are not nearly as polymerized as cellulose, containing 50 to 300 units. Functionally, hemicelluloses surround the cellulose chains to form macromolecular fibers, or fibrils, much like the bundled cables used with suspension bridges. As hemicelluloses are a large class of molecules, only the main constituent of softwoods and hardwoods are to be discussed. Roughly 66% of softwoods are composed of galactoglucomannans, which have the structure seen in Figure 2.5 and 85% of hardwoods are composed of glucuronoxylans seen in Figure 2.6. While the particular formula of these hemicelluloses and those not shown are not crucial for the modeling of the OWHH, it should be noted that the chemical composition does not vary that much from cellulose. The reason is, that the aromatic structures forming the hemicellulose backbone, mannans and xylans in the figures shown, are all based on similarly structured monosaccharides. This will be used as an argument to treat holocellulose as chemically homogenous.

Figure 2.5: Galactoglucomannan Structure [4]

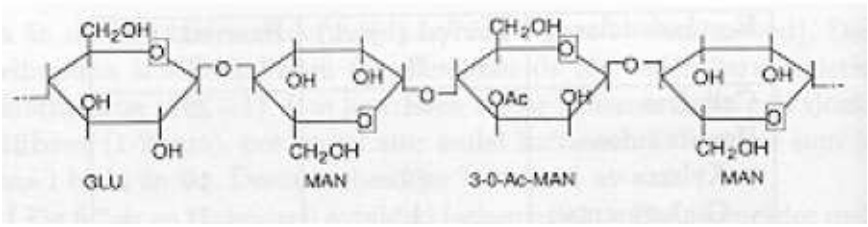

Figure 2.6: Glucuronoxylan Structure [4]

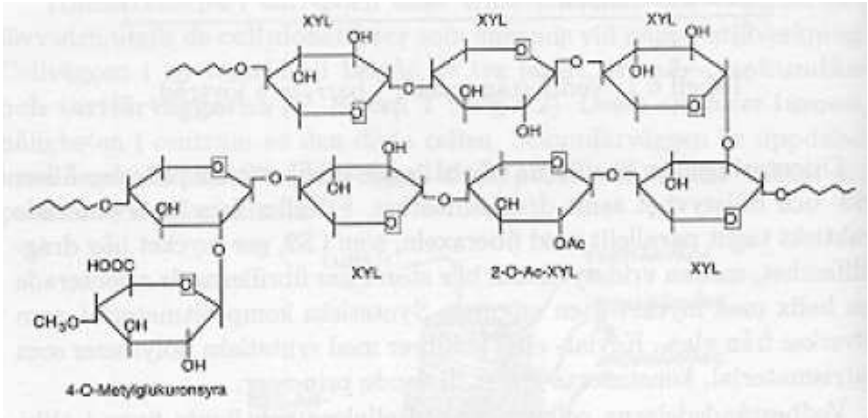

Lastly, lignin is often thought of as the glue that holds the fibrils together to create and hold together cell walls. It is very heterogeneous, and its exact structure remains a source of debate amongst botanists. One proposed structure of lignin by Sakakibara can be seen in Figure 2.7. To chemically assess lignin to a degree that offers the insight towards the modeling of an OWHH goes beyond the scope of this study. Having little use other than its fuel value, lignin has long been the bane of the paper industry's existence and an old joke is that it "can make anything except money" [8].

Figure 2.7: One Proposed Structure of Lignin [9]

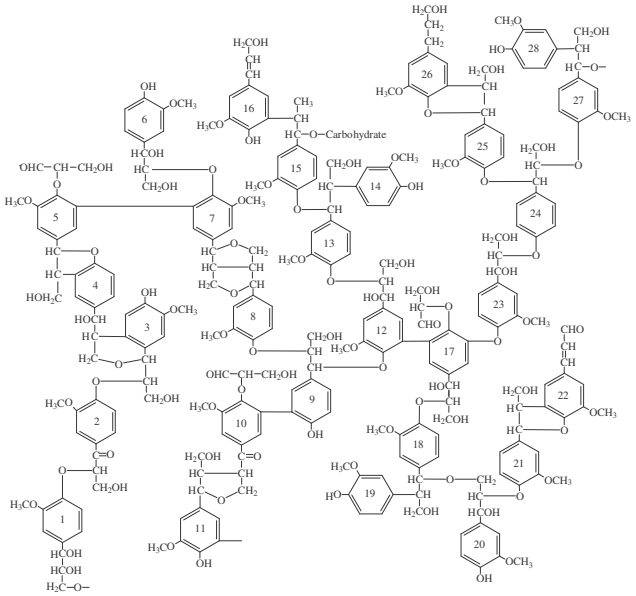

Approximations of the wood composition may be made in a similar fashion to coal even though biomass is easier to structurally characterize due to extensive knowledge of plant biochemistry. Proximate analysis is where a sample is heating in a series of environments such that the total moisture, volatile matter, fixed carbon, and ash are progressively quantified. An ultimate analysis further characterizes the fuel by atomic content, C, H, N, and O as the primary species in wood. The proximate and ultimate analyses of the woods used in this study are outlined in Table 2.1 on a dry basis [48, 5].

Table 2.1: Proximate and Ultimate Analysis of Wood Fuels

Species	Volatile Matter	Fixed carbon	Ash	Elemental Weight Percent			
				C	H	N	O
White Oak	86.2	13.5	0.3[1]	49.5	5.4	.4	43.1
Douglas Fir	86.2	13.7	0.1	52.3	6.3	0.1	40.5
Cedar	77.0	21.0	2.0	48.8	6.4	0	44.4

2.1.3 Wood Combustion

The four stages of wood combustion are to be outlined in this section. At this point, it is worth discussing the typical operation of the Model 1 OWHH versus what the EPA Test Method 28 requires. The Model 1 OWHH operates with cordwood, or cut logs. The combustion region lined with heavy refractory brick, which is preheated. The large cordwood blocks are placed in the firebox, the heat from the refractory brick provides the ignition source, and the OWHH runs for roughly 8 hours until refueling is required. The cordwood is generally seasoned, or air dried to roughly 20 to 30% moisture on a dry basis. The Method 28 test requires a different, more repeatable fuel configuration, called a test crib. The crib wood, for which the total weight is a function of the firebox volume, is a set of 4" x 4" oak pieces which are to be separated by ¾" inserts, as shown in Figure 2.8. The test stipulates the use of red or white oak within the range of 19 to 25% moisture on a dry basis [55]. Obviously, the behavior of the fuel burn will differ greatly between the two scenarios, and the stages of wood combustion will be discussed in this context.

[1] Approximated as Red Oak Sawdust

Figure 2.8: Method 28 Test Crib Configuration [55]

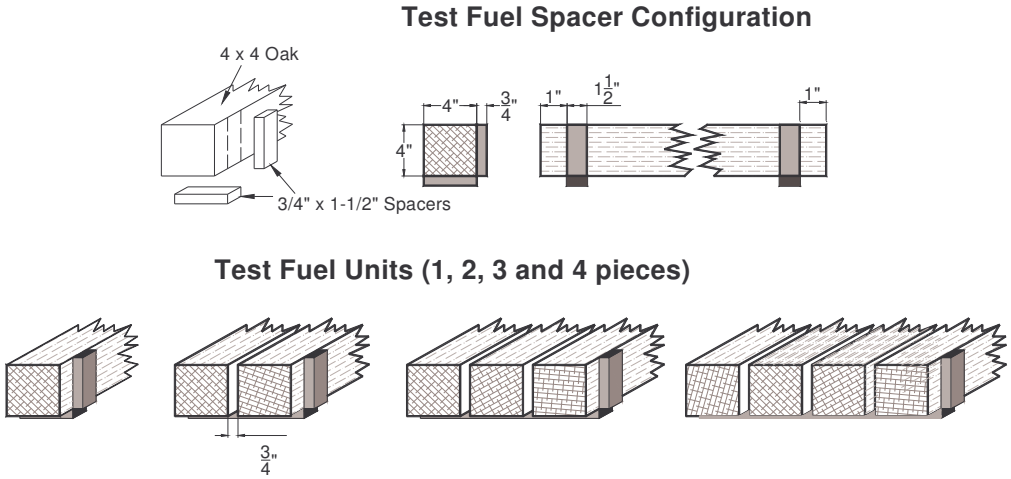

A huge literature exists on the basic processes occurring during wood combustion. A detailed review is beyond the scope of the present work. Instead, we present an overview of the process that focused on the conditions specific to natural draft wood combustion. This is presented in the form of an outline rather than in the form of a review of individual papers.

2.1.3.1 Heating and Drying Stage

As the cordwood or test crib is placed into the preheated firebox, heating and drying begins. Generally, the air dried wood will not have any free water in the tracheids, and vessels in the case of hardwoods. The remaining trace free water and the bound water will reside in the void space between tracheids and adsorbed to the holocellulose structure respectively. First, it is useful to distinguish between the two conventions of moisture content reporting of biomass. The more common convention is moisture content on a dry basis, or oven-dried basis, and the less common is on a wet, or green basis as defined respectively in equations 2.1 and 2.2. While it is more convenient to perform calculations on a wet basis, it is easy to convert to a dry basis.

$$MC_d = \frac{m_{water}}{m_{wood,dry}} \qquad \text{Equations 2.1}$$

$$MC_w = \frac{m_{water}}{m_{wood,dry} + m_{water}}$$ Equations 2.2

During the heating of the wood, the water hinders and promotes this process by increasing the specific heat but also increasing the thermal conductivity. The full drying process can be broken into four steps: heating of the wood to 100°C, heating the bound water to 100°C, overcoming the heat of vaporization, and overcoming the heat of desorption of the bound water. The total heat required per mass of wet wood is outlined in equation 2.3. The specific heat of wood can be estimated by equation 2.4. The heat of vaporization of water at 100°C is 2.26MJ/kg, the heat of desorption for moisture contents between 12-30% on a wet basis varies between 9.5-2.4 kJ/kg moisture, and the specific heat of water for the temperature range may be estimated as 4.2 kJ/kg K [48].

$$q_{dry} = \left(C_{wood}(1 - MC_w) + C_{water}MC_w\right)(373K - T_F) + \left(H_{vap} + H_{desorb}\right)MC_w \quad [kJ/kg\ wet]$$

Equation 2.3

$$C_{wood} = 0.0635 + 2.769 \cdot 10^{-4}(T - 273K) \qquad [kJ/kg \cdot K]$$ Equation 2.4

For a 15°C wood sample with 20% moisture content on a dry basis (16% wet basis), typical for the EPA Test Method 28, and estimated heat of desorption of 7.9 kJ/kg moisture, the total heat required for drying is 426 kJ/kg (183 Btu/lb) wet wood with the largest contribution from overcoming the heat of vaporization. This is 2% of the heating value of dry wood, of roughly 8,550 Btu/lb. Upon entering the preheated firebox at a typical 700 K, the process will occur at the wood surface quickly, especially for the exposed surface area of the test crib.

2.1.3.2 Solid Phase Pyrolysis

The exact mechanisms of solid phase pyrolysis may never be known, and the plethora of modeling techniques reflects the continued research on this topic. As many as 213 species are estimated to make up the products of cellulose pyrolysis alone [27], which their formation depends on the moisture content, heating rate, species, and other

parameters. Additionally, there are great discrepancies in which the experimentation supports these theories and validates these models.

Once the surface layer of the cordwood or test crib dries, the internal temperature will begin to quickly rise from 373 K to the pyrolysis temperature, where this stage begins. Values used for this pyrolysis temperature are outlined in Table 2.2, the variation may be attributed to different species, experimental techniques, and heating rates.

Table 2.2: Minimum Pyrolysis Temperatures

Source	**Sample**	**Pyrolysis Temperature**
Tillman [48]	Wood	500 K
Shafizadeh and Chin [44]	Hemicellulose	500 K
	Cellulose	600 K
	Lignin	500 K
Welker [56]	Cellulose	553 K
Galgano [23]	Wood	500 K
Huttenen [31]	Wood	523 K

To estimate an idea of time required for the wood to reach the pyrolysis temperature of 500 K, a simplified model is used [17]. A zeroth order pyrolysis rate is assumed, shown in equation 2.5, for a non-reacting and moisture free 1-D slab. Assuming that the slab is thermally thin, that is the internal temperature gradient is negligible, the heat diffusion equation may be used with the following boundary conditions, in equation 2.6.

$$\dot{m}'' = A_p \rho_p e^{\left(-E_a / RT_s\right)} \qquad \text{Equation 2.5}$$

$$\frac{\partial T_s}{\partial t} = \alpha_s \frac{\partial^2 T_s}{\partial x^2}; \quad \text{at t = 0, } T_s = T_o, \text{ at y = 0, } k_s \frac{\partial T_s}{\partial x} = \dot{Q}_s'', \text{ and at y = 2 in, } \frac{\partial T_s}{\partial x} = 0$$

Equation 2.6

Solving equation 2.6, the time until pyrolysis begins may be estimated by equation 2.7.

$$t_p = \frac{\rho_s C_s s\left(T_p - T_o\right)}{\dot{Q}_s''} \qquad \text{Equation 2.7}$$

The surface heat flux is the sum of free convective and radiative heat transfer and is estimated between the pyrolysis temperature of 500 K and the typical initial firebox temperature of 700 K. Assuming a density of 460 kg/m^3 [25], specific heat of 1.26 kJ/kg K [12], emissivity of 0.87, convective heat transfer coefficient of 10 W/m^2 K [32], and the slab thickness will be 2 inches, half of the crib thickness. The resulting time is almost 6 minutes. This order of magnitude is consistent with the time elapsed before CO and PM emissions start during testing.

The wood temperature will increase during solid phase pyrolysis and asymptote on a ceiling temperature of 773 K until all of the volatiles are driven off and only char remains [56]. In an inert atmosphere, several studies have indicated that this pyrolysis process is endothermic and others show it to be exothermic. To support the endothermic pyrolysis theory, a drop in surface temperature is observed just prior to ignition in the studies of Gardon and Martin [56]. Simmons notes that pyrolysis is indeed endothermic up until an internal temperature of 550 K, however between 550 K and 775K pyrolysis is exothermic and supporting of secondary gas phase reactions [45]. Beyond 775 K, the char stage has been reached. In the context of the operation of a preheated OWHH, this fine distinction from endothermic to exothermic is not as important. The preheated firebox air has a minimum temperature of 700 K and the wood char bed that the cordwood or test crib is placed upon provides a quick ignition source. The exothermic release of the high temperature pyrolysis is less crucial for secondary gas phase pyrolysis within the preheated refractory walls.

When examining the chemical structure of cellulose, the major hemicelluloses, and lignin, pyrolysis proceeds as one may intuitively imagine. First, the bonds holding together the aromatic structures are broken, and then simultaneously energetic reactions create light volatile species and condensation reactions create heavy tars and char. The higher the heating rate, the less char is produced [17]. The solid phase pyrolysis products of cellulose and xylan, the major aromatic structure of hardwood hemicelluloses, are found in Table 2.3. These high molecular weight products will be further pyrolyzed in the gas phase and oxidation stage. While the particular chemicals are not important to this study directly, it is useful to note that the compounds to be further pyrolyzed are mostly aldehydes with between one to six carbons and bound oxygen. The tars reported are condensed higher

molecular weight hydrocarbons including but not limited to phenylacetylene, anthracene, and naphthalene [48].

Table 2.3: Pyrolysis Products of Cellulose and Xylan [48]

Specie	Molecular Weight (kg/kmol)	Cellulose (at 873 K)	Xylan (at 773 K)
Acetaldehyde	44.05	1.5	2.4
Acetone propionaldehyde	116.16	0.0	0.3
Furan	68.07	0.7	Trace
Propenal (acrolein)	56.06	0.8	0.0
Methanol	32.04	1.1	1.3
2-Methylfuran	82.10	Trace	0.0
2,3-Butanedione (diacetyl)	86.09	2.0	Trace
1-Hydroxy-2-propanone glyoxal	132.03	2.8	0.4
Acetic Acid	60.05	1.0	1.5
2-Furaldehyde	96.00	1.3	4.5
5-Methyl-2-furaldehyde	110.11	0.5	0.0
Carbon Dioxide	44.00	6.0	8.0
Water	18.00	11.0	7.0
Char	n/a	5.0	10.0
Tar	n/a	66.0	64.0

Such an analysis of lignin, due to its complex structure and litany of asymmetries seen prior in Figure 2.7, is not useful to this study due to inconsistencies in data reported. Full pyrolysis of lignin to gaseous species yields the following products: CO (50%), CO_2 (10%), CH_4 (38%), and C_2H_2 (2%) [48]. The char yield is comparable to that of cellulose and xylan seen in Table 2.3.

Once a layer of char is formed on the outside, the pyrolysis front moves towards the center, which still contains moisture. The pyrolyzed species, like those in Table 2.3, diffuse through the outer char layer to the gas phase. One may think of these solid phase processes as two fronts, the drying front followed by the pyrolysis front. Galgano et al.. has created a mathematical model describing the movement of these fronts, validated the model extensively, and incorporated this pyrolysis submodel into a CFD simulation [23, 24]. While this would be ideal to use for this study, this submodel has many kinetic and property parameters specific to the Beech wood sample that were experimentally derived for this

particular study, such as the pyrolysis activation energy, pre-exponential factors, and empirical constants. Interestingly, this study of a cylindrical log did show these fronts to move with almost constant speed [23], as seen in Figure 2.9, for radii defined R_c as the combustion front, R_p as the pyrolysis front, and R_u is the drying front. From this, moisture content will be approximated as constant throughout this phase.

Figure 2.9: Movement of Combustion, Pyrolysis, and Drying Fronts [23]

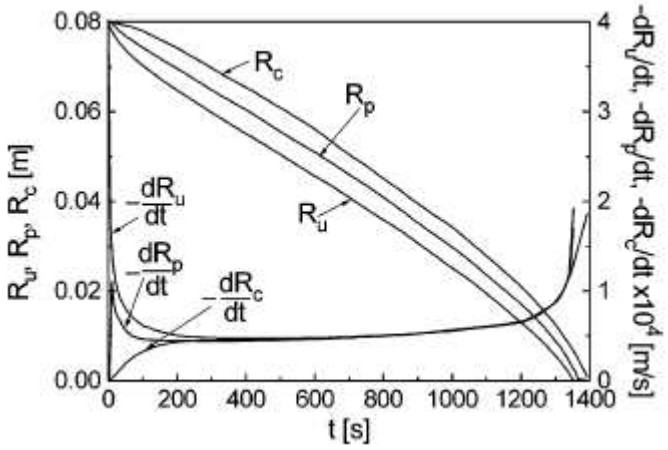

Solid phase pyrolysis kinetics is most commonly experimentally studied in two ways, in an isothermal and a steadily heated environment. The weight loss of a sample is examined over a heating time of up to several years and up to 160 K/min, for the non-isothermal studies. The activation energy and pre-exponential factors are sensitive to the environmental temperature. Especially with the isothermal studies, there are wide disagreements amongst the results, suggesting the applicability of these values restricted to narrow temperature ranges. For example, one study reported over a 50% increase in the activation temperature over a 120 K range [56].

The moisture content of the wood has an effect on this stage through limiting the internal temperature prior to the pyrolysis front. As mentioned earlier, the notable result of internal temperature reduction is an increased char yield. As to be expected, the moisture content reduces the flame temperature, and with the estimate of Tillman et al. assuming stoichiometric air, this relationship is seen in Figure 2.10 [48].

Figure 2.10: Adiabatic Flame Temperature versus Moisture Content

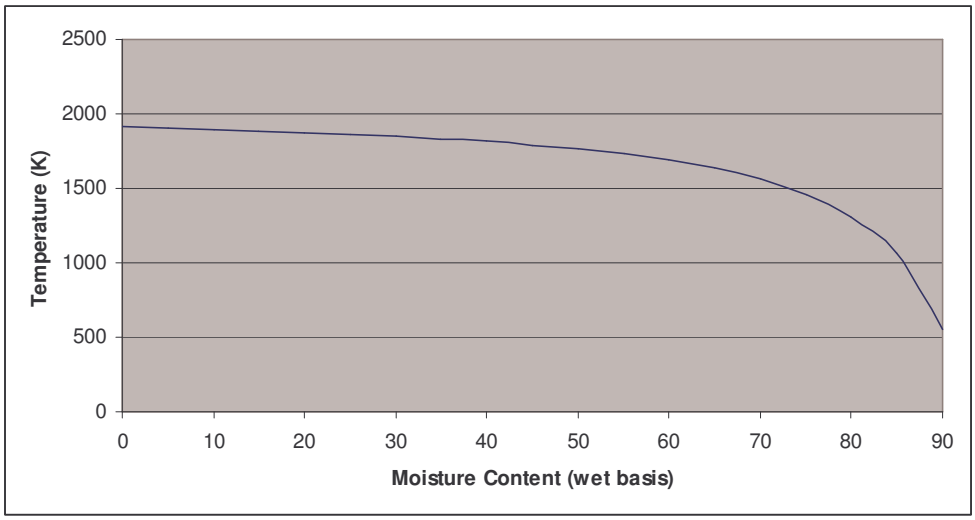

Pyrolysis into an oxygen rich atmosphere versus an inert atmosphere greatly reduces the activation energy. A study of isothermal cellulose pyrolysis revealed dramatic increases then slight decreases in light hydrocarbons, CO_2, and H_2 yields from an inert to 5% O_2 to 21% O_2 environment. Only CO yields continued to increase with the % O_2 increase, revealing a shift in the rate determining step. As the near surface concentration of oxygen goes to zero once a flame develops, this effect is not important for the burn duration, however it reveals the care required when applying a "one size fits all" pyrolysis mechanism over varying environmental temperatures, fuel moisture contents, and surface species concentrations [45].

2.1.3.3 Gas Phase Pyrolysis and Oxidation

The solid phase pyrolysis products, consisting of organic acids, aldehydes, esters, carbon dioxide, water vapor, and other species, diffuse through the outer char layer, enter the gas phase, and break down into lighter, more flammable species approaching the flame front. Without this further breakdown into more reactive species, combustion would not be so easily supported. From the perspective of this study, this is most important stage, as this is where PM is created and this stage dictates the flame dynamics. Due to the particular importance to this study, the formation of and oxidation of PM will be addressed in a later

section. Tillman et al. suggest separately examining the pre-combustion zone near the wood surface, the primary combustion zone containing the flame, and the post-combustion zone [48].

The pre-combustion zone is where exterior heat sources, radiation from the flame, and possible exothermic releases from high temperature solid phase pyrolysis provide the activation energy for gas phase pyrolysis. Tillman et al. classifies the two types of reactions as seen in equations 2.8 and 2.9, where R represents a generic organic molecule. The former class represents the cleaving or recombination of a C-C bond and the latter the cleaving of a C-H bond. The C-C bond is preferentially broken over the C-H bond when R" contains two or more carbons. For hydrocarbon species, the breaking of the C-H bond is an important source of the methyl radical, CH_3. The reverse of equation 2.8 occurs more often for larger pre-combustion zones, achieved by fuel-rich firebox conditions. [48]

$$R - R \Leftrightarrow R + R' \qquad \text{Equation 2.8}$$

$$R''-H \Rightarrow R''+H \qquad \text{Equation 2.9}$$

The bound oxygen of the solid phase pyrolysis species, found in the aldehydes listed in Table 2.3 and as shown in Figure 2.11, is held by a double bond and does not typically participate in the pre-combustion reactions. This is noted in Glassman in the discussion of aldehyde oxidation, where the pyrolysis is shown in equation 2.10, where M is any third body causing collision [26]. The hydrogen radical will often produce methane when combining with the methyl radicals produced in equation 2.9 or combine with itself to form molecular hydrogen. The RCO radical will eventually decompose and release the CO. Also, if any molecular oxygen reached this zone, Simmons states that "the reaction of alkyl radicals with oxygen is too slow to compete with their unimolecular decomposition reactions" [45].

Figure 2.11: Aldehyde Diagram

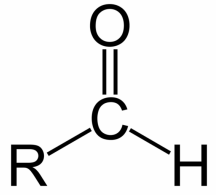

$$RCHO + M \Rightarrow RCO + H + M$$ Equation 2.10

The primary combustion zone is where the atmospheric oxygen comes into contact with the abovementioned fuel and radical species, and will support a series of chain reactions until final product species are formed. Tillman et al. note that the formation of HO_2 radicals are not energetically favored, rather that the important chain branching reaction are described in equation 2.11 [48]. The methyl radicals formed in the pre-combustion zone in the presence of oxygen form formaldehyde and a hydroxyl radical, both unstable species and important to supporting combustion. Tillman et al. also note that the fairly low C:H ratio in wood, close to one recalling Table 2.1, along with the release of moisture also contributes to the hydroxyl radical pool ensuring swift combustion [48].

$$\left.\begin{aligned} CH_3 + O_2 + M &\Rightarrow CH_3O_2 + M \\ CH_3O_2 &\Rightarrow CH_2O + OH \end{aligned}\right]$$ Equation 2.11

Simmons also notes the key role of the hydroxyl radicals in the following two sequences in equations 2.13 and 2.14 [45]. As seen previously, formaldehyde plays a crucial role as an intermediate fuel, which has led some researchers to treat it as a surrogate for all wood volatiles.

$$\left.\begin{aligned} H + O_2 &\Rightarrow OH + O \\ CO + OH &\Rightarrow CO_2 + H \end{aligned}\right]$$ Equation 2.12

$$\left.\begin{aligned} CH_3 + O &\Rightarrow CH_2O + H \\ CH_2O + OH &\Rightarrow HCO + H_2O \\ CH_2O + H &\Rightarrow HCO + H_2 \\ HCO &\Rightarrow CO + H \end{aligned}\right]$$ Equation 2.13

As mentioned previously, the species fed into the primary combustion zone are an array of radical species, light hydrocarbons, and low molecular weight organic compounds. The chain branching mechanisms and unimolecular decompositions in the pre-combustion

zone often result in stable fuel and product species, and the mixture is often approximated as a CO, CO_2, H_2, H_2O, and CH_4. While this allows for the use of simplified global reaction mechanisms, it is interesting that the important role of methyl and hydroxyl radicals traveling between the solid phase and the primary combustion zone is glossed over. Table 2.4 displays how similar studies have characterized this volatile fuel. Huttenen et al. compared a mixture-based four step global mechanism against a single fuel species empirically-based two step mechanism, unfortunately for which little comparative conclusions were drawn [31]. For CFD simulations, there are clear computational advantages when using a single fuel species rather than this mixture, however it is at a cost of modeling accuracy. Bhaskar et al. used formaldehyde as the fuel species in a CFD study of wood stoves, however an empirically derived heat of formation was used to represent the mixture as a whole, not that of formaldehyde [7].

Table 2.4: Approximations of Primary Combustion Fuel Mixture

Study	Species Mass Fractions				
	CO	CO_2	H_2	H_2O	CH_4
Galgano [25]	0.383	0.237	0.006	0.312	0.062
Huttenen [31]	0.372	0.256	0.023	0.215	0.132
	0.410	0.161	0.014	0.269	0.146
	$CH_{2.12}O_{0.94}$				
Dixit [7]	CH_2O h_f = -267 MJ/kmol				

Initial testing suggests that complete combustion is not achieved, which is to be expected for any real process, thus species other than CO_2 and H_2O leave the primary combustion zone into a post-combustion zone. CO oxidation is limited by the presence of hydroxyl radicals, seen in equation 2.14 [48]. Turns also recognizes the importance of hydrogen noting that "the CO oxidation step involving the hydroxyl radical is much faster than the steps involving O_2 and O" [49]. As the exhaust gases approach the heat transfer area of the OWHH, heat removing third body collisions will recombine hydroxyl and hydrogen atom radicals into water vapor.

$$\left.\begin{aligned} HCO + OH &\Rightarrow CO + H_2O \\ CO + OH &\Rightarrow CO_2 + H \end{aligned}\right] \quad \text{Equation 2.14}$$

The global mechanisms used in the abovementioned studies are outlined in Table 2.5, with kinetic parameters to be discussed in the modeling section. With the mixture or single molecule based fuels in Table 2.4 as an approximation of the resulting species from the pre-combustion zone, these mechanisms are to describe all reactions taking place through the primary and post-combustion zones. Neither scheme includes the hydroxyl radical for brevity, however the water-gas shift reaction, the fourth in both schemes, represents the influence of hydrogen over CO oxidation.

Table 2.5: Four Step Global Mechanisms

Study	Mechanism
Galgano [24]	$CO + \frac{1}{2}O_2 \Rightarrow CO_2$ $H_2 + \frac{1}{2}O_2 \Rightarrow H_2O$ $CH_4 + 2O_2 \Rightarrow CO_2 + 2H_2O$ $CO + H_2O \Leftrightarrow CO_2 + H_2$
Huttenen [31]	$CH_4 + \frac{1}{2}O_2 \Rightarrow CO + 2H_2$ $CH_4 + H_2O \Rightarrow CO + 3H_2$ $H_2 + \frac{1}{2}O_2 \Rightarrow H_2O$ $CO + H_2O \Leftrightarrow CO_2 + H_2$

2.1.3.4 Char Oxidation

A layer of char, or porous carbon, forms quite early in the burn on the outer layer of the cordwood or test crib. While char is not completely carbon, oak char being composed of 85.4% C by weight with ash, H, and N remaining, it is often approximated as such and the remaining substances treated as inert [1]. It is not until the pyrolyzed volatiles, 77-86% of the dry wood weight, are driven off that char oxidation dominates the behavior of the burn. The dynamics are familiar when we recall the burning of a charcoal briquette, with significantly less moisture and volatiles than wood, it will have a brief luminous flame during the pyrolysis dominated stages and then become a hotter glowing briquette during the char oxidation dominated stage. This stage is mass diffusion limited, and the main reaction is

shown in equation 2.15 [26]. This highly endothermic reaction initiates char oxidation at the porous char surface [48]. Hydrogen may also play a catalytic role, similar to that of the hydroxyl radicals in the previous stage, as seen in equation 2.16 [24]. As the char oxidation stage dominates, the burn rate will slow down dramatically as illustrated in Figure 2.12 [4], which experimentally this coincides with a smokeless exhaust.

$$C + CO_2 \Rightarrow 2CO \qquad \text{Equation 2.15}$$

$$C + H_2O \Rightarrow H_2 + CO \qquad \text{Equation 2.16}$$

Figure 2.12: Burn Rate for Volatile and Char Oxidation Dominated Stages [4]

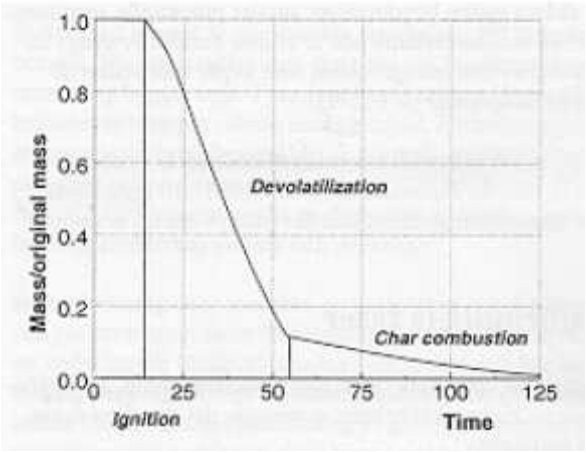

2.2 Particulate Matter Formation and Oxidation

Particulate matter may come from two sources during the combustion of wood, carbonaceous PM will form as a result of incomplete combustion and other PM will form around inorganic substances in the fuel. There is little to be done about preventing the formation of the latter PM source for OWHHs that does not involve fuel conditioning, therefore this study will concentrate on the former and "PM" will refer to carbonaceous PM only.

2.2.1 PM Formation Theory

Within the classification of carbonaceous PM, there exist two subclasses, split by composition and radiative characteristics into black carbon and brown carbon. Great attention has been paid recently for correct identification and specific labeling of these two subclasses as a result of lax use of terminology. Black carbon, also commonly known as soot or elemental carbon, may form with the combustion of any carbonaceous fuel ranging from methane to coal. Soot forms on the fuel side of the flame and escapes through gaps in the flame caused by excessive strain or localized quenching. Soot is composed of hollow spheres, or spherules, composed of graphene sheets with diameters of roughly 10 to 50 nm. These spherules are effectively char particles that agglomerate into irregularly shaped fractal-like structures, such as those seen in Figure 2.13. This agglomeration happens in areas with temperatures below that of the primary combustion zone [3].

Figure 2.13: Image of Soot Particles[2]

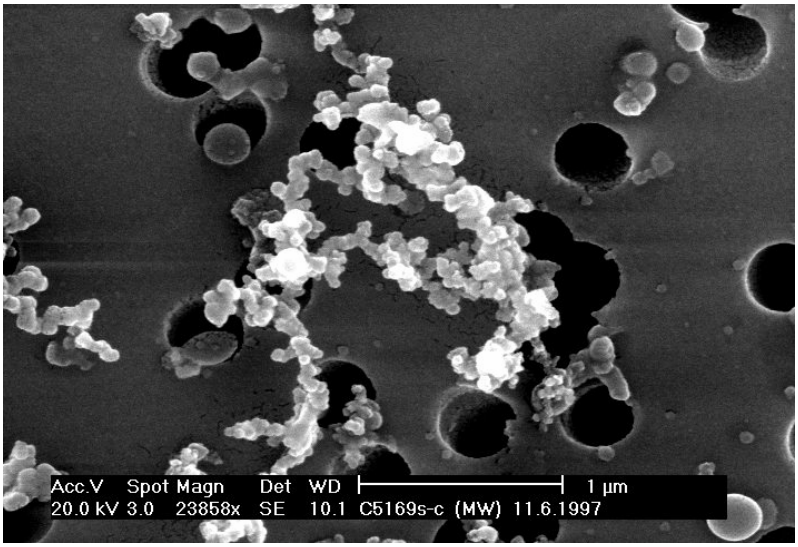

Brown carbon, or organic carbon, from biomass combustion is composed of condensed tars and the so-called humic-like substances (HULIS). HULIS is a class of fine aerosols from biomass combustion of unknown composition, but behave optically like humic substances such as peat and dark soils. Visibly, brown carbon appears brown to

[2] http://www.mpch-mainz.mpg.de/~gth/soot_aerosol.htm

yellowish and is generally produced by the pre-combustion zone pyrolysis products escaping through the primary combustion zone and condensing in the cooling exhaust plume [3].

In a study of fine particle emissions from residential fireplaces, Fine et al. determined that for Northern Red Oak, a close relative of White Oak used for the test crib, organic carbon was 90% and elemental carbon was 4% of the total particle mass [20]. The mass balance of the organic carbon is further broken down in Figure 2.14, where UCM stands for unknown complex mixture. While most of the organic compounds of this study were not identified, it is interesting to note that the largest known species is levoglucosan which is a direct pyrolysis product of cellulose [20]. This is not only due to cellulose being the largest fraction of wood, but also that its pyrolysis temperature is higher than hemicellulose and lignin.

Figure 2.16: Breakdown of Organic Carbon by Mass [20]

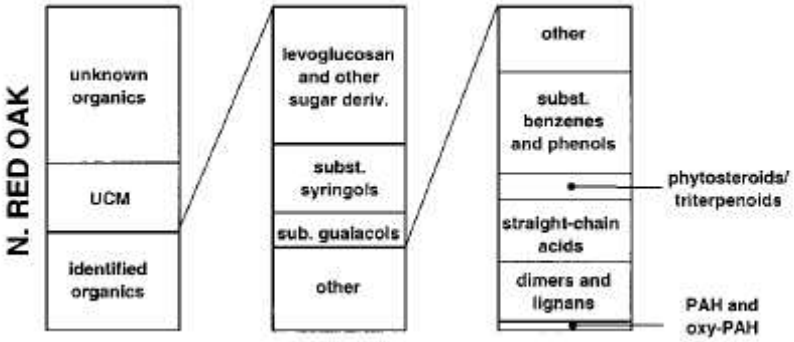

As noted by Fitzpatrick et al., a major distinction of organic carbon over black carbon aerosols is the presence of bound oxygen, due to the tars arising from the solid phase pyrolysis product mixture. This study reported a thorough listing of the 26 aromatic compounds found in the black carbon, or soot, aerosols from pine wood combustion and also noted the highly polar, and thus hydrophilic, nature of biomass smoke. The study proposes overall pathways from which black carbon (soot) and organic carbon (oxygenated soot) originate. During the gas phase pyrolysis, black carbon forms from unburned hydrocarbons which become aromatic radical compounds. They then condense to polycyclic aromatic hydrocarbons (PAH) known as precursors to soot, such as pyrene and anthracene seen in Figures 2.15 and 2.16 respectively, and then form soot upon further

agglomeration. Completion of this pathway is favored during higher temperature pyrolysis. Along that pathway, the aromatic radical compounds or PAHs may be oxidized to oxygenated soot, or organic carbon. Oxygenated PAHs also can be formed directly by the pyrolysis of the tars released during solid phase pyrolysis, which also create organic carbon [21].

Figures 2.15 & 2.16: Pyrene and Anthracene Structure

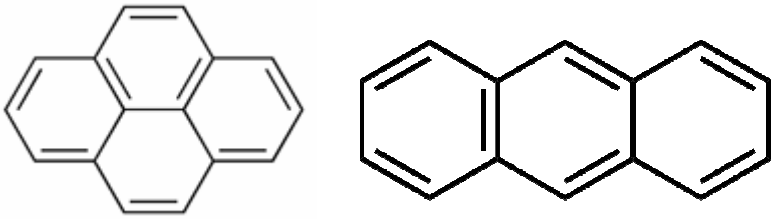

2.2.2 PM Formation and Combustion Modeling

A comprehensive theory or model of soot formation for laminar diffusion flames does not yet exist, and models of a singular case of turbulent methane-air diffusion flames have trouble creating reasonable predictions. Additionally, fundamental knowledge of organic carbon formation is just beginning to be understood through experimentation as discussed above.

One soot formation and combustion model has received considerable attention, the groundbreaking study by Magnussen and Hjertager (1976), studying turbulent diffusion flames [37]. The study related the soot formation and oxidation work of Tesner et al. to their eddy dissipation model of turbulent combustion [46]. The premise of the eddy dissipation model is that "because chemical reactions are very fast, it can be assumed that the rate of combustion will be determined by the rate of intermixing on a molecular scale of fuel and oxygen eddies, in other words, by the rate of dissipation of the eddies". This will be discussed in further detail in later sections.

The Tesner model is a two-step soot formation model, separating the formation of radical nuclei from the nucleation or agglomeration step, in contrast to popular one step soot models. The formation of the nuclei step may be thought as the PAH formation discussed earlier. This step is outlined in equation 2.17, which in words is the spontaneous generation

of radical nuclei, a first order Arrhenius rate expression defined separately in equation 2.18 dependent on local fuel concentration, minus the difference between the linear branching and termination coefficients multiplied by the local radical nuclei concentration minus the coefficient of linear termination of soot particles multiplied by the local radical nuclei and soot particle concentrations. The soot formation step is defined in a similar way as seen in equation 2.19, where a and b are constants and m_p is the soot particle mass [46, 22].

$$R_{n,f} = n_o + (f - g)n - g_o nN \qquad \text{Equation 2.17}$$

$$n_o = a_o C_f \exp\left(-E_a / RT\right) \qquad \text{Equation 2.18}$$

$$R_{s,f} = m_p (a - bN)n \qquad \text{Equation 2.19}$$

The soot and radical nuclei combustion are modeled similarly to that of the overall combustion within the eddy dissipation model. Two reaction rates are computed and the lower is used, one for the standard eddy dissipation form and the second accounting for low local oxygen concentrations. The combustion rate of radical nuclei is then computed as a function of the soot combustion rate and the ratio of the local nuclei and soot concentrations. The study showed good correlation with several acetylene-air turbulent diffusion flame data sets, with the aid of the empirical constants and assumed soot and radical nuclei parameters [46].

More recent soot formation and oxidation models have not strayed very far from the work of this study, including the work of Kronenburg and Bilger, and the one-step model of Khan and Greeves [38, 22]. There remains much work to be done, as a computational soot model grounded in physics that is not semi-empirical has not yet been developed [38]. That said, several gaps must be bridged when applying a soot formation and combustion model to the operation of OWHHs. First and foremost, these models predict the formation of soot only, or black carbon, and the majority of PM expected is organic carbon formed through a different pathway. Secondly, the empirical constants used in the development of these models are fit to well defined, steady-state, momentum driven, unimolecular light hydrocarbon flames whereas OWHHs produce chaotic, transient, buoyancy driven, heterogeneous organic matter fueled flames. Lastly, the errors generated between these soot

models and the studies that they were applied to are also carried over. Therefore the use of these soot models to capture the formation and combustion of soot and organic carbon in the OWHH will be exercised sparingly and judiciously.

2.3 Heat Transfer

Within an OWHH, especially the Model 100 for which the firebox is composed of refractory brick, none of the three forms of heat transfer: convection, conduction, and radiation, may be ignored. As discussed during the solid phase pyrolysis section, radiation is the feedback mechanism that drives wood combustion and largely how the preheated firebox begins the wood heating and drying stage. Convection is dominant in many portions of the OWHH: the preheating of primary and secondary air, the reheating of the refractory brick, and heat transfer to the water tubes, which is the purpose of the OWHH. While important to the movement of the pyrolysis and drying fronts within the wood and key to assessing the OWHH's heat loss through the exterior, conduction will be less of a focus of this study but not ignored.

The well known classical relationships of heat transfer of these three modes are the Stefan-Boltzmann Law, Newton's Law of Cooling, and Fourier's Law of Heat Conduction (in the x-direction), outlined in equations 2.20, 2.21, and 2.22 respectively. The radiation and convection equations are written for surface heating, as that will often be the case. Where discretion comes into play is the determination of the phenomenological parameters ε, k, and especially h. This is to be discussed during the modeling section of this study.

$$q''_{rad} = \varepsilon\sigma_b\left(T_\infty^4 - T_s^4\right) \quad \text{Equation 2.20}$$

$$q''_{conv} = h\left(T_\infty - T_s\right) \quad \text{Equation 2.21}$$

$$q''_{cond,x} = -k\frac{\partial T}{\partial x} \quad \text{Equation 2.22}$$

2.4 Fluid Mechanics of Buoyancy-Driven Diffusion Flames

The fluid flow within the OWHH may be completely described by the Navier-Stokes equations of mass and momentum conservation, as shown in equations 2.23 and 2.24. The equations are in conservative and index form and the momentum equation includes a gravitational body force source term, g_i, with the viscous stress tensor as defined in equation 2.25, assuming that the gases are Newtonian fluids. Reacting flows and especially buoyancy-dominated diffusion flames are dilatational, that is characterized by expansion with density gradients that are large compared to non-reacting flows. Thus, the divergence of the velocity field may not be approximated as zero. This effect is seen by the retention of the density gradients within the continuity equation, equation 2.23, and the retention of the dilatational expansion term as a momentum sink, second in the stress tensor definition. However we may treat the flow field as incompressible, as the ideal gas law is a good approximation for the hot gases within the OWHH, as the density does not change with pressure.

$$\frac{\partial \rho}{\partial t} + \frac{\partial}{\partial x_j}\left(\rho u_j\right) = 0 \qquad \text{Equation 2.23}$$

$$\frac{\partial}{\partial t}\left(\rho u_i\right) + \frac{\partial}{\partial x_j}\left(\rho u_i u_j\right) = -\frac{\partial p}{\partial x_i} + \frac{\partial \tau_{ij}}{\partial x_j} + g_i \qquad \text{Equation 2.24}$$

$$\tau_{ij} \equiv 2\mu S_{ij} - \frac{2}{3}\mu \frac{\partial u_k}{\partial x_k}\delta_{ij} = \mu\left(\frac{\partial u_i}{\partial x_j} + \frac{\partial u_j}{\partial x_i}\right) - \frac{2}{3}\mu \frac{\partial u_k}{\partial x_k}\delta_{ij} \qquad \text{Equation 2.25}$$

Specifically, the fire within the OWHH may be thought of as a buoyancy-driven diffusion flame from the perspective of the flow field. Despite its lazy nature and low frequencies associated with its flow fluctuations, it is often fully turbulent. Due to the absence of a large momentum flux (i.e. a jet), the density gradients cause prominent instabilities that can aid or inhibit reactant mixing, thermal transport, local turbulence, and flame quenching among other mechanisms. The study of buoyancy-dominated diffusion flames reveals a tight coupling between the smallest dissipative and the largest rotational scales of motion, fundamental importance of the global forcing mechanism of buoyancy on

momentum and thermal transport, and how throughout the course of a burn many competing phenomena both promote and retard complete combustion. Therefore the flow field is of paramount importance, due to its connection to reaction kinetics, scalar transport, and heat transfer. While integral to modeling of the OWHH, especially with respect to the pyrolysis and drying stages, the radiation portion of the heat transfer and flow field coupling is to be ignored. This is because time scales for radiative transport are so small that the flow is effectively stationary [47].

2.4.1 Buoyant Reacting Plumes: Theory & Experimental Evidence

Buoyant plumes are jets that rise with respect to the gravitational vector as a result of density gradients. In the case of fires the density gradients are a result of volumetric heat release. Helium or other lighter-than-air substances are commonly studied to isolate buoyancy effects on plumes from the changing composition as a result of reactions. This mechanism produces a majority of the entrainment, or convective mixing of air in the case of OWHHs, by introducing large scale instabilities which in turn drives the vorticity field at the mixing layer interface. As the plume rises, a shear layer develops at the edge, forming due to the large horizontal density gradient. This increases turbulent intensities, or magnitudes of fluctuating variables, and greatly increases the species and thermal transport. However, the more that the plume expands isotropically, angular momentum conservation requires that the eddy rotation rates at this shear layer must be reduced. Additionally in the case of reacting buoyant plumes, the temperature increase that causes this expansion will increase the eddy viscosities, further reducing shear layer mixing [47].

A familiar effect of buoyancy on entrainment of the surrounding fluid is the low frequency puffing exhibited by fires. This characteristic puffing is so integral in the study of these flows, that researchers will integrate over a puffing 'cycle' for time-averaged values. Counterintuitively, this mechanism is not a function of combustion instabilities and is independent of thermal transport. Buoyant isothermal helium plumes have shown the same puffing behavior [47]. The plume will puff as a result of periodic toroidal vortex shedding, as a result of the competition between dilatation and the shear layer discussed previously. At the plume edge, a baroclinic torque develops, which is defined as the cross product of the

pressure and density gradients. This torque is responsible for the instabilities that create this vortex shedding, from the large rotational structures down to diffusional vortices over a 'length scale cascade'.

These effects have been experimentally verified, as the acquisition of data from buoyant plumes in a quiescent atmosphere is easier than that of a high temperature combustor. However, buoyant flames when compared to their jet cousins are more chaotic, less reproducible, and time and density-averaged values are less straightforward to determine. Therefore the preferred method is to study buoyancy-dominated jet diffusion flames. Muniz et al. compared a momentum driven and buoyancy driven reacting jet to a non-reacting jet of the Reynolds number matching the buoyancy driven jet. Axial and radial turbulent intensities, seen as normalized velocity fluctuations, are at a minimum much closer to the fuel source for the momentum than the buoyancy driven reacting jet. Additionally these intensities reach a maximum at the flame tip for the momentum driven jet and beyond the flame tip for the buoyancy driven jet with larger magnitude intensities. The initial minimum is due to reduced Re_D, with the delayed dip for the buoyant jet due to a large density gradient. The eventual rise in turbulent intensities towards the flame tip is evidence of the buoyancy induced instabilities discussed earlier reaching a maximum at the higher temperatures. The corresponding intensities for the isothermal non-reacting buoyant jet were consistently higher than either reacting jet, evidence of the effect of increased eddy viscosities and greater dilatation rates [38].

2.4.2 Combustion Theory and Modeling

As discussed previously in the gas phase pyrolysis and oxidation section, combustion is characterized by formation of free radical species in a high temperature environment via chain branching and eventual termination reactions that lead to product species. These final reactions are highly exothermic and are the source of much of the heat release. To incorporate this phenomenon into a complete fluid dynamic description, the energy conservation equation, in the form of an enthalpy equation, along with the species transport equations must be added to the Navier-Stokes equations, seen in equations 2.23 and 2.24. The energy conservation equation, equation 2.26, tracks the time rate of change of enthalpy

per unit mass for a fluid parcel, accounting for mean flow advection, instantaneous time derivatives of pressure from waves, fluid heat conduction, and a radiation source term. This form of energy conservation assumes velocities are low enough such that viscous dissipation is negligible, concentration gradients are low enough to cause negligible heat fluxes, and that the mixture kinetic energy is small compared to the mixture enthalpy [15]. It is also unlikely that significant pressure waves will develop within the OWHH, therefore the first term on the right hand side is likely to play an insignificant role. The mixture heat capacity, C_p, is a local mass weighted average. The species transport is formulated similarly, which tracks the time rate of change of the mass fraction of species α for a fluid parcel, accounting for mean flow advection, Fickian diffusion, and species destruction or creation via reactions. Equation 2.27 is known as the Shvab-Zeldovich equation.

$$\frac{\partial}{\partial t}(\rho h)+\frac{\partial}{\partial x_j}(\rho u_j h)=\frac{\partial p}{\partial t}+\frac{\partial}{\partial x_j}\left(\frac{k}{C_p}\frac{\partial h}{\partial x_j}-\dot{q}_j^R\right) \qquad \text{Equation 2.26}$$

$$\frac{\partial}{\partial t}(\rho X_\alpha)+\frac{\partial}{\partial x_j}(\rho u_j X_\alpha)=\frac{\partial}{\partial x_j}\left(\rho D\frac{\partial X_\alpha}{\partial x_j}\right)+S_\alpha \qquad \text{Equation 2.27}$$

Noting the wide array of species expected to participate in gas phase pyrolysis and oxidation and the resulting product species as well, it seems unreasonable to simultaneously solve a species transport equation for each of them. For the simple case of a single global reaction, each species source term requires an additional Arrhenius rate expression, shown in the general form in equation 2.28 for species α and an involved species β. If multiple reactions are modeled, this source term will incorporate the destruction and creation of species α from each reaction and equation 2.28 will become a summation over all reactions.

$$S_\alpha = M_\alpha A T^b \exp\left(-\frac{E_A}{RT}\right)C_\alpha C_\beta \qquad \text{Equation 2.28}$$

Use of a global mechanism, such as those outlined in Table 2.5, would allow the use of only six species conservation equations for CO, CO_2, H_2O, H_2, CH_4, and O_2. The

seventh inert species, in this case nitrogen, would not need its own equation, as it may be arithmetically determined as the remaining mass fraction of each fluid parcel. Additionally, disassociation of CO_2 into O_2 and CO is not expected to be significant as it is in higher temperature combustion environments. The equilibrium mole fraction CO_2 at 1500 K and 1 atm is 0.9994 [49], which is close to the Model 100's record internal temperature of 1489 K. While this method is essential in the modeling of finite rate chemistry, for just one dimensional laminar flow this approach requires the simultaneous solution of a system of nine equations!

2.4.2.1 The Mixture Fraction Model

The pioneering work of Burke and Schumann [10] and further refinement by Bilger [6] led to an elegant approach to this problem by defining the mixture fraction, Z. Burke and Schumann experimentally examined flat flames and mathematically determined the location of the flame surface through by use of new scalar variable, and also coined the term 'diffusion flame'. Thinking of oxygen as a 'negative fuel', they tracked the fuel molar concentration and eliminated the source term. They assumed that combustion is mixing limited only and reactions between the fuel and oxidizer are irreversible and infinitely fast, thus fuel and oxidizer do not coexist. This is also known as the 'fast-chemistry assumption'. Converting equation 2.27 to one-dimensional radial coordinates and molar concentrations, the fuel concentration field was analytically solved using Bessel's functions. This scalar representing the stoichiometric mixture was defined as in equation 2.29, where the concentration is defined as the initial concentration of the fuel added to the negative concentration of oxygen over the molar oxygen to fuel ratio. Analytically determining the flame location at the surface of stoichiometric fuel concentration, $C = C_o$, of a round jet flame yielded good results when compared to experimental observations. This analysis was for steady state radial diffusion only and the upper limit of the conserved scalar C was problem dependent, thus normalization would be required to have a better analogy to species mass and mole fractions [10].

$$C_o = C_F + \frac{C_O}{i}$$ Equation 2.29

Bilger simplified this analysis by implementing the abovementioned normalization and is often credited with creating the mixture fraction model as it is used today. By design it is desired that the mixture fraction have a range of values between zero and one, where the bounds represent the pure fuel and pure oxidizer. This normalized mixture fraction for a two stream system is defined in equation 2.30, which numerically tracks the local mixture fraction of mass which originated in stream 1 [6].

$$Z = \frac{\dot{m}_1}{\dot{m}_1 + \dot{m}_2}$$ Equation 2.30

As described by Peters, this can be applied to the generic reaction in equation 2.31. Conserving mass, the relative differential change in fuel and oxygen mass fractions is outlined in equation 2.32. This may be integrated between the unburnt initial state and an arbitrary state to reach equation 2.33. It is evident that *s* is defined as the stoichiometric oxygen to fuel mass ratio. As we are concerned with mass fractions rather than mass, Z may eventually include inert species in either stream, such as N_2 [41].

$$\nu_F Fuel + \nu_O O_2 \Rightarrow products$$ Equation 2.31

$$\frac{dX_F}{\nu_F M_F} = \frac{dX_O}{\nu_O M_O}$$ Equation 2.32

$$sX_F - X_O = sX_{F,u} - X_{O,u}, \qquad s = \frac{\nu_O M_O}{\nu_F M_F}$$ Equation 2.33

Assuming that the fuel, oxidizer, and any background inert species have equal diffusivities, which is reasonable for high temperature gases, the unburnt mass fractions may be expressed in terms of Z. Using equation 2.30 with stream 1 as fuel and 2 as air, Z represents the mixture fraction of the unburnt mass from the fuel stream and (1-Z) represents that from the air stream. These relationships yield equations 2.34 and 2.35, which when returning to equation 2.33 yields equation 2.36, where 1 and 2 denote the initial

boundary mass fractions. For the equivalence ratio, defined in equation 2.37 as the ratio of actual fuel to air mass ratio to that of a stoichiometric mixture, we see a ratio greater than one implies rich conditions and less than one implies lean conditions. Reexamining equation 2.31 from a mass basis allows Z to be defined in terms of this ratio in equation 2.38. Peters notes that the mixture fraction may be thought of as normalized local equivalence ratio [41].

$$X_{F,u} = X_{F,1} Z \qquad \text{Equation 2.34}$$

$$X_{O,u} = X_{O,2}(1 - Z) \qquad \text{Equation 2.35}$$

$$Z = \frac{sX_F - X_O + X_{O,2}}{sX_{F,1} + X_{O,2}} \qquad \text{Equation 2.36}$$

$$ER = \frac{\left(Fuel/Air\right)}{\left(Fuel/Air\right)_{stoich}} \qquad \text{Equation 2.37}$$

$$Z = \frac{ER}{ER + s} \qquad \text{Equation 2.38}$$

To determine the stoichiometric mixture fraction, where the flame sheet is located, it is noted that the fuel and oxidizer are totally consumed at the stoichiometric interface, thus $X_F = X_O = 0$.

$$Z_{st} = \frac{sX_{F,1}}{sX_{F,1} + X_{O,2}} = \left[1 + \frac{sX_{F,1}}{X_{O,2}}\right]^{-1} \qquad \text{Equation 2.39}$$

Rather than employing a species transport Shvab-Zeldovich equation for each species, the mixture fraction transport equation in equation 2.40 may be used. In addition to the requirement of equal diffusivities between species, the unity Lewis number assumption is also made, requiring equal thermal diffusivities amongst species as well. This progression, seen preceding equation 2.40, allows the use of dynamic viscosity and the local Prandtl number in the place of the mass diffusivity, which are functions of the flow field variables. Assuming equilibrium chemistry, the local temperature (thus density) and species mass fractions are functions of the mixture fraction.

$$Le = \frac{\alpha}{D} = 1;\ \rho D = \rho\alpha = \rho\frac{k}{\rho C_p} = \frac{k}{C_p} = \frac{k}{C_p}\frac{\mu}{\rho\nu} = \frac{\mu\alpha}{\nu} = \frac{\mu}{\mathrm{Pr}}$$

$$\frac{\partial}{\partial t}(\rho Z) + \frac{\partial}{\partial x_j}(\rho u_j Z) = \frac{\partial}{\partial x_j}\left(\rho D\frac{\partial Z}{\partial x_j}\right) = \frac{\partial}{\partial x_j}\left(\frac{\mu}{\mathrm{Pr}}\frac{\partial Z}{\partial x_j}\right) \qquad \text{Equation 2.40}$$

Many flames, including those within an OWHH, are markedly transient in behavior and the assumption of equilibrium produces large errors. To account for this, Bilger returned to the Shvab-Zeldovich equation and kept the source term to assess the effect on reaction rates [6]. As all species mass fractions are only functions of the mixture fraction, fuel is examined. Combining the transport of the fuel mass fraction with its relation to Z, equations 2.27 and 2.34 and noting that X_F is only a function of Z, yields the equation 2.41 [50]. The grouping in equation 2.42 represents the scalar dissipation rate, χ, which has dimensions of inverse time. For non-equilibrium flames, this so-called 'flamelet' approach accounts for transient behavior and finite reaction rates [50].

$$S_F = -\rho D\frac{d^2 X_F}{dZ^2}\left|\nabla Z\right|^2 \qquad \text{Equation 2.41}$$

$$\chi = 2D\left|\nabla Z\right|^2 \qquad \text{Equation 2.42}$$

2.4.3 Turbulence Modeling of the Flow Field

The equations of interest for fluid dynamics modeling of an OWHH are summarized in Table 2.6, with the two options for chemistry modeling included. As discussed in the theory of reacting and non-reacting buoyant plumes, the effect of turbulence is vital to describing the physics of the flow field. These fluctuations are not explicitly accounted for, and the only means in which to capture their effects is to use Direct Numerical Simulation (DNS) techniques which are beyond the computational and technical scope of this study, and perhaps the current CFD field. Therefore, modeling of turbulence is required. To capture the buoyancy-induced turbulence, care must be exercised. As more physics is incorporated and complex chemistry modeled, there are more assumptions, fitting

parameters, and phenomenological laws needed that cause a distinct loss of simplicity and universality. Peters sums this up by noting that "this semiempirical nature of turbulence modeling puts them into the category of an art rather than a science" [41].

Table 2.6: Governing Equations for Laminar Regime

Equation Name		Equation
Continuity		$\frac{\partial \rho}{\partial t} + \frac{\partial}{\partial x_j}\left(\rho u_j\right) = 0$
Momentum		$\frac{\partial}{\partial t}\left(\rho u_i\right) + \frac{\partial}{\partial x_j}\left(\rho u_i u_j\right) = -\frac{\partial p}{\partial x_i} + \frac{\partial \tau_{ij}}{\partial x_j} + g_i$; $\tau_{ij} \equiv \mu\left(\frac{\partial u_i}{\partial x_j} + \frac{\partial u_j}{\partial x_i}\right) - \frac{2}{3}\mu\frac{\partial u_k}{\partial x_k}\delta_{ij}$
Energy		$\frac{\partial}{\partial t}\left(\rho h\right) + \frac{\partial}{\partial x_j}\left(\rho u_j h\right) = \frac{\partial p}{\partial t} + \frac{\partial}{\partial x_j}\left(\frac{k}{C_p}\frac{\partial h}{\partial x_j} - \dot{q}_j^R\right)$
Species	General	$\frac{\partial}{\partial t}\left(\rho X_\alpha\right) + \frac{\partial}{\partial x_j}\left(\rho u_j X_\alpha\right) = \frac{\partial}{\partial x_j}\left(\rho D\frac{\partial X_\alpha}{\partial x_j}\right) + S_\alpha$
	Mixture Fraction	$\frac{\partial}{\partial t}\left(\rho Z\right) + \frac{\partial}{\partial x_j}\left(\rho u_j Z\right) = \frac{\partial}{\partial x_j}\left(\frac{\mu}{\mathrm{Pr}}\frac{\partial Z}{\partial x_j}\right)$

Decomposition of the variables modeled: ϱ, u, h, and X_α or Z, into averaged and fluctuating components is required to begin. Typically, this is done on a time averaged basis, forming the so called Reynolds Averaged Navier-Stokes (RANS) equations. However, due to large density gradients within the OWHH and subsequent use of the non-solenoidal form of the continuity equation, density averaged variables must be used to for the so called Favre Averaged Navier-Stokes (FANS) equations. Density averaging is outlined in equations 2.43 and 2.44, for the variable Φ where $\tilde{\Phi}$ is the density-weighted time average of the variable. An overbar denotes a quantity that is identical to the Reynolds, or time, averaged quantity [25].

$$\Phi(\mathbf{x},t) \equiv \tilde{\Phi}(\mathbf{x},t) + \Phi''(\mathbf{x},t) \qquad \text{Equation 2.43}$$

$$\tilde{\Phi}(\mathbf{x},t) \equiv \frac{\int_T \rho(\mathbf{x},t)\Phi(\mathbf{x},t)dt}{\int_T \rho(\mathbf{x},t)dt} \equiv \frac{\overline{\rho\Phi}}{\overline{\rho}} \qquad \text{Equation 2.44}$$

(note: $\overline{\rho u} = \overline{\rho}\tilde{u}$)

The decomposed variables are returned to the equations in Table 2.6, with the exception of the mixture fraction conservation equation. The whole equations are averaged, and the known properties of averaged variables are used are used to simplify. While it remains that the average of a fluctuating variable is zero, it is important to note that the variable in question is the density averaged velocity. In other words: $\overline{\rho u_j"} = 0$ and $\overline{u_j"} \neq 0$. The resulting FANS equations including enthalpy and species transport are in Table 2.7, noting that the mean viscous stress tensor is in terms of averaged velocities.

Table 2.7: Favre Averaged Navier Stokes Equations with Enthalpy and Species Transport

Equation Name	Equation
Continuity	$\frac{\partial \overline{\rho}}{\partial t} + \frac{\partial}{\partial x_j}\left(\overline{\rho}\tilde{u}_j\right) = 0$
Momentum	$\frac{\partial}{\partial t}\left(\overline{\rho}\tilde{u}_i\right) + \frac{\partial}{\partial x_j}\left(\overline{\rho}\tilde{u}_i\tilde{u}_j\right) = -\frac{\partial \overline{p}}{\partial x_i} + \frac{\partial}{\partial x_j}\left(\overline{\tau}_{ij} - \overline{\rho u_i" u_j"}\right) + \overline{g}_i;$
Energy	$\frac{\partial}{\partial t}\left(\overline{\rho}\overline{h}\right) + \frac{\partial}{\partial x_j}\left(\overline{\rho}\tilde{u}_j\overline{h}\right) = \frac{\partial \overline{p}}{\partial t} + \frac{\partial}{\partial x_j}\left(\frac{k}{C_p}\frac{\partial \overline{h}}{\partial x_j} - \overline{\rho u_j"h"}\right) - \frac{\partial \dot{q}_j^R}{\partial x_j}$
Species	$\frac{\partial}{\partial t}\left(\overline{\rho}\tilde{X}_\alpha\right) + \frac{\partial}{\partial x_j}\left(\overline{\rho}\tilde{u}_j\tilde{X}_\alpha\right) = \frac{\partial}{\partial x_j}\left(\overline{\rho D\frac{\partial X_\alpha}{\partial x_j}} - \overline{\rho u_j" X_\alpha"}\right) + \overline{S}_\alpha$

While the equation set in Table 2.6 is a closed set with a state relation (the Ideal Gas Law), Table 2.7 is not and additional equations, assumptions, and models are needed to overcome this closure problem. The fluctuating terms within the second to last groupings in the Momentum, Energy, and Species are known as turbulent transport terms and cause this closure problem.

The turbulent transport term in the Momentum equation is the Reynolds stress tensor, and its treatment is the basis of each turbulence model. The typical operating

conditions of the OWHH and need for combustion modeling limits the range of turbulence models that may be applied. As previously mentioned, DNS techniques are beyond the scope of this study and turbulence modeling is required. For i ≠ j, there are six Reynolds stresses that may be modeled directed with six transport equations or further simplified by making assumptions in a so called Reynolds Stress Model. The improved capture of near wall effects are not justified for this computational expensive, as the flow field within the OWHH is poorly defined and chaotic. Additionally, in the absence of large pressure gradients, with low Mach numbers, and small viscous effects, the k-ω model is not needed. The k-ω model solves the turbulent kinetic energy and turbulent frequency transport equations [42]. The two turbulence models that are to be examined in this study are the prevalent k-ε model and its variations, and Large Eddy Simulation (LES).

2.4.3.1 The k-ε Model

To solve the closure problem presented by the Reynolds stress tensor, it is often assumed that at the turbulent microscales, pressure and density fluctuations are insignificant such that parameters involved in turbulence are Reynolds averaged. Sonic and supersonic flows would require the use of density averaged parameters at this small scale. Therefore, it is commonly assumed that at this scale the time and density averaged fluctuating velocities are equivalent. This approximation allows for the density within the Favre averaged Reynolds stress term to be decoupled, for example the $\overline{\rho u_i'' u_j''}$ term in the momentum equation is approximated as $\bar{\rho}\overline{u_i'' u_j''}$. This allows for application of the turbulent viscosity hypothesis and the Boussinesq approximation [22]. The following discussion of the k-ε model's development includes this approximation, therefore the density averaged velocity will represent the turbulent fluctuating component.

To address the turbulent viscosity hypothesis, the turbulent kinetic energy, is defined as half of the trace of the Reynolds stress tensor in equation 2.45. As k is a scalar quantity, a summation is implied. Pope distinguishes between the isotropic normal and anisotropic shear Reynolds stress components by defining the anisotropic component as in equation 2.46 [42].

$$k \equiv \tfrac{1}{2}\overline{u_i" \cdot u_i"} \qquad \text{Equation 2.45}$$

$$a_{ij} = \overline{u_i" u_j"} - \tfrac{2}{3} k \delta_{ij} \qquad \text{Equation 2.46}$$

The turbulent viscosity hypothesis postulates that the shear portions of the Reynolds stress tensor are directly proportional to the gradient of the normal component of velocity, much like that of Newton's law of viscosity. The constant of proportionality is defined as the turbulent kinematic viscosity, ν_T. As the Reynolds stress anisotropy defined in equation 2.46 is a tensor, it is proportional to the mean rate of strain tensor shown in equation 2.47. Notice the similarities to the definition of the shear stress tensor in equation 2.25 and the retention of the dilatational shear term at the end. This is also known as the Boussinesq hypothesis, or the eddy viscosity hypothesis.

$$a_{ij} = -\nu_T \left[\left(\frac{\partial \tilde{u}_i}{\partial x_j} + \frac{\partial \tilde{u}_j}{\partial x_i} \right) + \frac{2}{3} \frac{\partial \tilde{u}_k}{\partial x_k} \delta_{ij} \right] \qquad \text{Equation 2.47}$$

The turbulent transport of scalars, including k, is modeled using the gradient diffusion assumption. Like the turbulent viscosity hypothesis, this has a direct analogy to Fick's law of mass diffusion where a scalar flux is related to its gradient by its diffusivity. This may be summarized as in equation 2.48 [25]. With the unity Lewis number assumption, the scalar turbulent diffusivity is approximated as the ratio of the turbulent kinematic viscosity and the turbulent Prandtl number (or Schmidt number), which is empirically defined depending on the scalar quantity.

$$\overline{u_i" \phi"} = -\Gamma_\phi \frac{\partial \tilde{\phi}}{\partial x_i}; \qquad \Gamma_\phi \cong \frac{\nu_T}{\mathrm{Pr}_\phi} \qquad \text{Equation 2.48}$$

This modeling assumption requires an additional equation to model the transport of the turbulent kinetic energy and the turbulent kinematic viscosity must be modeled. The turbulent eddies which dissipate into the Reynolds stress anisotropy according to equation 2.47, are assumed to behave like particles in classical kinetic theory, that is transporting

momentum at a characteristic length and velocity scales [25]. The turbulent kinematic viscosity is empirically related to these scales ($k^{1/2}$ being the velocity scale) as in equation 2.49. The resulting turbulent kinetic energy transport equation is outlined in equation 2.50, where the right hand side terms in order are: the mean and turbulent diffusion of k, the destruction of k from mean velocity gradients, the destruction of k from buoyancy for ideal gases, and the viscous dissipation of k [22].

$$\nu_T = C_\mu' k^{1/2} l \qquad \text{Equation 2.49}$$

$$\frac{\partial}{\partial t}(\bar{\rho}k) + \frac{\partial}{\partial x_j}(\bar{\rho}\tilde{u}_i k) = \frac{\partial}{\partial x_j}\left(\left(\mu + \frac{\mu_T}{Sc_k}\right)\frac{\partial k}{\partial x_j}\right) - \bar{\rho}\overline{u_i" u_j"}\frac{\partial \tilde{u}_j}{\partial x_i} - g_i \frac{\nu_T}{Sc_k}\frac{\partial \bar{\rho}}{\partial x_i} - \nu\overline{\frac{\partial u_i"}{\partial x_j}}\overline{\frac{\partial u_i"}{\partial x_j}}$$

Equation 2.50

The final term in equation 2.50, the viscous dissipation of k, creates another closure problem. With some additional modeling assumptions and a transport equation this may be corrected. The dissipation of k, defined as ε, relates to the length scale of equation 2.49 by dimensional analysis in equation 2.51 which returned to equation 2.49 yields equation 2.52. The resulting transport equation of ε is outlined in equation 2.53 [22]. The terms on the right hand side of the transport equation have the same physical meaning as equation 2.50. The constant values and approximated turbulent Schmidt numbers are as follows: C_{1e} = 1.44, C_{2e} = 1.92, $C_{3e} \equiv \tanh|v/u|$, C_μ = 0.09, Sc_k = 1.0, Sc_e = 1.3 [36].

$$l = C_D \frac{k^{3/2}}{\varepsilon} \qquad \text{Equation 2.51}$$

$$\nu_T = C_\mu \frac{k^2}{\varepsilon} \qquad \text{Equation 2.52}$$

$$\frac{\partial}{\partial t}(\bar{\rho}\varepsilon) + \frac{\partial}{\partial x_j}(\bar{\rho}\tilde{u}_i \varepsilon) = \frac{\partial}{\partial x_j}\left(\left(\mu + \frac{\mu_T}{Sc_e}\right)\frac{\partial \varepsilon}{\partial x_j}\right) + C_{1e}\frac{\varepsilon}{k}\left(\bar{\rho}\overline{u_i" u_j"}\frac{\partial \tilde{u}_j}{\partial x_i} - C_{3e} g_i \frac{\nu_T}{Sc_e}\frac{\partial \bar{\rho}}{\partial x_i}\right) - C_{2e}\bar{\rho}\frac{\varepsilon^2}{k}$$

Equation 2.53

Further dimensional analysis reveals the relation of viscosity and ε to the Kolmogorov time and the length scales in equations 2.53 and 2.54 respectively. Physically these are scales of the smallest turbulent motions [42].

$$\tau_\eta = \left(\frac{\nu}{\varepsilon}\right)^{1/2} \qquad \text{Equation 2.53}$$

$$\eta = \left(\frac{\nu^3}{\varepsilon}\right)^{1/4} \qquad \text{Equation 2.54}$$

With the transport equations for k and ε, the equation set in Table 2.7 is closed and use of the k-ε model may commence. The ubiquity of the k-ε model in commercial codes has led to the illumination of its shortcomings. The primary source of its inaccuracies with respect to the OWHH lies in the use of the turbulent viscosity hypothesis. Within the use of this hypothesis is the inherent assumption of the isotropy of turbulence, which at smaller scales is not problematic. It is the capturing of the larger buoyancy-induced coherent turbulent structures that loses accuracy with this hypothesis. The k-ε model works well for diffusive turbulent transport, however convective turbulent thermal and scalar transport in the OWHH may be more significant. The statistical technique of the Renormalized Group (RNG) applied to the k-ε will be not explored, as its advantages in computational savings are outweighed by large errors in the modeling of wood combustion over the standard k-ε model [31].

2.4.3.2 Large Eddy Simulation

In a world of infinite computational resources, decomposition of variables in Table 2.6 and subsequent turbulence modeling would not be needed and the CFD simulation of an OWHH would be done with DNS. However, the constraints of reality limit the application of DNS, which computational expenses increase with the cube of the Reynolds number, to relatively simple geometries and low Reynolds numbers [42]. Recognizing that models using the turbulent viscosity hypothesis, like k-ε, work well at small scales, selective application of DNS at larger scales where this hypothesis breaks down is at the core of the Large Eddy

Simulation (LES) technique. This allows the assumption of isotropy to be restricted to smaller scales and for direct simulation of the large eddies, which are on the scale of the mean flow.

Rather than decompose variables into mean and fluctuating components by time or density averaging, LES employs an analogous filtering technique decomposing the variables into filtered and subgrid components as seen in equation 2.55 [42]. The filtered component, with use of a finite-volume simulation, is defined as in equation 2.56 [22], where $\mathbf{x}' = \mathbf{x} - \mathbf{r}$, which limits the filtering to υ, the cell domain, and V is the cell volume.

$$\Phi(\mathbf{x},t) = \overline{\Phi}(\mathbf{x},t) + \Phi'(\mathbf{x},t) \qquad \text{Equation 2.55}$$

$$\overline{u}(\mathbf{x},t) = \frac{1}{V}\int_{\upsilon} u(\mathbf{x}',t)d\mathbf{x}' \,;\, \mathbf{x}' \in \upsilon \qquad \text{Equation 2.56}$$

Applying this filter to the Navier-Stokes equations of Table 2.6, results in the filtered equations in Table 2.8 [22]. The viscous stress tensor, τ_{ij}, is defined as previously and the subgrid-scale stress tensor, τ_{ij}^{sg}, is analogous to a Reynolds stress tensor and its anisotropic portion is modeled using the turbulent viscosity hypothesis as done in the k-ε model [42]. Additionally, subgrid-scale turbulent transport of scalars is treated with the gradient diffusion hypothesis as seen previously in equation 2.48. It should be noted that unlike the density averaged mean quantities, the filtered quantities are random variables.

Table 2.8: LES Filtered Navier-Stokes Equations

Equation Name	Equation
Continuity	$\frac{\partial \rho}{\partial t} + \frac{\partial}{\partial x_j}\left(\rho \overline{u}_j\right) = 0$
Momentum	$\frac{\partial}{\partial t}\left(\rho \overline{u}_i\right) + \frac{\partial}{\partial x_j}\left(\rho \overline{u}_i \overline{u}_j\right) = -\frac{\partial \overline{p}}{\partial x_i} + \frac{\partial}{\partial x_j}\left(\tau_{ij} - \tau_{ij}^{sg}\right) + g_i \,;$ $\tau_{ij} \equiv \mu\left(\frac{\partial \overline{u}_i}{\partial x_j} + \frac{\partial \overline{u}_j}{\partial x_i}\right) - \frac{2}{3}\mu \frac{\partial \overline{u}_k}{\partial x_k}\delta_{ij} \,;$ $\tau_{ij}^{sg} \equiv \rho\overline{u_i u_j} - \rho \overline{u}_i \overline{u}_j$

In order to model the turbulent viscosity without k and ε transport equations, the Smagorinsky-Lilly model uses equation 2.57. Where L_s is the mixing length at subgrid scales, defined as in equation 2.58, where κ is the von Kármán constant, d is the distance to a wall, and $C_s = 0.17$ [42, 22].

$$\nu_T = L_S^2 \sqrt{2\bar{S}_{ij}\bar{S}_{ij}} \qquad \text{Equation 2.57}$$

$$L_s = \min(\kappa d, C_s V^{1/3}) \qquad \text{Equation 2.58}$$

2.4.4 Turbulence-Chemistry Interaction

Within the proximity of the flame sheet many simultaneous phenomena and feedback mechanisms occur at a wide range of spatial and temporal scales, thus presenting a unique challenge to the engineer. As discussed previously, buoyant isothermal non-reacting plumes have a complex flow field to simulate, consisting of high baroclinic torques, periodic vortex shedding, and a strong dilatational field. The addition of hot reactive species at opposite ends of this density front; undergoing highly exothermic reactions, pyrolysis, and recombination, yields large thermal and species gradients. Despite the common notion that combustion is a mature academic field, it is not surprising that turbulent combustion continues to confound and challenge engineers.

To capture fluctuations in the flow field, the mixture fraction approach is typically applied with an assumed shape probability density function (PDF) approach. The PDF provides the probability of the fluid parcel having the mixture fraction in the vicinity of Z [22]. Inherent in the use of the source-less transport equation is the assumption of chemical equilibrium, thus use of a PDF is appropriate, especially for steady-state simulations. Additionally, avoiding decomposition of Z also avoids the need of using a generalized gradient hypothesis, as seen in prior turbulent scalar transport models, that is amenable to a wide range of fuels.

The assumed shape PDF used by many commercial codes is the β-distribution seen in equation 2.59, which is like the normal distribution in that it may be defined by is mean and variance, $\overline{Z}$ and $\overline{Z'}$ respectively.

$$p(Z) = \frac{Z^{\alpha-1}(1-Z)^{\beta-1}}{\int Z^{\alpha-1}(1-Z)^{\beta-1}\,df}; \alpha = \overline{Z}\left(\frac{\overline{Z}(1-\overline{Z})}{\overline{Z'^2}} - 1\right); \beta = (1-\overline{Z})\left(\frac{\overline{Z}(1-\overline{Z})}{\overline{Z'^2}} - 1\right)$$

Equation 2.59

The temperature, species mass fractions, and density are assumed to be dependent on the mixture fraction, thus the local PDF shape. The dependence of these parameters on local mean enthalpy changes, due to radiation or near wall effects, must also be taken into account. Many codes employ a clever technique of creating a so called "look-up table" of these parameters as functions of the mean and variance of Z for several scaled heat flux scenarios in conjunction with an equilibrium chemistry solver. A block diagram of this scheme is seen in Figure 2.17 [22].

Figure 2.17: Schematic of Look-up Table Creation [22]

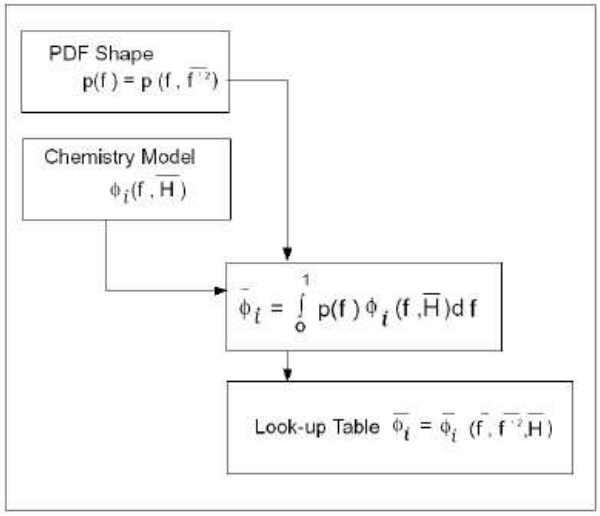

The mean and variance of Z are independently modeled in transport equations and this table is accessed during the simulation to provide the mean scalar values, at considerable computational savings over direct calculation [34]. The transport equation empirical constants are defined as follows: Pr_T = 0.85, C_g = 2.86, and C_d = 2.0. While the physical meaning of most of the terms are familiar by now, the last two terms of equation 2.61 which are not familiar are the viscous scalar dissipation and the turbulent transport of the variance

of Z respectively, for which ε/k represents the turbulent mixing time scale. The interaction between the flamelet concept and local turbulence is to be discussed in the modeling section of this study.

$$\frac{\partial}{\partial t}\left(\overline{\rho}\overline{Z}\right)+\frac{\partial}{\partial x_j}\left(\overline{\rho}\widetilde{u}_j\overline{Z}\right)=\frac{\partial}{\partial x_j}\left(\frac{\mu_T}{\mathrm{Pr}_T}\frac{\partial\overline{Z}}{\partial x_j}\right) \qquad \text{Equation 2.60}$$

$$\frac{\partial}{\partial t}\left(\overline{\rho}\overline{Z'^2}\right)+\frac{\partial}{\partial x_j}\left(\overline{\rho}\widetilde{u}_i\overline{Z'^2}\right)=\frac{\partial}{\partial x_j}\left(\frac{\mu_T}{\mathrm{Pr}_T}\frac{\partial\overline{Z'^2}}{\partial x_j}\right)+C_g\mu_T\left(\frac{\partial\overline{Z'^2}}{\partial x_i}\right)^2-C_d\overline{\rho}\frac{\varepsilon}{k}\overline{Z'^2} \qquad \text{Equation 2.61}$$

Use of species transport and finite-rate chemistry does not allow for such a PDF method, especially that the purpose of using such an approach to chemistry is to avoid the assumption of chemical equilibrium. As with the 'fast chemistry' assumption leading towards the mixture fraction model, the mixing time scales are recognized to limiting in turbulent flames dynamics. Magnussen and Hjertager, coupled with previously mentioned work on soot formation, postulated the eddy-dissipation model where reaction rate kinetics are on the order of the eddy mixing time scale, k/ε [37]. This reaction rate of specie α is outlined in equation 2.62, with empirical constants replaced by their numerical values. When mixing limited, the presence of turbulence, k/ε > 0, initiates reaction rather than an activation energy, i.e. ignition, source. When modeled with LES, where k and ε are not modeled in transport equations, the turbulence mixing rate is determined as the subgrid scale mixing rate in equation 2.63 [22]. This method is known to poorly handle radical species due to the reliance on mixing time scales, however as noted previously, the global mechanisms to be used in Table 2.5 contain only stable species.

$$R_{\alpha,1}=\nu'_{\alpha,1}M_\alpha(4.0)\rho\frac{\varepsilon}{k}\min\left(\frac{X_R}{\nu'_{R,1}M_R},0.5\frac{\sum_P X_P}{\sum_j^N \nu''_{j,1}M_j}\right) \qquad \text{Equation 2.62}$$

$$\tau_{mix}^{sgs}=\frac{\nu_T}{L_S^2}=\sqrt{2\overline{S}_{ij}\overline{S}_{ij}} \qquad \text{Equation 2.63}$$

2.5 Final Remarks

It is apparent that fixed bed wood combustion theory and current modeling techniques are as chaotic and disparate as the phenomenon itself. To reiterate, the goal of this study is to reduce PM and CO emissions of the Model 100 OWHH while simultaneously improving its efficiency, with the aid of the modeling techniques outlined in this chapter and a commercial CFD package.

Not until recently have a few studies been performed on the application of CFD to OWHHs or fireplaces. Additionally, over the course of this study a wealth of laboratory testing was performed as part of the Model 100's iterative redesign. Thus in addition to emissions reductions, this study will also compare the merits of the varied approaches to fuel characterization, flow field simulation, and turbulent combustion modeling of OWHHs.

Chapter III: Data Acquisition

Prior to embarking of CFD modeling of the OWHH, it is useful to discuss the operation of the Model 100 and how test data is acquired through the EPA Method 28. Modeling assumptions are not solely to be based upon previously discussed theory and practice, but also on observed phenomena and the typical operation of the OWHH. In the pursuit of emissions reductions and efficiency gains, the iterative process of design and operation modification is inherently specific to the Model 100.

3.1 The Model 100 OWHH

As evident by its discussion, an OWHH is a simple device that transfers the heat via wood (or other biomass) combustion to water for domestic or commercial use. The operation of the Model 100, as shown in Figure 3.1[3], reflects this simplicity. Burning wood (cordwood in this case) within the refractory brick firebox releases hot exhaust upwards, due to buoyancy. The rising exhaust creates a vacuum drawing in air through inlet ports at point B, driving the pyrolysis and eventual combustion. The exhaust gases travel upwards from the burn to pass through and along pipes containing a heat transfer fluid, generally water sometimes with propylene glycol added. This fluid runs through a pump-driven loop which is oriented in counter-flow such that the temperature gradient between the exterior exhaust gases and the internal fluid is minimized. The hot fluid runs through a secondary heat exchanger at point E, which heats the water for end use. To prevent the boiling within the internal loop, a damper plate covers the air inlet ports to meter the burn and reduce internal temperatures. To prevent losses through the skin of the unit, several layers of insulation line the interior of the Model 100.

[3] http://www.greenwoodfurnace.com/How_it_Works.htm

Figure 3.1: Overall Schematic of Model 100 Operation

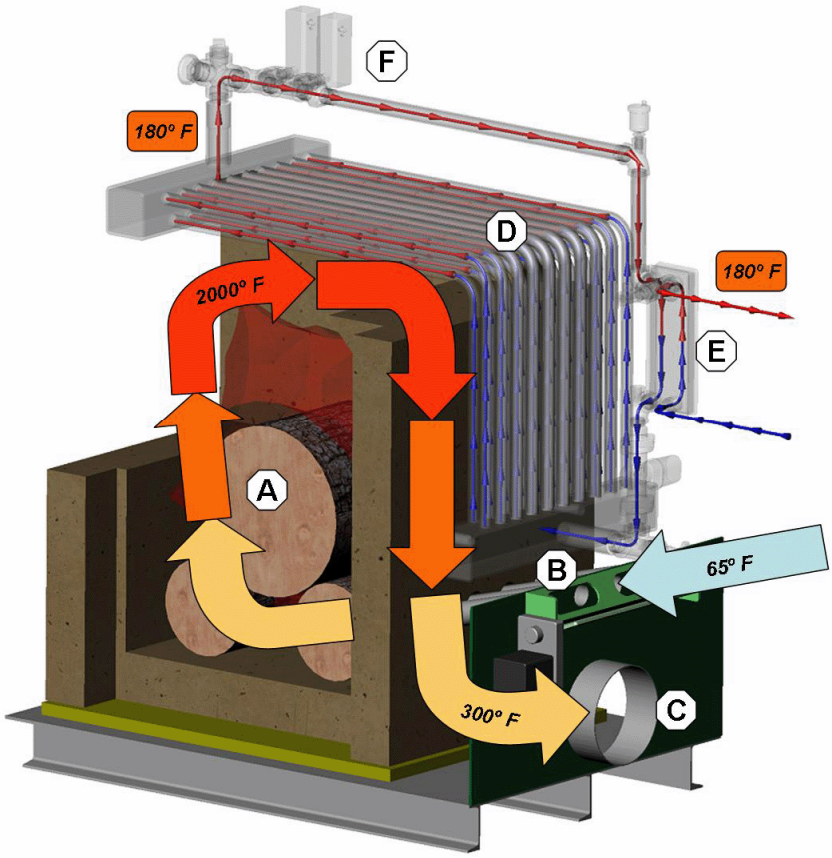

Potential issues in the overall design, with respect to emissions reductions and efficiency are apparent upon first glance. First, the placement of firebox air is fundamentally tied to flame dynamics, especially due to the natural draft design. It may be inferred that the air inlet and exhaust side being on opposing sides of the wood load will be problematic in the even distribution of oxygen during gas phase reactions. Second, the primary combustion region within the firebox is voluminous to allow large fuel loads. While advantageous to the user, gas phase pyrolysis in the pre-combustion zone favors the reverse recombination reaction of equation 2.8 in larger volumes and especially in fuel rich conditions. This may result in the escape of unburned organic carbonaceous species. Third, the post-combustion zone in this design, vital to CO and PM oxidation, is rather small. We expect that this zone ends when the gases reach the heat extraction tubes since temperatures will drop enough to effectively freeze any further reactions.

The firebox enclosure composed of refractory brick is an important aspect of this design. The refractory is an excellent thermal insulator and re-radiator; keeping flame temperatures high and promptly igniting fuel loads with a high thermal inertia, thus over long periods. The brick itself is a proprietary mix alumina, silica, and other materials with the following properties at typical firebox conditions: C_p = 960 J/kg K, ϱ = 1,856 kg/m^3, and k = 0.66 W/m K. The EPA Test Method 28 is performed with a preheated OWHH, thus the initial heating of this refractory is to be ignored during this study.

3.2 Testing Methods

As part of the mandate to assess the criteria pollutant and other emissions from stationary sources under the U.S. Clean Air Act and its amendments, the EPA has established a series of standardized and easily repeatable test methods. While the intent is to conservatively measure emissions which would occur during normal operation, the Method 28 requires the use of a test crib as seen in Figure 2.8 rather than cordwood, thus the test procedure has its critics[4]. While the intent of this study is to achieve the emissions limits set by the EPA and NESCAUM with test cribs, the performance of the unit with cordwood is of possibly greater importance as this is the way most owners will use the unit. Additionally, in spite of the small weighting that the category 4 testing scenario of Table 1.1 is given, it is the focus of CFD simulations. During the category 4 burn at full output, the damper plate is generally not activated and the flow field, pyrolysis, and flame dynamics are closer to steady state behavior. During the categories 1, 2, and 3 burns of lower outputs, the air inlet port damper plate is activated several times causing fluctuations in the already chaotic behavior of the burn, thus posing challenges in isolating the causes of emissions and assessing their mitigation. Therefore, the majority of this study focuses on the category 4 test crib burn.

[4] Letter from Myren Consulting to EPA, 10/7/2006

3.2.1 EPA Method 28

While certified EPA tests are executed by third parties to prevent conflicts of interest, including those from which data are used in this study, it is useful to discuss the test methods in some detail with respect to fuel requirements and PM sampling.

Per the Method 28 requirements, the test crib is comprised of 4" x 4" pieces of White Oak, with 19-25% moisture on a dry basis, that are to be 80% of the longest firebox dimension in length, which is roughly 20". The wood moisture is determined by a handheld electric resistance moisture meter as an average of at least three points, 3 inches from each of the ends and at the center parallel to the grain. The amount of crib pieces is determined by the firebox volume, the total test crib weight should be 10 lbs/ft^3 of firebox space. For the Model 100, this comes to roughly 60 lbs, which is about 7 pieces. The crib pieces are held together by 3/4" spacers. A photo of a typical test crib is shown in Figure 3.2. The reasoning behind the use of cribs rather than cut cordwood is the repeatability of this test crib. Any irregularities due to geometry, size, and bark are eliminated. However, increasing the surface area to volume ratio of the wood has marked effects on pyrolysis and thus PM formation rates.

Figure 3.2: Typical Method 28 Test Crib

The PM emission rate is determined by a sampling train which draws from a dilution tunnel. In order to prevent the development of excessive back pressure in the exhaust as a result of the lengthened path., the exhaust terminates at a typical height and a hood resides just above the exhaust exit drawing flow into the sampling region. Additionally, the use of the hood draws in ambient air to reduce stack gas sampling temperatures and freeze any PM oxidation or morphological changes, hence the name dilution tunnel.

The PM is sampled in accordance with Method 5G: *Determination of Particulate Matter Emissions from Wood Heaters (Dilution Tunnel Sampling Location)* [54]. The typical PM sampling train is seen in Figure 3.3. Two glass fiber filters, with no less than 99.95% catch efficiency, are used in series in the event of breakthrough to prevent PM reaching the dry gas meter. Secondary and tertiary sampling trains are setup prior to testing to be used in the event of the complete loading of the filters, which is monitored by the filter pressure drop. Additionally, dual sampling trains are operated simultaneously during the test to assure accuracy. The filtration precedes the gas drying in order to catch condensable PM, for which the organic PM is largely comprised of. Upon completion of the burn, the filters are removed, dried with the aid of a desiccator, and weighed. To account for bias from a dusty testing facility, the sampling equipment is washed thoroughly prior to testing and afterwards with acetone. The acetone used for post-test cleaning is collected, dried, and weighed in a similar manner as the particulate filters. This 'acetone blank' will ultimately be subtracted from the calculated PM emissions [54].

Figure 3.3: Typical Method 5G Particulate Sampling Train

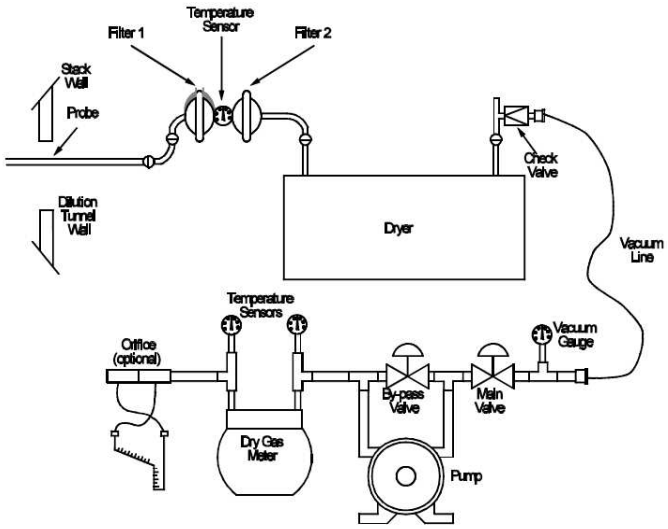

The entire PM stream is not routed to these sample filters and also the probe influences the flow field within the tunnel. To rectify these problems, the sample is taken representatively and isokinetically. To reduce non-uniformities in the particulate concentration stream, the sample is taken eight stack diameters downstream and two upstream from any bend or other disturbance in the flow. Additionally, the sampling point traversing the stack is chosen to have the average tunnel velocity. Isokinetic sampling is vital when sampling the particulate-laden tunnel gas, especially for organic PM which contains varied shapes and a wide size distribution. The principle of isokinetic sampling is to draw the sample, via a vacuum pump in this case, at a face velocity equal to that of the mean tunnel flow to minimize streamline distortion. If the sample is drawn faster than the tunnel flow the PM sample weight is underestimated, as normally diverted streamlines at the exterior of the probe are drawn in and the pathlines of larger particles, with enough momentum, divert to the outside of the probe. If the sample is drawn slower than the tunnel flow the PM sample weight is overestimated, as the streamlines that are normally drawn in backup and go around the probe face, drawing smaller particles but the pathlines of larger particles continue into the probe. Without isokinetic sampling, the PM sample is biased either to only the smaller or larger particles within the tunnel PM size distribution. Variation from isokinetic sampling rate must no greater than 10% [13].

The weight of the dried PM filter catch is divided by the dry gas volume creating an average PM concentration, which is multiplied by the tunnel flow rate to derive a total PM emissions rate. The mean tunnel flow rate is determined via an S-type pitot tube attached to the sampling probe. Along with the dry burn rate and assumed wood Higher Heating Value (HHV) of 8,550 Btu/lb, the PM emissions per MMBtu input may be determined. Additional data taken during this testing are: the weight change of the furnace in lbs (± 1.0 lb), the stack temperature and static pressure, the inlet (cold) and outlet (hot) temperatures of the internal heat transfer loop, and the flow rate of the heat transfer fluid.

3.2.2 Experimental Data Acquisition

In the determination of the stoichiometry of the burn and the efficiency of the OWHH, additional data are taken during Method 28 testing beyond that required and during research and development (R&D) testing as well. A number of internal and external temperatures are measured throughout the Model 100 via standard thermocouples. Throughout this study, the temperatures reported will be referenced by their location. The Model 100 schematic in Figure 3.4 is provided as reference for these internal locations. During testing, internal thermocouples are typically doubled up at each location with respect to the z-direction and averaged. The 'Baffle' temperature zones reflect a later design of the furnace but will reside in these locations. The exterior temperatures are defined with respect to the door side of the OWHH.

Figure 3.4: Labels of Thermocouple Locations

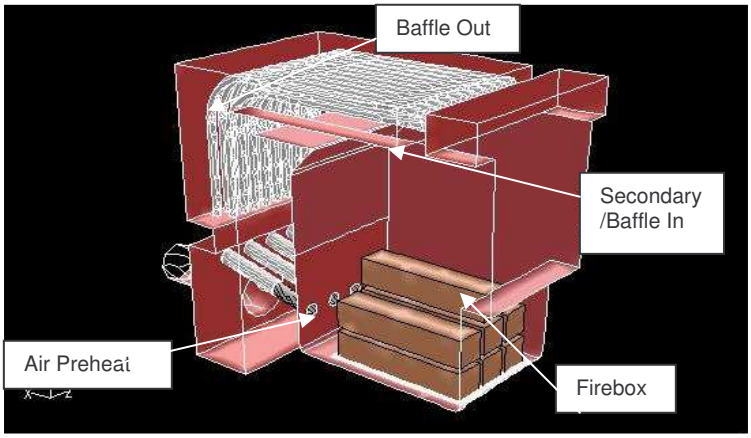

Beyond the requirements of pressure measurement for Method 28, magnehelic gauges were used to measure the static pressure at the initial exhaust exit. Later uncertified testing employed the use of an orifice meter to determine the inlet forced air flow rate to the total unit, and to the firebox and secondary air injection separately. As the fans operated at steady state during the test, Bernoulli's Principle allows for the following approximation from the 6" duct through the 3" orifice to be made. Use of an orifice meter requires a long intake to assure fully developed flow at the orifice, this can be seen in a photo in Figure 3.5. Also notice in the photo that the unit sits completely on a scale. This scale with a resolution of ± 1 lb, along with the test duration, is what may be used to determine the burn rate.

$$\dot{V} = A_{duct}\left(1-\left(\frac{D_{duct}}{D_{orif}}\right)^4\right)^{-1/2}\left(2\frac{\Delta P}{\rho}\right)^{1/2} \qquad \text{Equation 3.1}$$

Figure 3.5: Test Facility Photo Highlighting Orifice Meter

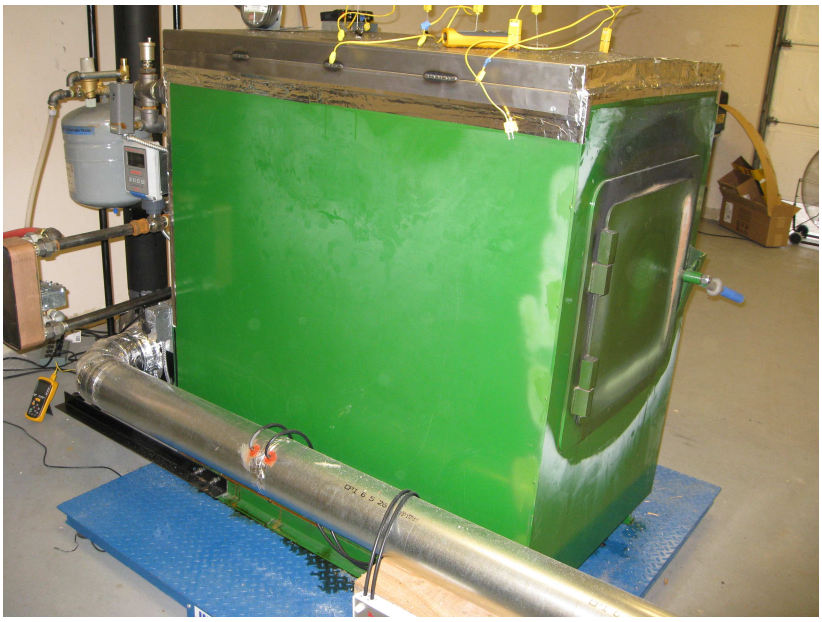

Also, the CO_2, CO, and O_2 dry gas concentrations are measured in varying combinations during this study. The CO and CO_2 when measured are done so with an infrared analyzer and O_2 with a paramagnetic analyzer. As the gas analysis industry has a

majority of its business with well tuned natural gas boilers emitting high CO_2, low O_2, and trace CO and other species; the analysis equipment will measure two out of the three species, assume they contain all of the elemental oxygen, and arithmetically determine the concentration of the third specie. This assumption will be tested throughout this study and may prove to be inappropriate.

3.3 Discussion of Testing

As mentioned previously, a wealth of testing has been performed on the Model 100 and its modified iterations. Over the course of this study, 8 certified and 18 uncertified cribwood tests and 4 certified and 4 uncertified cordwood tests have been performed. As some of the testing was performed in conjunction with recommendations from this study, a chronological report would be logical. The remainder of this study will be segmented into three sections: initial creation of baseline analysis and modeling results, assessing overall oxygen starvation, and the implementation of physical modifications. These sections will chronologically follow the evolution of this study. The following two paragraphs provide the framework of the entire study.

The analysis of the initial test results indicated that the Model 100 is oxygen starved and runs fuel rich for a majority of the burn. Forced air injection effectively brought the Model 100 to fuel lean conditions and reduced PM emissions during the cordwood tests, however the pyrolysis rate increased dramatically during the cribwood test, causing increased PM and CO emissions. The heating rate of this cribwood test increased, however the much shorter burn led to a marked drop in efficiency. Under lean conditions, complete combustion was now mixing limited. As with many research endeavors, solving one problem generally identifies, or creates, another problem.

The proverbial low hanging fruit was picked and now any further gains in emissions reduction and efficiency required physical modifications. A more compact manner of heat transfer was proposed, with an added benefit of greatly increasing the size of the post-combustion zone. This space allowed for the addition of various flow restrictions to aid mixing and the introduction of secondary air. Several permutations of various baffle arrangements, secondary air injection, and primary air restrictions were assessed and

significant reductions in PM and CO emissions were achieved. Efficiency gains were also made, however the test OWHH required blower fans, thus eliminating the simplicity of a natural draft unit. Certified testing of the operationally and physically modified furnace met the EPA Phase I Emissions Level and earned the Model 100 a "Green Label".

3.3.1 Potential Testing Sources of Error

Laboratory testing, especially that which is required to satisfy legal mandates, should always be performed with the most reasonable reduction in sampling error. The quantity measured, its temporal resolution, its method of measurement, and the potential source of error are outlined in Table 3.1 for certified and uncertified tests. While these listed sources of error and that introduced by the temporal resolution are not insignificant, it is beyond the scope of this study, its available resources, and beyond the demand of the resolution required for simulation to seek more accurate methods of measurement.

Table 3.1: Summary of Measurement Methods

Measured Quantity	Temporal Resolution (minutes)		Measurement Technique	Potential Source of Error
	Uncertified	Certified		
OWHH Weight Loss (Burn rate)	5	5	Digital Scale	Resolution is to nearest lb
Temperature	5	1	K-type Thermocouple	Spatial resolution
Pressure	5	5	Magnehelic Gauge & Inclined Manometer	Visual reading during fluctuations
Dry Gas Concentration: CO_2, CO, O_2	1	1	Infrared and Paramagnetic Analyzer	Assumed concentration of remaining specie
Fluid Flow Rate	5	5	FloCat	Visual reading during fluctuations
Particulate Weight	N/A	Full test	Method 5G Sampling Train	Ensuring representative and isokinetic sampling
Stack Opacity	5	N/A	Visually	Subjective in nature

Chapter IV: Benchmark Modeling and Analysis

While modern CFD codes are powerful tools for understanding an experiment, they still involve many approximations. This is especially true for the present problem (i.e., a buoyantly-driven reacting flow). A prudent approach is to test the model against benchmark data before attempting to use the code to suggest physical or operational changes to the furnace. Good reproduction of the furnace processes gives some evidence that the code can be used to "test" proposed changes. Thus, this section will begin with discussing initial test data, perform initial analyses, and finally benchmark a 2D and 3D CFD model using different methods discussed previously.

4.1 Benchmark Testing

Prior to this study, tests performed on the Model 100 consisted of certified EPA Test Method 28 source tests with Douglas Fir cordwood and White Oak cribwood. These tests were performed solely to determine compliance with the 0.6 lbs PM/MMBtu limit and often quantities of interest such as skin temperatures, various internal temperatures, and gas flow rates were not measured. Due to limited data reported in initial cordwood testing and as mentioned in Chapter 3, the category 4 test crib burn is to be the focus of this study, the benchmark modeling will focus on a category 4 cribwood test on July 10th, 2007.

4.1.1 Initial Test Results

The source test was performed at Myren Consulting test facility in Colville, WA. A 65.25 lb test crib of 17.62% moisture (wet basis) was burned in a preheated Model 100 for 150 minutes. Internal temperatures were measured at the Firebox and Secondary locations outlined in Figure 3.3 and external temperatures were measured on all exposed sides of the OWHH. To assess the heat output of the OWHH to the internal fluid loop, the hot and cold manifold temperatures of the fluid are reported as well. The temperatures recorded during the test are shown in Figures 4.1 and 4.2. The three sudden dips in internal

temperatures are times where the air inlet damper was activated to prevent boiling within the loop. This was due to an ambient temperature that reached a peak of 94°F during testing.

Figure 4.1: Firebox, Secondary, and Stack Temperatures of Initial Crib Test

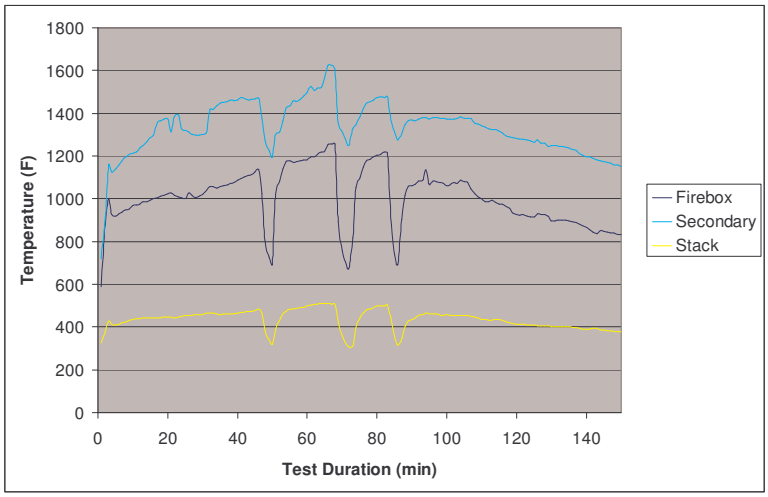

Figure 4.2: Skin and Loop Temperatures of Initial Crib Test

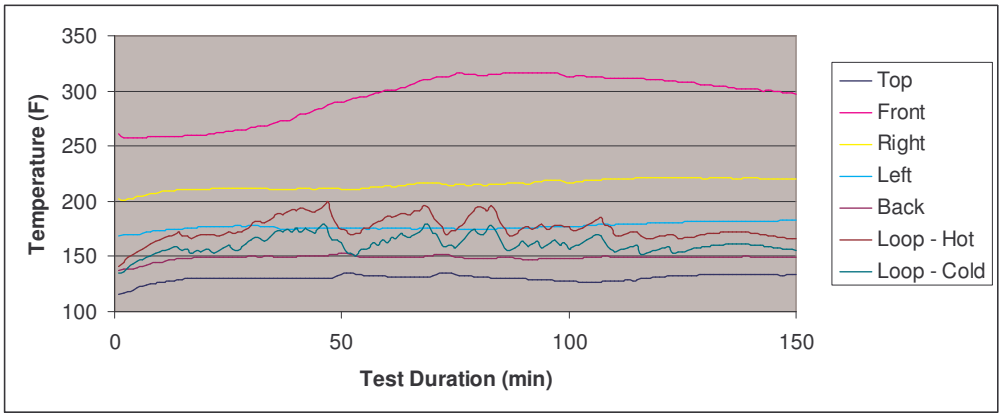

To determine the system stoichiometry and burn rate, the measured CO_2 and CO dry gas stack concentrations and the scale reading which indicates the burn rate are shown in Figures 4.3 and 4.4 respectively. While often enough to characterize the exhaust flow constituents, O_2 is also measured however this is to be reported later as. The reader is reminded of the distinct burn rate seen in Figure 2.12, for which the char oxidation stage may be assumed to begin dominating the burn somewhere between the 60^{th} and 80^{th} minute. Additionally, as the test begins once the test crib is loaded, several minutes elapse for the

wood surface to reach the drying and pyrolysis temperature and for solid phase pyrolysis to begin. The estimate of 6 minutes from Section 2.1.3.2 is not far off.

Figure 4.3: Dry Gas Mole Fractions of CO_2 and CO of Initial Crib Test

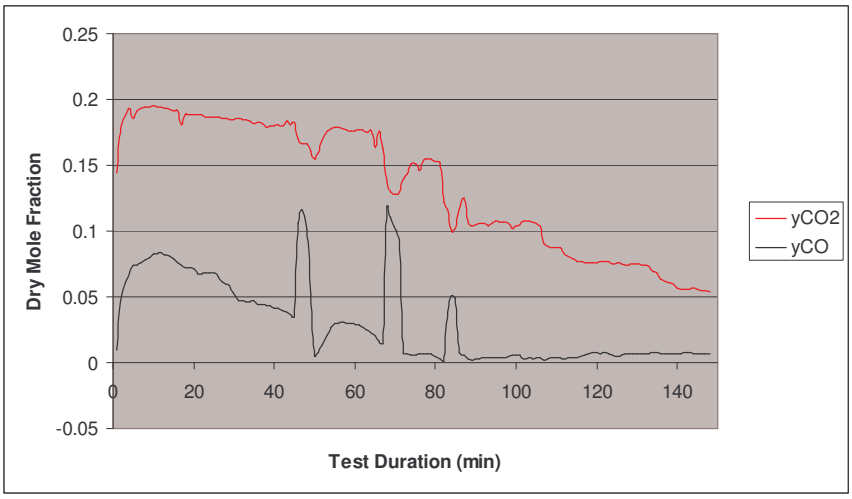

Figure 4.4: Scale Reading of the Initial Crib Test

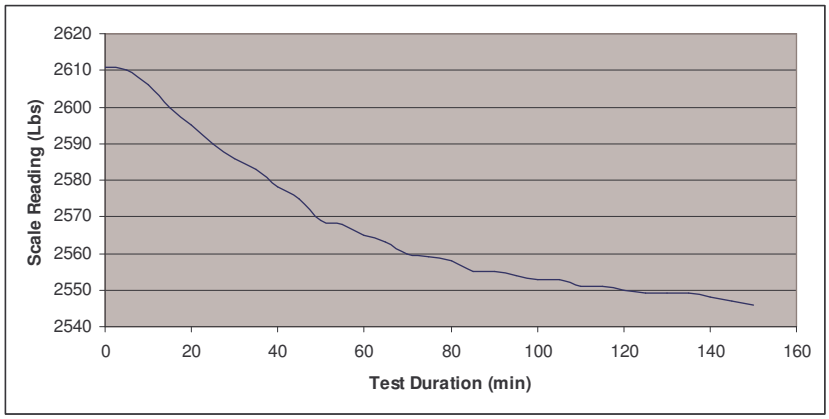

The resulting unadjusted PM emissions were 0.62 lb/MMBtu input, which when weighted with the PM emissions of lower categories, which have been observed to be up to 290% higher, would result in cumulative PM emissions well beyond the 0.6 lb PM/MMBtu. To understand the emissions rate throughout the burn, five separate filters were used at points throughout the burn.

4.2 Data Analysis

Due to the buoyancy driven flow field and the complexity of wood combustion, many details of the chemistry and internal heat transfer are not as simple to acquire as in more canonical flows, such as methane-air jet diffusion flames. Such simple quantities as the mass of air entering the system must be approximated. Numerous approximations must be made to establish internal boundary conditions for the CFD simulation and a comparative basis for its results. From the test data, three aspects of the OWHH operation may be analyzed: the system stoichiometry and thus the mass air-to-fuel ratio, the total energy budget of the OWHH, and the anticipated internal oxidation rates of PM and CO.

4.2.1 System Stoichiometry and Air-to-Fuel Ratio

As discussed in Section 2.1.3.3, the wood combustion community still disagrees on how to chemically approximate the gas phase pyrolysis species, which presents a challenge in selecting a surrogate fuel to determine the product species and the air-to-fuel ratio. Rather than assess each individual stage of combustion and the fuel species involved, the ultimate analysis of White Oak, from Table 2.1, is used. This "wood molecule" will also consist of a liquid water fraction representing the moisture content, which is at constant proportion throughout the burn. Naturally this is an inappropriate assumption. The majority of the PM emissions are, however, generated prior to the char oxidation stage, and during this period the assumption of proportional water fraction is good. The product species are to be limited to CO, CO_2, H_2O, O_2, and N_2. Unburned fuel and PM are important from an environmental point of view, but these are trace species that do not significantly influence stoichiometry or energy release, and thus they can be ignored in the present calculation without significant error.

With abovementioned assumptions and the analysis for the general "wood molecule" in Appendix A, the following may be derived from the measured dry gas concentrations of CO and CO_2: stoichiometric coefficients from equation A.2, the ratio φ which is defined as in equation 4.1 and A.5, and the ratio Θ which is defined in equation A.2. Rather than compare actual to ideal ratios of air to fuel without CO conditions, Θ indicates the amount

of air needed to completely consume the fuel and produce the measured CO_2 and CO concentrations. CO is measured in the stack throughout the test, as seen in Figure 4.3, thus $\Theta < \varphi$. The calculated φ during the test is shown in Figure 4.5, indicating a fuel rich burn for the first 45 minutes. This coincides with the maximum observed PM emissions rate on a g/kg basis, which is shown for the five separate sampling periods, for which the correlation is apparent. The minimum values of φ and the mass air-to-fuel ratio calculated for the fuel rich portion of the burn are 0.724 and 4.168 respectively.

$$\varphi \equiv \frac{\left(n_{air} / n_{fuel} \right)_{actual}}{\left(n_{air} / n_{fuel} \right)_{stoichiometric}} \qquad \text{Equation 4.1}$$

Figure 4.5: Phi and Measured PM Emissions Rate of Initial Crib Test

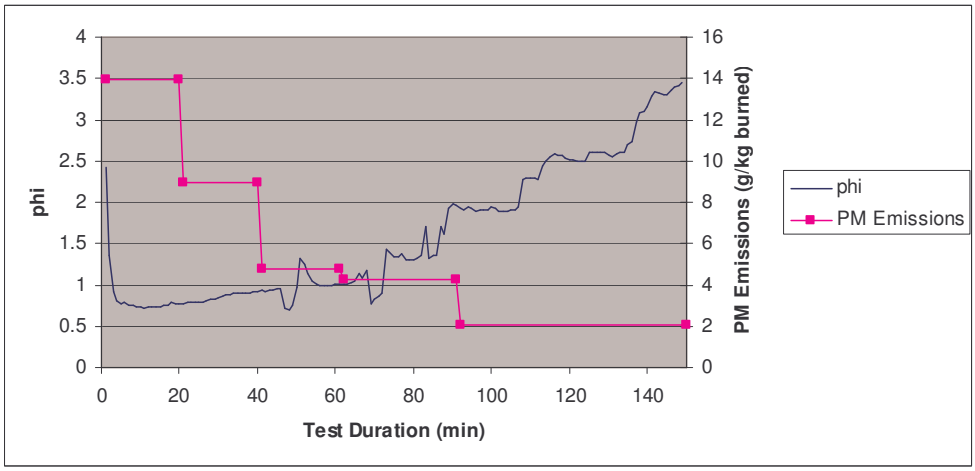

The measured CO and CO_2 dry gas exhaust mole fractions are all that is needed to calculate the stoichiometry. The O_2 measurement is thus redundant, and this can be used as a check of the overall stoichiometry calculation. The comparison between measured and calculated exhaust dry O_2 mole fractions is shown in Figure 4.6. As the first 30 minutes of this test is oxygen starved, the negative concentrations calculated are due to the inadequacy of the complete combustion model under fuel rich conditions. In other words, neglecting the fuel species in the exhaust is inappropriate under rich conditions. While good agreement

is shown for the fuel lean char oxidation dominated portion of the burn, during the fuel rich gas phase pyrolysis dominated portion, that the presence of O_2 in the exhaust is an indication of inadequate mixing rather than O_2 limited combustion. As the simplified one-step reaction model of Appendix A does not account for mixing limited reactions and further analysis requires an assumption of equilibrium chemistry, the limited exhaust species approach is to be maintained despite this shortcoming.

Figure 4.6: Calculated vs. Measured O_2 Stack Concentrations for Initial Crib Test

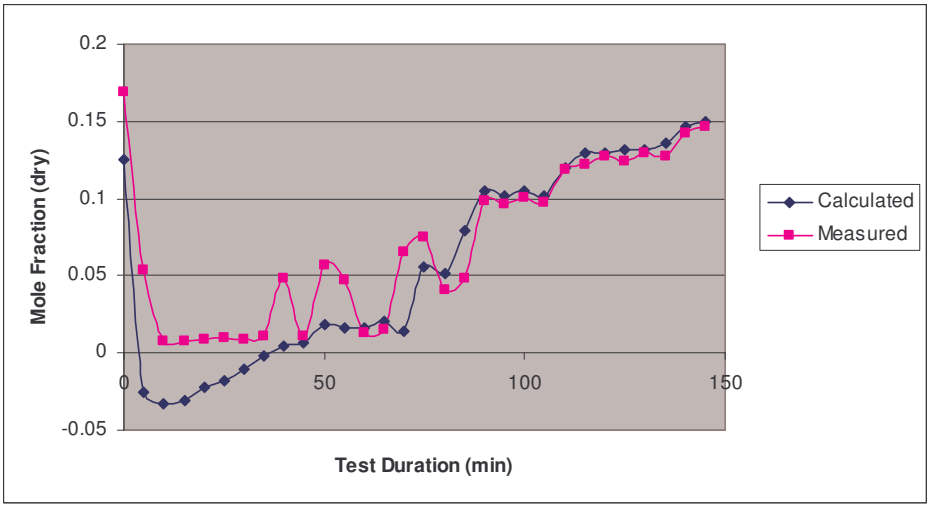

4.2.2 Energy Budget of the Model 100

The primary purpose of the OWHH is not to burn wood but provide hot water, and reductions in PM emissions should not come at a cost of performance. That said, an analysis of the system's energy budget is needed. Additionally, this analysis is needed in order to determine realistic internal temperature and/or heat flux boundary conditions for the CFD simulation.

The only measured heat transfer rate, that to the internal fluid loop, is calculated from the hot and cold sides of the internal loop and the fluid volumetric flow rate, denoted as $\dot{Q}_{loop}$ per equation B.25. Independently, using the method outlined in Appendix B.1, the heat transfer rate to the internal fluid loop can be calculated from measured quantities. To calculate the heat transfer rate from the exhaust gases to the internal fluid loop,

approximations of the flow path must be performed in order to apply empirical convective heat transfer relations. These approximations include: the idealization of the heat transfer regime into two discrete cross and parallel flow zones without a transitional region, the assumption of unidirectional far field averaged velocities without circulation or non-fully developed near wall effects, and the treatment of each zone as constant temperature environments. If the calculated and measured heat transfer rates show good agreement, then such quantities as the tube bank surface temperature and tube bank heat transfer coefficients may be approximated.

Using the measured internal temperatures of Figures 4.1 and 4.2 and the composition of the exhaust calculated previously, the heat transfer rate to the internal loop is calculated per Appendix B.1, as the sum of the cross-flow and parallel-flow heat transfer regimes, $\dot{Q}_{cross}$ and $\dot{Q}_{par}$ respectively. This assumes that the chemistry freezes upon heat extraction, that is the exhaust dry mole fractions calculated do not change from the tube bank to the stack. Figure 4.7 illustrates the comparison of the calculated and measured heat transfer rates, reported in BTU/hr. Good agreement is shown between the calculated and measured heat transfer rates, considering the resolution of the measured temperatures and the expected accuracy with these types of heat transfer calculations.

Figure 4.7: Calculated and Measured Heat Transfer to Internal Fluid Loop

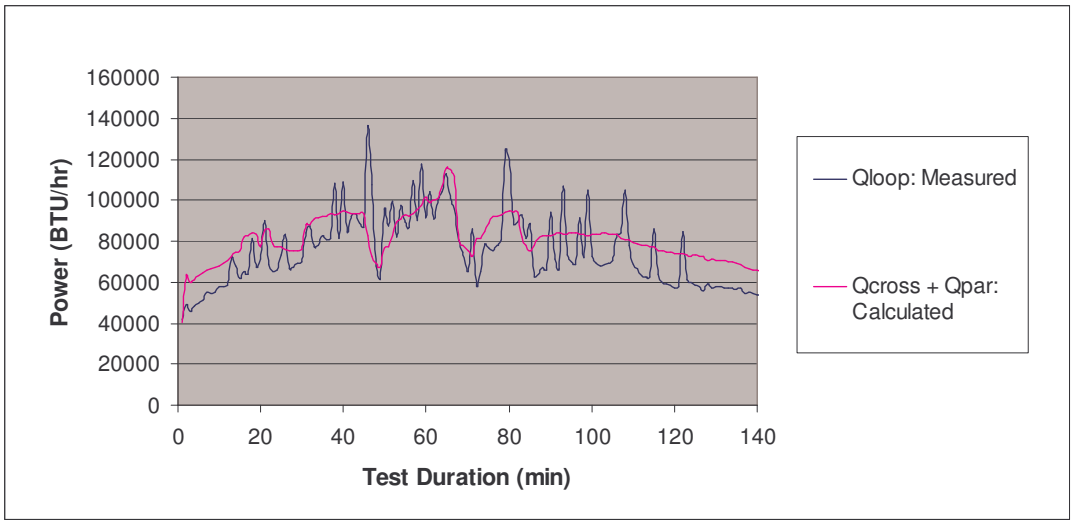

With the exception of large measured spikes due to the activation of the air inlet damper, the calculated heat transfer rate slightly overestimates the measured data, for which it should be noted that convective heat transfer calculations have typical accuracies of ±20%. The simplicity of the analysis and good agreement with measured quantities will make its use acceptable.

From this analysis, internal boundary conditions may be estimated and the design of the system may be critiqued. Using the first 15 minutes of the burn for time averaged quantities for peak pyrolysis simulations, where the majority of PM emissions occur per Figure 4.5, the surface temperature of the tube bank is estimated as 450 K. The splitting of the flow regime into cross flow and parallel flow zones allows for comparison between their efficiencies. Perhaps obvious to the student of convective heat transfer, cross flow external convective heat transfer is more efficient than parallel flow. This is validated in Figure 4.8, which compares the total convective heat flux of the cross and parallel flow regimes. It should be noted that the cross flow portion of the tube bank is 32.7% of its total surface area. An entirely cross flow tube bank would provide the same required heat transfer at a greatly reduced surface area, thus reducing material costs and OWHH weight.

Figure 4.8: Total Convective Heat Flux of Each Regime

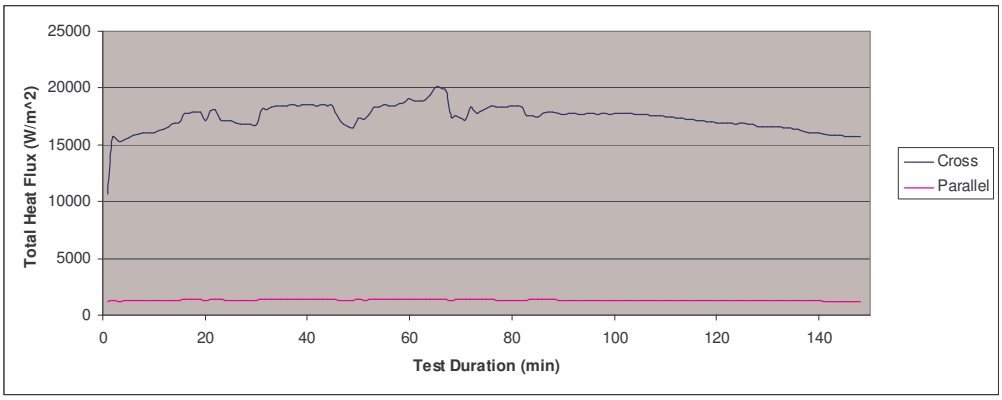

Performing a so called 'First Law' energy budget of the OWHH requires the determination of the expected heat flows, sources, and sinks. A cartoon of the OWHH shown in Figure 4.9 illustrates the mass flows (solid arrows), losses (squiggly lines), and sources/sinks (internal text). Succinctly, this energy budget is shown in equation 4.2.

Figure 4.9: Cartoon of the OWHH Energy Budget

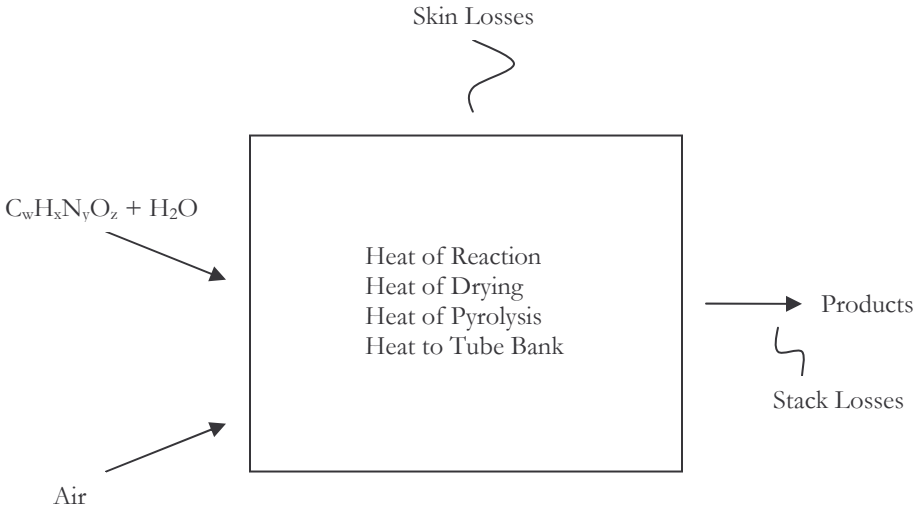

$$\dot{Q}_{rxn} = \dot{Q}_{stack} + \dot{Q}_{skin} + \dot{Q}_{dry} + \dot{Q}_{pyr} + \dot{Q}_{loop} \qquad \text{Equation 4.2}$$

Using the calculated stoichiometric coefficients, measured internal and external temperatures of Figures 4.1 and 4.2, and the burn rate $\dot{m}_{wet}$ calculated from Figure 4.4, the energy budget and relative contributions of each component of equation 4.2 are determined and shown in Figure 4.10, following the analysis of Appendix B.2. Despite good agreement, the heat transfer to the fluid loop included in this energy budget is measured, not calculated.

Figure 4.10: Energy Budget of the Model 100 OWHH

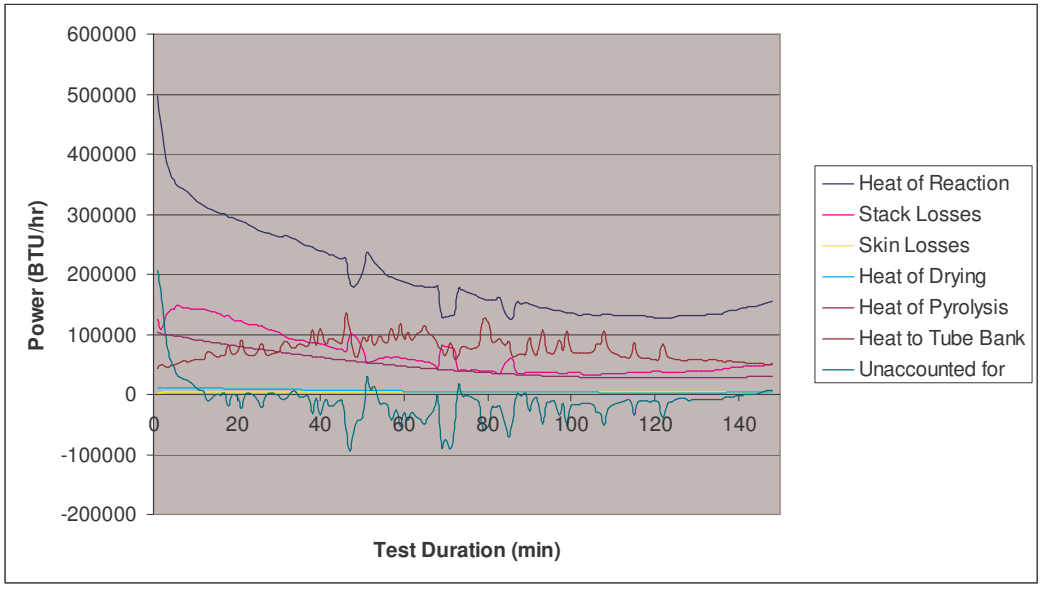

The remainder of equation 4.2, displaying the overestimation or underestimation of this analysis is shown in the 'Unaccounted for' data set. While the estimation of each component is not exact and a remainder of zero does not imply accurate results, this may be thought of as an approximation error. This remainder indicates (1) significant overestimation at the outset of the burn, (2) three significant underestimations corresponding with the three damper activations, and (3) overall underestimation throughout the char oxidation dominated portion beyond the 90th minute, explained accordingly:

(1) The Heat of Reaction is grossly overestimated during the first 5 minutes of the burn due to the simultaneous high enthalpy of reactants and low enthalpy of products estimations (relative to zero, as both enthalpies are negative). These are due to initially low internal temperatures relative to stack temperatures and high CO_2 to CO ratios.

(2) This analysis assumes steady state behavior, however the damper activation initiates transient behaviors that have significant lag times. The damper is activated to prevent the hot side of the internal fluid loop from boiling and does so by cutting off the inlet air. This causes a sharp drop in the Heat of Reaction, thus internal temperatures seen in Figure 4.1, however the hot and cold side of the internal loop drop in unison, seen in Figure 4.2, registering no net change in the heat transferred to the fluid loop. Additionally stack losses increase as the concentration of CO spikes.

(3) During the char oxidation dominated portion of the burn, many assumptions made are no longer appropriate. These include: maintaining composition of the 'wood molecule', including of moisture and the Heat of Drying, and the use of the empirically based Heat of Pyrolysis for the volatile phase.

Use of this analysis is acceptable, provided its use is restricted to the gas phase peak pyrolysis portion of the burn when steady state behavior has been established, roughly corresponding with the fuel rich portion of this burn between the 5th and 25th minute of the test.

Several items of interest arise from this analysis, giving insight into which portions of the CFD simulation require the most attention and highlighting which portions of the OWHH's operation are the least efficient. During the fuel rich portion of the burn, stack

losses are the most prominent proportion of heat utilized, a function of the stack temperature, PM emissions, and CO emissions; or more concisely, they are a function of incomplete combustion. Secondly, the skin losses are almost negligible, containing a maximum of 3.2% of the Heat of Reaction over the course of the test. This may seem counterintuitive, however a comparative glance between the internal and external temperatures of Figures 4.1 and 4.2 delivers a testament to the insulation within the Model 100. Lastly, while the Heat of Drying is similarly a small proportion of the Heat of Reaction the Heat of Pyrolysis, which empirically represents solid and gas phase pyrolysis [31], is not.

One might ask, why is it that the heat released and absorbed by the firebox refractory brick ignored during this energy budget analysis? As discussed in Chapter 3, the firebox material has the following thermal properties: C_p = 960 J/kg K and k = 0.66 W/m K. By design the brick has very high 'thermal inertia', thus once it is preheated it is approximated as a blackbody radiator for the duration of testing. Therefore, as these calculations assume quasi-steady state behavior between time intervals, the refractory is a heat source and sink of equal magnitude and the effect of its heating is captured by the use of internal measured temperatures.

4.2.3 PM and CO Oxidation

While it is difficult to perform a 'back-of-the-envelope' calculation when it comes to approximating the internal chemistry of the OWHH, certain assumptions and simplifications allow for order of magnitude determinations of PM and CO oxidation. The oxidation of these pollutants is to be examined for post-combustion zone conditions observed with simplified one-step global kinetic mechanisms.

Taking cues from the long studied kinetics of coal combustion, researchers have started to examine the kinetics of wood char oxidation within the last two decades. As previously discussed, PM emissions from wood combustion are both chemically and morphologically distinct from char, however char is better understood and its oxidation is more thoroughly studied. Janse et al. have determined experimentally that despite the application of several sophisticated pore models, the kinetics of pine char particles may be accurately represented by the so-called homogeneous rate equation. Assuming complete

particle oxidation, i.e. no mineral content, the rate may be determined by equation 4.3, valid over the range 573 K > T > 773 K. The parameters are as follows: k_o = 530,000 s^{-1}, E_A = 125 kJ/mol, n = 0.53, and the rate has the units [kg/(kg/s)]. From this mechanism, Figure 4.11 illustrates the effect of O_2 and temperature on the percent PM oxidized in the post-combustion zone [33].

$$r = k_o e^{-E_A/RT} P_{O_2}^n \qquad \text{Equation 4.3}$$

Figure 4.11: Percent PM Oxidation versus Temperature and O_2 Concentration

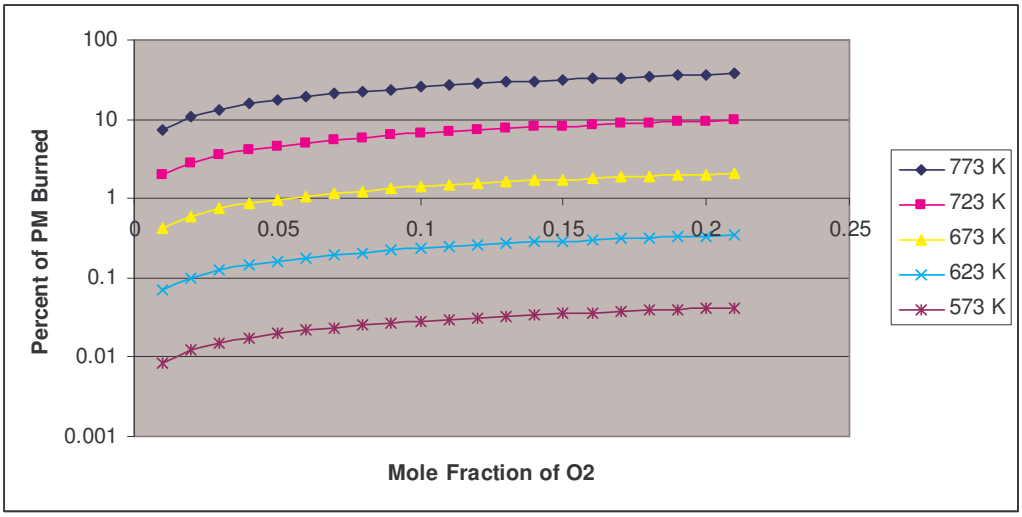

Inherent in this assessment of PM oxidation is the assumption that the operation is fuel lean, that is O_2 exists in the exhaust stream. Therefore it is imperative that the OWHH operate at least at stoichiometric conditions. As is often the case with Arrhenius rate kinetics, the reaction rate is heavily temperature dependent. With tube bank surface temperatures approximated as 450 K at peak pyrolysis, localized quenching of the PM oxidation kinetics is problematic and an extended post-combustion zone prior to heat extraction at the tube bank is necessary.

CO oxidation in the post-combustion zone is well understood, and is often modeled by the elementary step reaction seen in equation 4.4. While O_2 is not directly involved in the one-step mechanism, it is in the production of the hydroxyl radicals, as seen in the

mechanism in equation 4.5. Howard et al. have determined the mechanism in equation 4.6, with the following parameters: $k_o = 1.3 \cdot 10^{14}$ mL/mol s and $E_A = 30$ kcal/mol [30].

$$CO + OH \Leftrightarrow CO_2 + H \qquad \text{Equation 4.4}$$

$$\left.\begin{array}{l} H + O_2 \Leftrightarrow OH + O \\ O + H_2 \Leftrightarrow OH + H \\ OH + H_2 \Leftrightarrow H_2O + H \end{array}\right\} \qquad \text{Equation 4.5}$$

$$-\frac{d[CO]}{dt} = k_o[CO][O_2]^{1/2}[H_2O]^{1/2} e^{-E_A/RT} \qquad \text{Equation 4.6}$$

It is apparent that during fuel rich peak pyrolysis, this mechanism is not helpful in this analysis as the post-combustion O_2 concentration is zero. This mechanism will only prove useful once fuel lean operation is achieved.

4.3 CFD Modeling Decisions and Initialization

4.3.1 The FLUENT CFD Software Package

The CFD software used for modeling throughout this study is FLUENT Version 6.3, which uses finite-volume discretization to iteratively solve the coupled Navier-Stokes equations in addition to energy, species concentration, turbulent quantities, mixture fraction, or other modeled quantities as needed. It is a widely used commercial CFD software suite with a text-based and graphical user interface. Upon creation of a computational domain via the additional software entitled GAMBIT, boundary conditions are assigned, fluid zones are separated, and the meshing is performed. The grid is then loaded into FLUENT, boundary conditions are quantified, modeling decisions are made and required parameters are quantified, the solution scheme is selected, and the solution is initialized. Through the use of User-Defined Functions (UDFs), the user may customize any of these through a programmed and interpreted C code. The solution may be monitored during iterations by residuals and convergence of specific quantities, and if needed the grid may be refined in

arbitrary regions. Upon determination of convergence, the solution data may be post-processed in a number of ways, which highlights the advantage of such a software package.

The discretization the Navier-Stokes equations requires more care than that of scalar conservation or transport. As the Mach number of the OWHH is expected to be well below 1.0, the density-based solved will not be used. Favre-averaged Navier-Stokes equations provide the non-solenoidal form of the continuity equation as an additional constraint. However, through finite volume discretization of low Mach number flows treatment, this becomes a "kinematic constraint on the velocity field rather than a dynamic equation" [18]. The pressure gradient within the momentum equation is not explicitly determined between cells, and is modeled by a velocity coupling with the pressure gradient of the previous iteration (or the initialization), thus calculating the corrected pressure. The pressure-velocity coupling used throughout this study is the Semi-Implicit Method for Pressure Linked Equations (SIMPLE) algorithm for calculating the corrected pressure.

In order to prevent oscillatory behavior or divergence of the solution due to the nonlinear terms in the equations, under-relaxation factors (URFs) are used and changed along the iteration of the solution. For steady state simulations and iterations between time steps, the variables within the equation set are metered by use of arbitrary URFs according to equation 4.7 for the general variable φ. The value of φ from the previous iteration is adjusted by the calculated change in φ metered by the URF [22]. The values used for URFs are to be discussed during their usage.

$$\phi_{new} = \phi_{old} + (URF)\Delta\phi \qquad \text{Equation 4.7}$$

4.3.2 Convergence and Accuracy

As with all modeling exercises, especially iterative methods, two questions are important to answer, (1) what is the criterion for convergence of the solution, and (2) how accurate is the solution. In addition to the 'black-box' problem with use of commercially available numerical solvers, these questions require scrutiny.

This study uses a two-fold approach to judging convergence, monitoring of residuals and the convergence of important quantities. Residuals may be thought of as the remainder for each equation summed over the computational domain, as shown in the simplified

equation 4.8 for the general variable φ [18]. The discretized equation is reduced to simplified form, with Q as the solution vector and R as the remainder, or residual. superscript *n* denotes the iteration.

$$A\phi^n = Q - R^n \qquad \text{Equation 4.8}$$

The magnitude of this residual is difficult to use as a tool to determine convergence because of the large enthalpy gradients and small pressure gradients present. Instead, the judgment is based upon a scaled residual. The scaled residual for a given variable is the sum of cell residuals scaled by the sum of the center cell values. The commonly used limits of convergence are scaled residuals less than 10^{-6} for enthalpy, mixture fraction, and radiation, and are 10^{-3} for the remaining variables.

In addition to scaled residual monitoring, convergence is judged based upon the asymptotic behavior of important quantities. During iterative simulations, a known quantity for comparison, such as the mass-averaged stack temperature, is monitored and its convergence upon a certain value is an indication of convergence.

Upon determination of a converged solution, the accuracy of the results must be scrutinized. Ferziger et al. succinctly identified the three sources of CFD error [18]:

(1) *Modeling Error*, which is defined as the difference between the actual flow field and the exact solution of the model equations. Through the use of various modeling methods of the OWHH operation, this source of error is to receive the most attention throughout this study.

(2) *Discretization Error*, also known as grid dependency, is defined as the difference between the exact solution of the model equations and the exact solution of the discretized algebraic equations. Each grid is checked for grid dependency, that is, the effect of the solution by grid refinement. In addition, adaptive grid techniques afforded by the CFD software allow for mid-solution grid refinement in response to oscillatory and/or divergent behavior.

(3) *Iteration Error*, defined as the difference between the exact solution to the discretized algebraic equations and the converged solution. The two-fold convergence judging outlined previously will serve to minimize this error.

4.3.3 Grid Development

A computational domain is set up in the geometry pre-processing software GAMBIT, as shown previously in Figure 3.3. The domain inlets and outlet are indicated in Figure 4.12. The fluid zone in which the volumetric source of gas phase pyrolysis fuel species is introduced is 0.75" to the cribwood pieces normal to each face. Dimensions are determined through a combination of manufacturer's drawings and measurements made on the unit, to assure agreement with the existing Model 100. Note that the internal surfaces outside of the firebox are treated as smooth surfaces, neglecting the influence of the woolen insulation on the flow field. Difficulty in assumptions of friction factors and porous media geometry for this short thickness goes beyond the intended accuracy of these simulations.

In the meshing of the domain, areas in which large gradients were expected, smaller cells were employed and vice versa. The meshed domain consists of 104,000 cells, and is shown in Figure 4.12. While rendered in the Figure 3.3, the cribwood pieces, tube bank, and the exterior of air inlet tubing are all internal voids. The existence of these voids, in addition to many connections between rounded and rigid geometry, at the tube bank manifolds for example, and the inability to anticipate the direction of the many cell normal velocities, tetrahedral cells provide the most robust mesh geometry scheme.

Figure 4.12: Meshed Computational Domain of Model 100

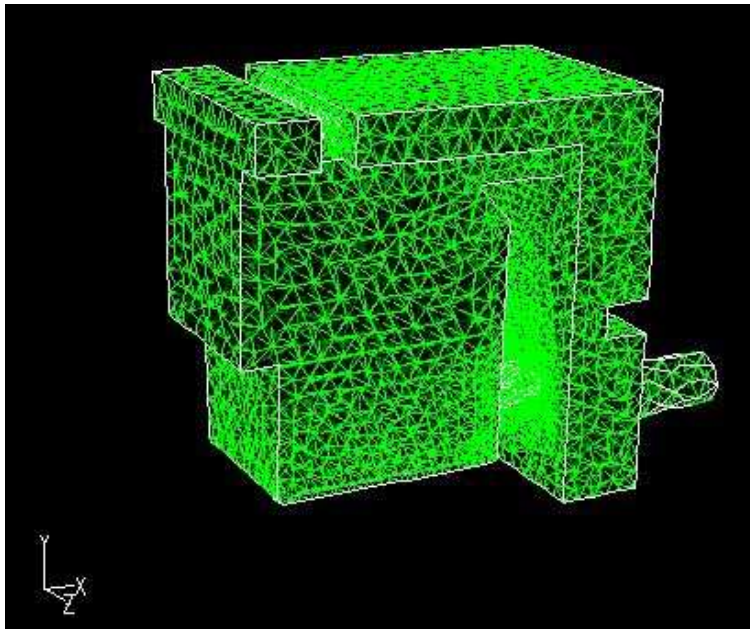

4.3.4 Modeling Decisions

Given the large number of modeling approaches available, as discussed in Chapter 2, one of the major challenges is to identify the specific approaches that will best address the goals of this project. The main challenges facing the model are (1) how to chemically characterize the composition of the fuel gases released by the wood into the computational domain during pyrolysis, (2) how to assess heat transfer during the burn, and (3) what approach to use to capture the physics of the turbulence. While our first interest is in PM formation and oxidation, these processes do not strongly affect the stoichiometry, heat release, or turbulence. Thus, the modeling will not initially focus on these steps.

Ten benchmarking runs were performed that assessed various combinations of modeling approaches. The modeling run numbers and how each facet is addressed are summarized in Table 4.1. It should be noted that simulations are not intended to be inclusive; rather they are to determine the effects of the geometry on the flow field and the mixing of fuel and oxygen.

Table 4.1: Summary of Benchmark Modeling Runs

Run	**Simulation**	**Fuel**	**Turbulent Combustion Model**
1	2D Steady	CH_2O	Mixture Fraction/PDF
2	3D Steady	CH_2O	Mixture Fraction/PDF
3	3D Steady	CH_2O	Mixture Fraction/PDF & Pyrolysis Mechanism
4	3D Steady	Huttenen 1	Mixture Fraction/PDF
5	3D Steady	Huttenen 2	Mixture Fraction/PDF
6	3D Steady	Galgano	Mixture Fraction/PDF
7	3D Steady	Huttenen 1	Mixture Fraction/PDF & Flamelet
8	3D Unsteady	Huttenen 1	Finite Rate/Eddy Dissipation
9	3D Unsteady	Huttenen 1	Finite Rate/Eddy Dissipation & LES
10	2D Steady	CH_2O	Mixture Fraction/PDF & Soot Model

The comparisons of the various approaches to the problem of wood gas composition, turbulence, and turbulence/chemistry interactions are addressed as follows:

(1) The physics of turbulent non-premixed flames is inherently a three-dimensional phenomenon, the loss of detail in two-dimensional modeling is assessed between runs 1 and 2.

(2) Addressing the different methods of approximating the gas phase pyrolysis species of Table 2.4, direct comparison is made between runs 2, 4, 5, and 6. CH_2O refers to the empirical surrogate molecule and the remaining are identified by the referred article author.

(3) The effect of a pyrolysis limited fuel inlet boundary condition will be explored using an algorithm for equation 2.5 in run 3.

(4) The non-equilibrium flamelet approach to the mixture fraction model, for which the scalar dissipation defined in equation 2.42 dictates the finite rate chemistry, is implemented in run 7.

(5) The effect of a transient simulation, needed in the capturing of the periodic dilatation and shear layer effects of the reacting plume, and finite rate/eddy dissipation turbulent chemistry model are explored in run 8, with the same fuel approximation as runs 4 and 7 with the four step mechanism in Table 2.5. Note that the mechanism from Huttenen et al. was not used due to the lack of a direct CO oxidation step, causing initial simulations to be unstable. The mechanism from Galgano et al. will be used exclusively in this study.

(6) The use of LES to model turbulence, rather than the k-ε used in all other runs, is explored in run 9 for direct comparison with run 8.

(7) The two-step soot nucleation and formation model outlined in Section 2.2.1 is to be implemented in run 10, for comparison with run 1.

For modeling scenario 3, the fuel gas influx boundary condition is modeled with a pyrolysis mechanism according to equation 1, based upon a zeroth order Arrhenius rate with pre-exponential constant of 4.37E+06 m/s, an activation energy of 143 kJ/mole, local gas density, the volatile fraction, and the surface area of the cell face. This is programmed into the CFD package using a User-Defined Function (UDF). During preliminary simulation of run 3, a runaway steady state pyrolysis rate during occurred, due to the feedback mechanism of increased local temperatures causing higher fuel emissions, causing higher flame temperatures, and so forth. To prevent this, a ceiling at the maximum observed firebox temperature is set as the steady state mass flux for each cell with the pyrolysis boundary condition algorithm.

The internal heat transfer and energy budget analyses performed earlier resulted in good agreement to data. Thus we did not work extensively with options for heat transfer. For all ten runs, radiation exchange is modeled with the Discrete Transfer Radiation Model (DTRM) [22]. To account for specific absorption bands of species mixtures, notably the influence of moisture, the absorption coefficient is determined by the domain based weighted-sum-of-gray-gases model (WSGGM) [50].

4.3.5 Boundary Conditions

As the goal is to simulate an instantaneous snapshot of the furnace internally during the peak of gas phase pyrolysis, including the unsteady runs 8 and 9, the quantities from test data to be used are averaged between the 5^{th} and 25^{th} minute. Opacity observations and Figure 4.5 suggest that this peak pyrolysis period encompasses the majority of PM emissions. Additionally, time averaging of data smoothes out any measurement anomalies due to sparse data sampling from a notably transient process.

The mass flux of fuel gas and air entering the system, with the exception of run 3, are set by $\dot{m}_{wet}$ and the calculated Θ for the time-averaging interval, for which the minimum value of Θ is 0.852, expected to be the point of peak pyrolysis. The fuel gas is chemically defined as per Table 4.1, and for the use of the mixture fraction model, Z = 1 at the fuel inlet and Z=0 at the air inlet per equation 2.36. Boundary values of k and ε are determined per Appendix C. Air enters the preheating tubes at atmospheric pressure and 300 K. Turbulent quantity boundary conditions are determined per Appendix C.

Internal surface temperatures are determined by a combination of test observations and the previous analyses. The average water tube exterior surface temperature is estimated as 450 K, the average internal refractory brick surface temperature is the observed 800 K, and the wood surface temperature is assumed to be 573 K, which is the observed solid phase pyrolysis temperature [31]. Throughout the previous analyses, the average convective heat transfer coefficients were determined. While the wall and tube bank boundary conditions could be set by coefficients rather than an assumed surface temperature. In doing so, stability issues arose in their implementation due to the requirement of an assumed T_∞ and the arbitrary split between the cross and parallel flow regimes. For example, in the tube

bank zone, the assumed T_∞ is the measured secondary temperature, which results in unrealistic heat fluxes during the simulation of the burn ignition, which quenches reactions and the radiation calculations cause the solution to diverge. It would be possible to 'guide' the simulation during this ignition phase, however much less assumptions are involved in the prescription of a surface temperature.

As noted previously in the grid development, the gas phase pyrolysis species are modeled as a volumetric source term within an internal fluid zone adjacent to the cribwood surface rather than a solid boundary inlet. This is to avoid underestimations of intra-cell concentration gradients at the internal fuel inlet boundaries. It was found that during initial modeling that the introduction of trace fuel species mass fractions or mixture fractions, trace with respect to the mean flow after initialization, intra-cellular mass fraction fluxes were grossly underestimated even with grid refinement. Numerically, the species mass fraction and mixture fraction gradients are interpolated by the difference between the facial values in the direction of the mean velocity. Due to enforced numerical stability via URFs and upwind discretization, the gradients are underestimated resulting in the overestimation of fuel species transport. To rectify this numerical stability problem, the fuel species are introduced as volumetric source terms (appearing on the right hand side of transport equations), and mass is conserved based upon the volume of the burn zone.

For the model runs employing the mixture fraction combustion model, the look up tables are created, as discussed in Section 2.4.4. With the exception of run 7, the look up tables are calculated for temperature, density, and species mass fraction, in terms of the mean and scaled variance of the mixture fraction for various scaled heat fluxes using an equilibrium chemistry algorithm and the β-distribution assumed-shape PDF. For model run 7, which employs the non-equilibrium modeling of reaction through the flamelet theory, a library of flamelets are calculated for the abovementioned variables are defined strictly in terms of the mixture fraction and scalar dissipation, χ. From this library, a look up table is computed in a similar fashion to that of the previous runs. The look up tables for temperature (z-axis), in terms of the mean (x-axis) and scaled variance (y-axis)of Z in the zero heat flux case are shown below in Figures 4.13 through 4.17 for each run. Note that the runs 2, 3, and 10 also use the look up table from run 1.

Figure 4.13: Look Up Table for Runs 1, 2, 3, and 10

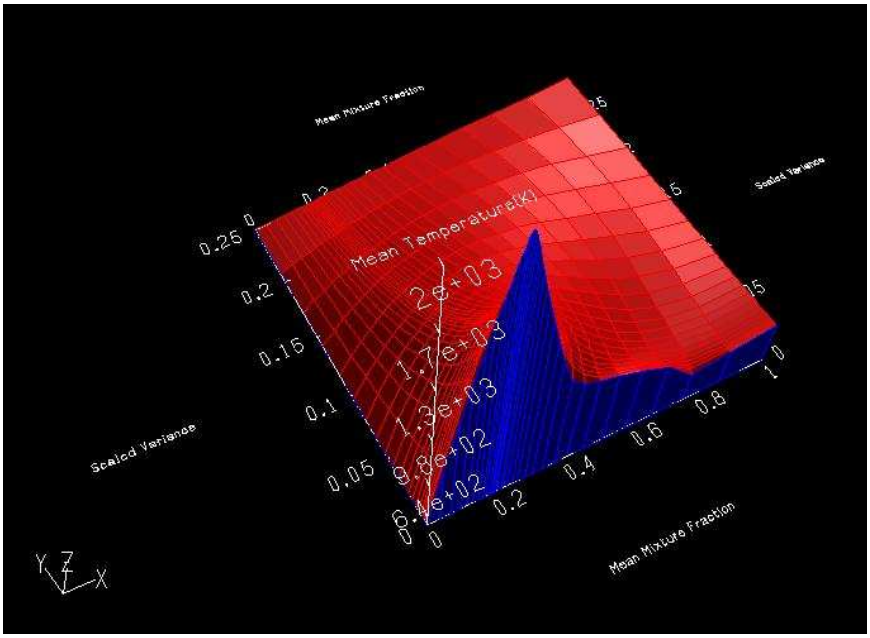

Figure 4.14: Look Up Table for Run 4

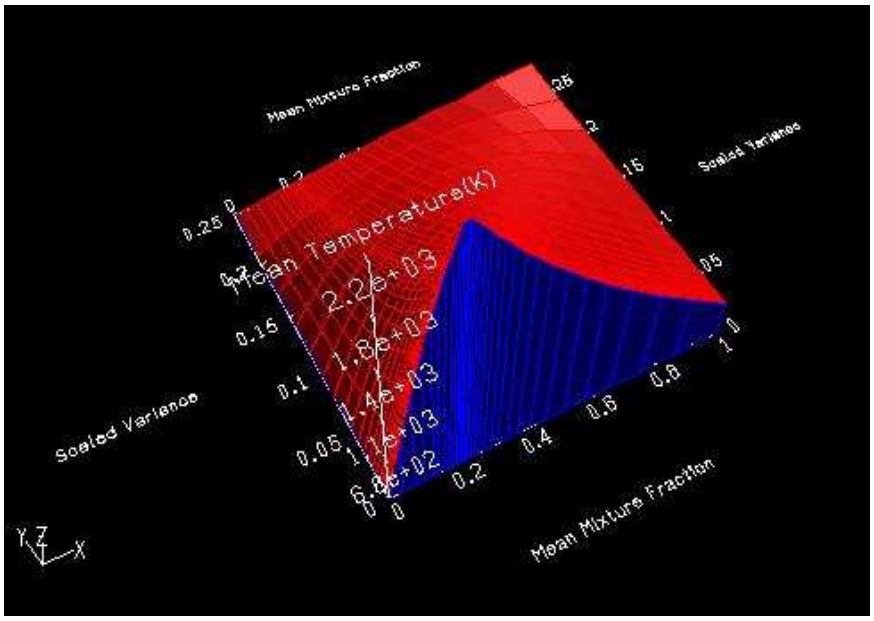

Figure 4.15: Look Up Table for Run 5

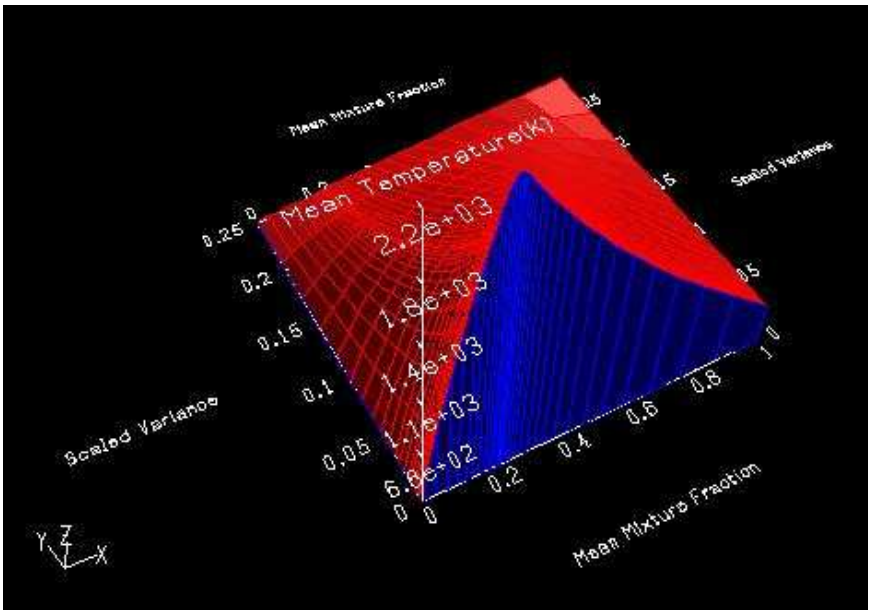

Figure 4.16: Look Up Table for Run 6

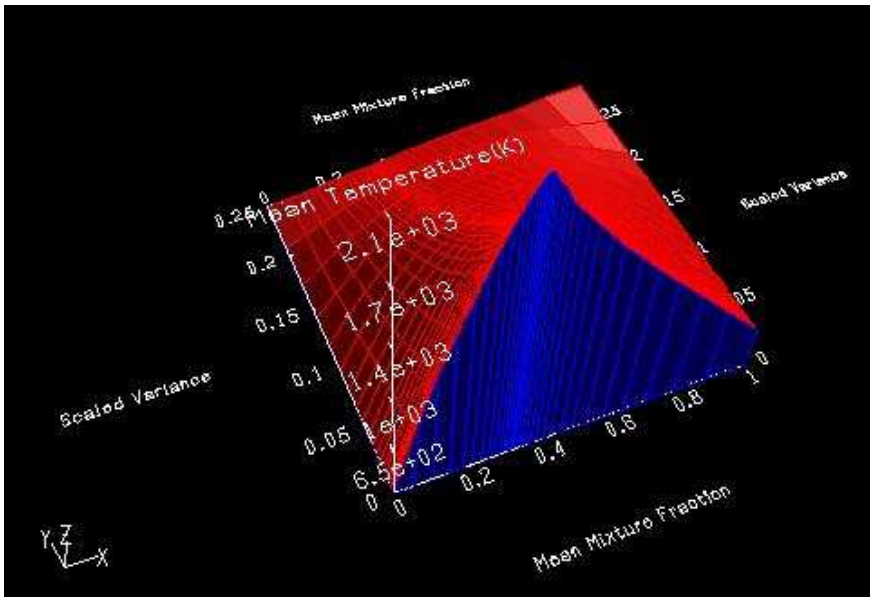

Figure 4.17: Look Up Table for Run 7

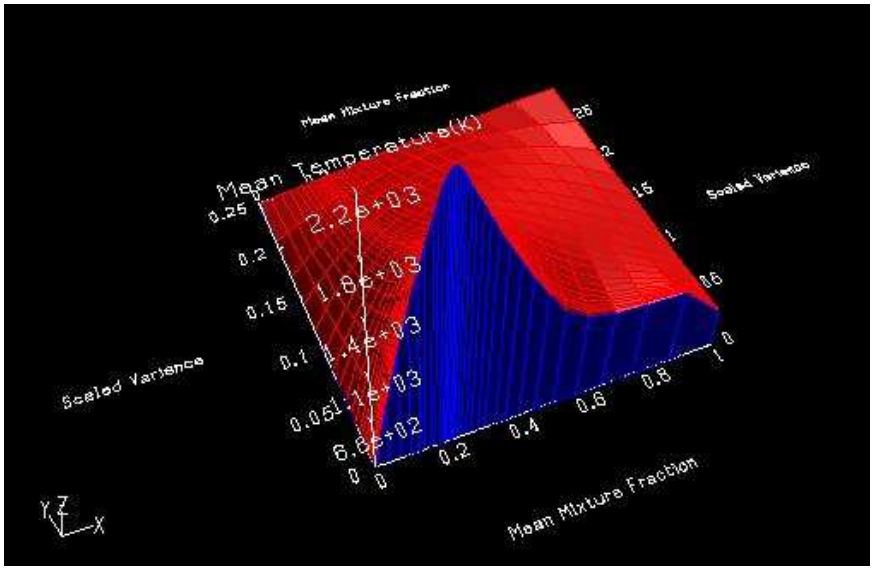

The temperature peak corresponds with the stoichiometric point for a given scaled variance, and shifts from look up table to look up table due to the differing heating values of the 'fuels'. The stoichiometric values of Z_{mean} at a scaled variance and heat flux of zero are as follows: Figure 4.13, $Z_{mean,stoich} = 0.1797$, Figure 4.14, $Z_{mean,stoich} = 0.2016$, Figure 4.15, $Z_{mean,stoich} = 0.2000$, Figure 4.16, $Z_{mean,stoich} = 0.3156$, and Figure 4.17, $Z_{mean,stoich} = 0.2016$. Towards the 1.0 side of the mean mixture fraction Figures 4.13 and 4.17, the temperature plot takes on a more uneven shape than that of the three equilibrium and mixture based fuel due to modeling of gas phase pyrolysis. In the case of the surrogate wood molecule CH_2O, the empirical fuel will degrade initially into the fuel species CH_4, CO, and H_2 according to the equilibrium chemistry solver, which are consumed at differing rates in the fuel lean regime ($Z_{mean} > 0.1797$). The same effect is seen in Figure 4.17, for the same reasons, as the flamelet library calculated prior to the look up table was based upon the Gas Research Institute (GRI) mechanism for natural gas combustion version 3. [28]

4.3.6 Simulation Strategy

While each simulation requires specific methodology relative to the iterative behavior, solution stability, values of important quantities, and modeling methods, a cohesive overall strategy is used in each case. The simulation is always initialized,

establishing the first iterative 'guess' for each cell, with the values at the air inlet. Natural draft or forced draft, fuel lean or rich, the air inlet boundary conditions have more bearing on the solution velocity field and species/mixture fraction field than does the fuel species inlet. Due to the great effect the combustion modeling has on the flow field, a so called 'cold flow' simulation, without reactions or radiation, is converged to establish a better pre-combustion initialization specific to the OWHH geometry. The reacting models and boundary conditions are implemented, and in addition look-up tables, flamelets, and reaction mechanisms are determined if necessary. To prevent oscillatory behavior during ignition, iterations are damped for density and mean mixture fraction/fuel species via reduced URFs. If internal temperatures indicate stalled ignition, a temperature of 900 K is patched into the burn zone and the simulation, then the simulation is run to convergence. Lastly, due to stability issues during the ignition phase, radiation modeling is initiated and the simulation is run to convergence. Finally, to assure accurate chemistry modeling and convective species transport, the pressure and mean mixture fraction/fuel species URFs are increased and the momentum URF is reduced, and the simulation is run to convergence.

During unsteady simulations this simulation strategy is used, however each time step contains an iterated steady state simulation. Therefore convergence must be judged differently, as the 'steady state' time step is reached. Primarily, it is determined by the asymptotic behavior of the mass-averaged stack exit temperature and CO_2 mass fraction, and simulations proceed with time steps of 0.1 s.

4.4 Benchmark Modeling Results

The 10 benchmark simulations are compared to the following measured quantities: time-averaged temperatures at the firebox, secondary, and stack thermocouple locations, and the CO_2, O_2, and CO stack dry gas concentrations. While the previous analysis revealed that during peak pyrolysis the Model 100 runs fuel rich, due to cost and that Method 28 does not require it, fuel species stack dry gas mole fractions were not measured. Simulations allow for these species to be reported, therefore simulation stack dry gas concentrations of H_e and CH_4 are reported as well.

Figure 4.18: Internal Temperatures of Test Data vs. Simulations

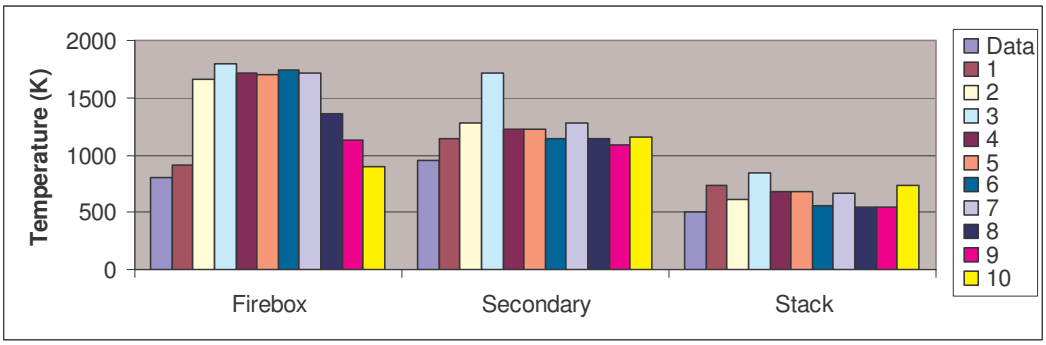

In Figure 4.18, it is apparent that many methods of characterizing the gas-phase pyrolysis products and their chemistry overestimate firebox temperatures. With the exception of the 2D simulations in runs 1 and 10, mixture fraction modeling with equilibrium or non-equilibrium chemistry grossly overestimates flame temperatures. It should be noted that the maximum flame temperature of the 2D solution is within 7% of the 3D mixture fraction model equivalent, run 2. The reported internal temperature at the thermocouple location is somewhat misleading, as in the 2D simulation the flame is drawn to the air side of the firebox.

For the moisture content of 17.621% on a wet basis, these temperatures approach the adiabatic flame temperature plotted in Figure 2.10. With the exception of the flamelet-based run 7, these temperatures are overestimated for the following reasons: they assume equilibrium chemistry and a limited number of product species, steady state solutions remove any influence of transient heat sinks, and local quenching of the flame by rich or humid parcels or excessive strain rates are underestimated by the assumed shape PDF with the RFL used. With the exception of steady state simulation, run 7 accounts for these issues by virtue of steady flamelet modeling, as discussed in Section 2.4.2.1. The combination of the slow buoyancy-induced convective transport of the mixture fraction and the fuel rich operation results in small mixture fraction gradients and thus low scalar dissipation rates, χ, as defined by equation 2.42. The regions of high scalar dissipation rates are restricted to between crib pieces, as seen in Figure 4.19, and overall the effect of including flamelet modeling is small. For this reason, the transport of Z_{mean} and $Z_{variance}$ in runs 4 and 7 do not differ much, and additionally the temperatures are overestimated due the similarities in the fuel rich side of the look-up tables from which they are drawn in Figures 4.14 and 4.17. The

contours of Z_{mean} are shown on a surface of the minimum value of $\chi = 0.01\ s^{-1}$, corresponding to a unique flamelet for which there are 10 calculated. The maximum value for the domain is $\chi = 0.58\ s^{-}1$; therefore with the lowest of anticipated scalar dissipation rates restricted to the near cribwood region and at the tube bank inlet (tubes not shown for clarity), the non-equilibrium flamelet approach in run 7 reports similar benchmarking temperatures to the equilibrium approach in run 4 at an increased computational cost.

Figure 4.19: Contours of Z_{mean} on Iso-surface of Scalar Dissipation = 0.01 [s^{-1}] for Run 7

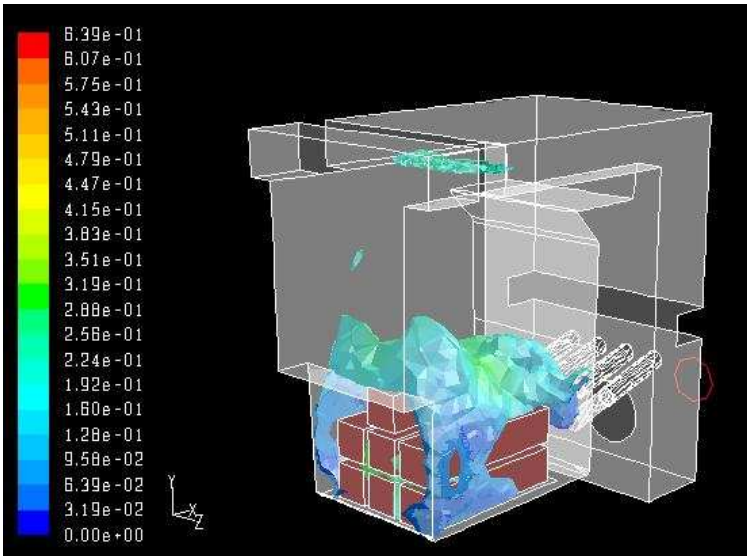

While better in agreement with measured temperatures, the unsteady simulations of run 8 and 9 also reported higher firebox temperatures. For the presented methods of chemistry characterization, the overestimations of temperature, and thus CO oxidation, are not seen as a fatal flaw of simulation. In conjunction with a sophisticated proprietary pyrolysis sub-model, CFD simulations of a fireplace performed by Huttenen et al. reported near-flame temperatures and CO mole fractions that were as much as 400% off from time-averaged measurements. They cited that the transient behavior of the measurements also may skew results, as wood log flame temperatures vary greatly within a small space [31). These combustion modeling techniques were initially validated against well-defined turbulent jet flames, for which they perform quite well. The modeling and experimental techniques in characterizing chaotic and buoyant flames of this nature continue to be an area of research and improvement across many disciplines.

As an indication of good heat transfer and post-flame combustion modeling, the secondary and stack temperatures show much better agreement across the simulation runs. The noted exception is run 3, for which the fuel pyrolysis rate is set by the pyrolysis model, which is determined by the adjacent cell temperature of the wood surface. Here the simulated fuel burn rate is reduced from the observed 0.00663 kg(dry)/s to 0.00512 kg(dry)/s. Spatially, the pyrolysis rate is underestimated on lower logs where the colder air enters the firebox and overestimated above upper logs receiving irradiation from the flame. This causes the entire flame to lift off the logs and maximum temperatures reach beyond the secondary thermocouple location, thus overestimating combustion efficiency with a reduced fuel emission rate. Additionally, stack temperatures are overestimated due to the effectively shortened exhaust path. Stack temperatures for the two 2D simulations, runs 1 and 10, are also overestimated due to the difficulty of representing the effect of the tube banks, and their associated heat extraction, on the flow field.

Figure 4.20: Stack Species Concentrations of Test Data vs. Simulations

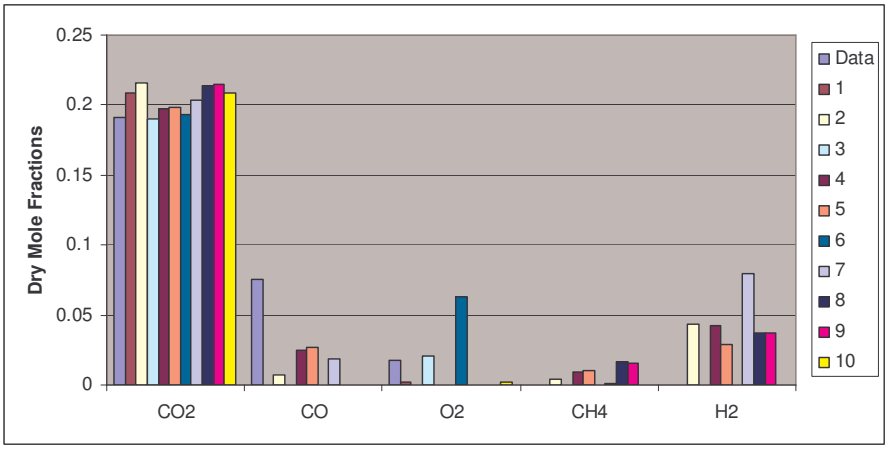

In Figure 4.20 dry stack gas species concentrations of CO_2, O_2, and CO are mixed in their agreement with measured data. CO_2 concentrations showed good agreement with the test data, however CO concentrations were consistently underestimated. Like local density and temperature, the local concentration of a given species is solely a function of the conserved scalar Z for all simulation runs except 8 and 9. Thus, as these simulations overestimated firebox temperatures, it also overestimates the completion of combustion in the form of higher CO_2 and lower CO concentrations. Runs 4, 5, and 7 had a significant

exhaust CO concentration due to their treatment of CO as a significant portion of the modeled fuel. This was not the case for run 6, as the modeled fuel had less CH_4 and H_2, thus a lower heating value as evident by the higher Z_{stoich} in Figure 4.16, causing the 'fuel' CO to be consumed at a higher rate and 'exhaust' CO to be produced at a lower rate. This also explains the overestimated O_2 reported for run 6.

Using the same fuel species mass fractions as run 4, the unsteady runs 8 and 9 reported lower average stack CO concentrations by almost two orders of magnitude. Noting the comparatively lower firebox temperatures in Figure 4.18 for these unsteady runs, this is initially puzzling. Additionally, these two runs were the only two to report no O_2 at the outlet, with those others not visible on Figure 4.20 at less than tenths of a percent and below. Partial responsibility lies within the four-step global mechanism used, seen in Table 2.5. The CO oxidation step (reaction 1) is prevalent on the air side of the cribwood, with the forward water gas shift step (reaction 4) remaining as the only CO consuming step, as seen in contours of reaction rate in Figures 4.21 and 4.22. Reaction 1 requires high temperatures, due to its high activation energy, and fuel lean conditions causing it to cease beyond the firebox. The forward rate of reaction 4 is able to continue in post-combustion low temperatures, and the reaction rate at the stack is only three orders of magnitude less than the domain maximum. The reverse of reaction 4 is not significant in the simulation given lower post-combustion temperatures and high moisture content of the exhaust, at a stack concentration of 20.2%. Slightly higher rates of reaction 1 and 4 are seen in run 9, however the trends remain. Therefore it is expected higher firebox temperatures overestimate the rate of reaction 1, for which the oxidation of CO is known to be heavily temperature dependent as seen in equation 4.6. If at measured firebox temperatures, it is expected that there will be less direct oxidation of CO, O_2 will be a minor stack specie per measured data, and the slower forward rate of reaction 4 will be unable to consume as much CO.

Figure 4.21: Run 8 Z-dir Contour of Reaction 1 Rate [kgmol/m^3 s]

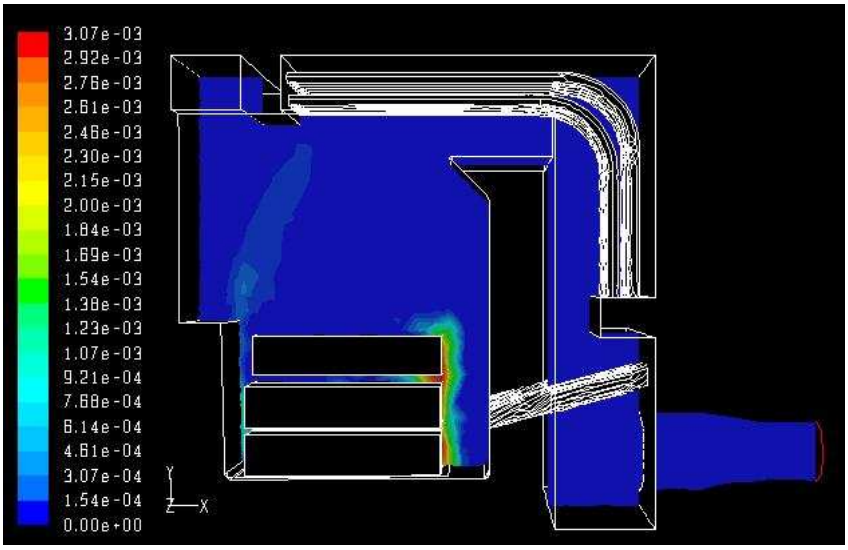

Figure 4.22: Run 8 Z-dir Contour of Forward Reaction 4 Rate [kgmol/m^3 s]

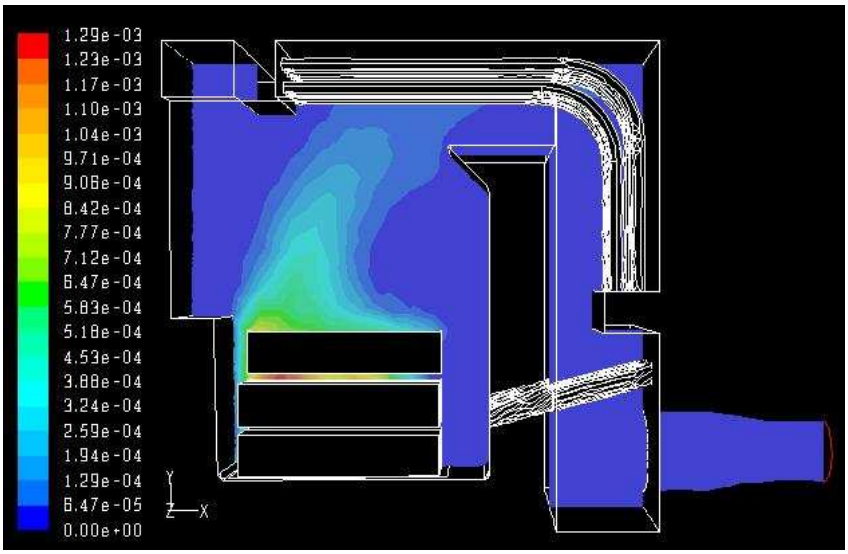

Within the modeling of finite rate/eddy dissipation chemistry, there exists a switch for modeling both chemistry-limited and mixing-limited reaction rates. The net production/destruction rate of species *i* is determined by the minimum of the Arrhenius and the eddy-dissipation rates, seen in equations 2.28 and 2.62 respectively. Key to the determination of the mixing or chemistry limited reaction rate is eddy mixing time scale, k/ε. The eddy dissipation model postulates that reaction rate kinetics is inversely proportional to this time scale, which if large will be rate limiting for combustion. It should be noted that

even if reactions are chemistry-limited, that is too cold or insufficient amounts of reacting species, the mixing is not deemed sufficient. During natural draft operation, a significant amount of the flow field is not fully turbulent and operation is fuel rich, and as it turns out the Arrhenius rate is the limiting rate for much of the domain. This can be seen in Figures 4.23 and 4.24, which illustrates the turbulent and Arrhenius forward reaction rates of reaction 4 in run 8. Figure 4.23 bears a resemblance to the total reaction rate seen in Figure 4.22, which is expected from consistently higher turbulent reaction rates seen in Figure 4.24.

Figure 4.23: Run 8 Z-dir Contour of Arrhenius Forward Reaction 4 Rate [kgmol/m^3 s]

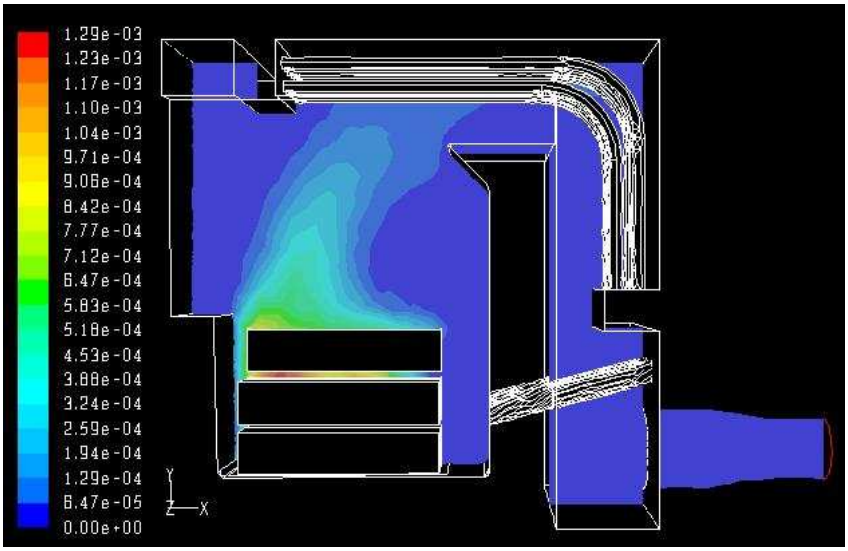

Figure 4.24: Run 8 Z-dir Contour of Turbulent Forward Reaction 4 Rate [kgmol/m^3 s]

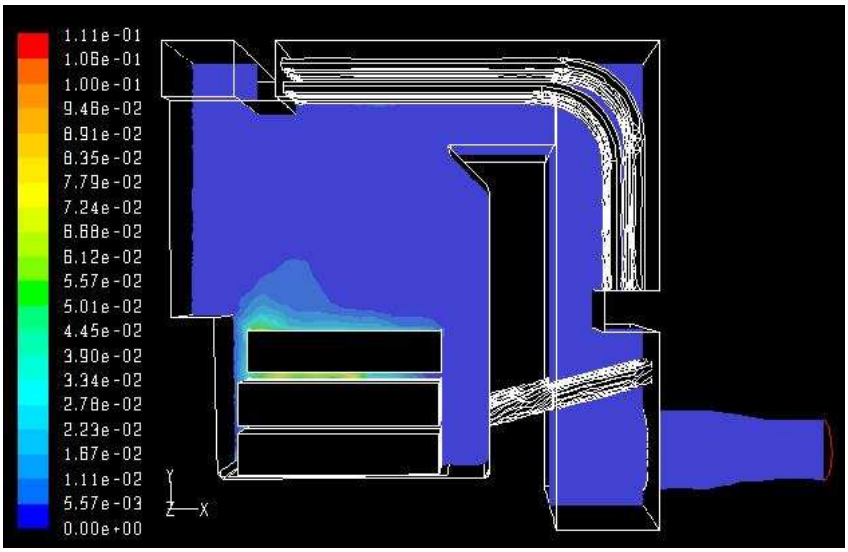

Reported dry gas mole fractions of O_2 did not show good agreement with test data, due to the tendency to overestimate firebox temperatures and thus combustion efficiencies. Run 3 reported the a dry gas stack concentration at 2.03% O_2, in good agreement with the time-averaged test data, but was likely due to the overestimation of stratified air distribution and smaller modeled $\dot{m}_{wet}$ for reasons mentioned previously. With the assumption of spatial uniformity in the z-direction and thus no lateral mixing within the tube bank, the 2D runs 1 and 10 reported small mole fractions of O_2. Lastly, run 6 grossly overestimated O_2 concentrations, and subsequent expected underestimations of fuel species emissions, due to the low heating value of the assumed fuel mixture.

The fuel species H_2 and CH_4 were not measured during testing, however it should be noted that they were significant portions of the simulation stack concentrations, supporting the initial determination of fuel rich operation despite measured O_2 in the stack. The existence of these species in the stack appears to be dependent on the composition of the fuel mixture. Runs 4, 7, 8, and 9 all assume the same fuel mixture composition and all report fuel species emitted, with the fuel composition of run 5 similar proportions of CH_4 and H_2 as well. The smaller proportion of H_2 in run 5 compared to run 4 explains the reduced emissions. It is likely that while runs 1, 2, 3, and 10 share the same fuel composition, only run 2 reported fuel species emitted strictly due to lower stack temperatures. Despite only a

difference in stack average Z_{mean} of 0.075%, the spike in H_2 emitted in run 7 compared to run 4 is due to the equilibrium vs. flamelet developed look up tables, seen in Figures 4.14 and 4.17respectively. Several steps within the GRI-mechanism produce H_2 as a product.

4.5 Discussion of Simulation Techniques

In the benchmarking of modeling methods made in these ten scenarios, there are many results in which comparison to measured data is not possible. While the discussion of measured data versus simulation results covered internal heat transfer, wood pyrolysis gas species treatment, and combustion modeling techniques, three important aspects of the simulations cannot be compared to measured quantities. These aspects are: (1) the effect of transient or steady state modeling and its importance to the periodic behavior of buoyant reacting plumes, (2) the use of the 2D soot nucleation and formation model, and (3) the comparison between modeling turbulence with k-ε and LES models.

An important feature of buoyant flames is the "puffing" that is caused by toroidal vortex formation and shedding. The shedding increases strain rates at the flame sheet, which acts to both enhance mixing (reducing PM and CO) and to promote extinction (increasing PM and CO). This effect is time-dependent, therefore it is important to assess whether this effect is negligible or if a transient simulation is required to capture this phenomenon. Runs 4 and 8 are to be compared; the difference between the two is the steady state mixture fraction vs. transient finite rate chemistry modeling. For run 4, the leftmost term in each transport equation see in Table 2.7 is eliminated. To visualize this puffing, contours of vorticity magnitude are plotted for the two runs in Figures 4.25 and 4.26, with the expectation of an observable dissipation of vorticity at the rising plume boundary. In distribution and magnitude, there is not a fundamental difference between the two. Rather than suggest that they capture this vortex shedding equally well, it is likely that this transient phenomena is not important within the OWHH. While the unit is natural draft and buoyancy drives the air into the firebox, the transient effects within are more likely to be a function of the wood burn rather than the flow field. The primary driver of this 'puffing' is the density gradient across the plume boundary, causing the baroclinic torque, which is expected to be much smaller within the firebox than in open air fires. Therefore,

the steady state and transient simulations are expected to perform similarly with respect to this 'puffing', which is expected to be minor.

Figure 4.25: Run 4 Z-dir Contour of Vorticity Magnitude [s^{-1}]

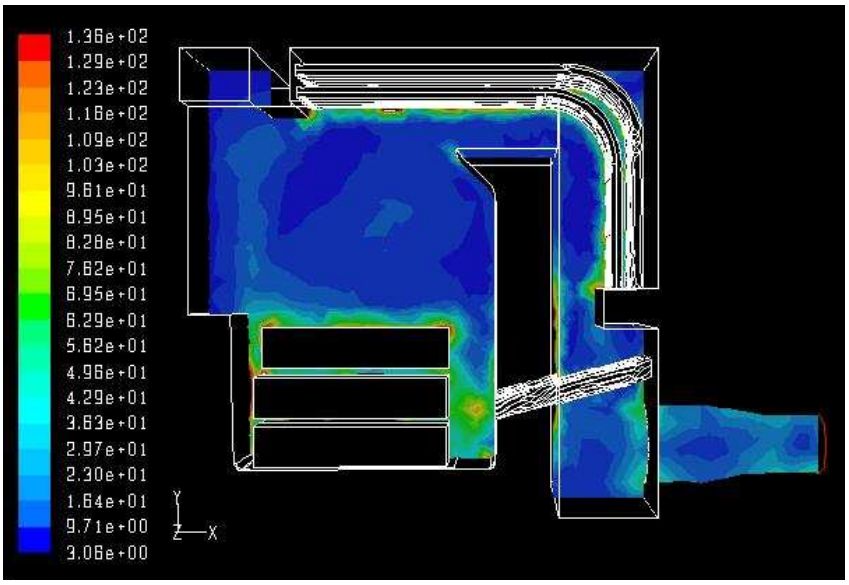

Figure 4.26: Run 8 Z-dir Contour of Vorticity Magnitude [s^{-1}]

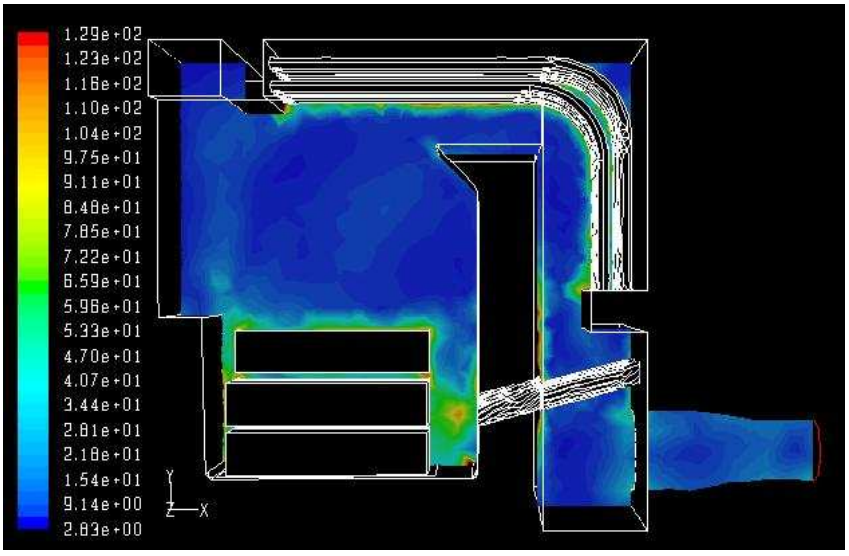

Despite previous caveats made about the inapplicability of modern soot formation and oxidation theories and modeling techniques, compounded by the small fraction of PM emissions composed of true BC soot, the two-step nucleation and formation model of

Tesner [46] was employed in with the 2D mixture fraction model run 10, outlined in Section 2.2.1. The sooting fuel was set as CH_4, the secondary fuel constituent upon thermal degradation of the empirical CH_2O fuel. The soot density can be seen in the contour plot of Figure 4.27, indicating near complete exhaust oxidation, a likely result of overestimated internal temperatures. While the predication of maximum soot density is likely to be in agreement with operation, there is not an experimental validation method. In addition, during peak pyrolysis, test data recorded roughly a 0.14 kg/hour. Ignoring that which is oxidized, the modeled soot formation rate does approach this with the maximum domain sooting rate at 3.09e-9 kg/m^3 s. Therefore, the caveats shall be heeded and modeling of soot formation shall not be used in further study, and the efficiency of combustion of fuel species shall continue to be used as a metric of PM emissions during simulation. More so than many theories, modeling techniques, and experimental methods discussed throughout this study, the formation and oxidation of organic PM is a constantly changing field of study and has very far to go towards a full understanding of the fundamental mechanisms.

Figure 4.27: Run 10 Z-dir Contour of Soot Density [kg/m^3]

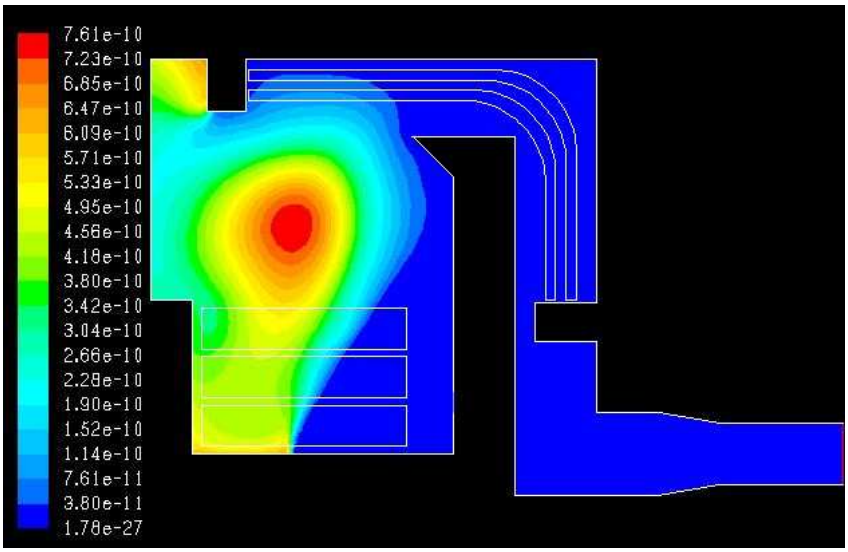

Recalling the shortcomings of the k-ε turbulence model, with it the assumption of isotropy and the turbulent viscosity hypothesis, its performance against LES will be assessed in capturing of the large scale flow field structures. Runs 8 and 9 provide a side-by-side comparison, and both objective and subjective metrics can be examined. The turbulent

viscosity ratio, defined as the ratio between the turbulent and laminar viscosity, is an indicator of high turbulent intensities. The maximum turbulent viscosity, subgrid in the case of LES, within the domain of runs 8 and 9 are 90.03 and 18.30 respectively. The location of this maximum in run 9 is where one might expect, at the interface between the cribwood inlet air and also at the entrance region of the stack. However the location of the maximum for run 8 is near the backside of the hot side fluid manifold, in the upper left hand portion of the domain (see Figure 4.26). Interestingly in run 8, turbulent viscosity ratios in the region of the run 9 maxima, similar magnitude ratios are seen. This illustrates the advantage of LES, in that the turbulence caused by the 'dead zone' in this upper left hand corner is modeled directly, whereas the k-ε model assumes isotropy in this large scale structure and underestimates turbulent intensities due to overly diffusive modeling. These large structures captured by run 9 are vital to the convective transport of heat and species. While the exact location of the flame surface is unknown, the consumption of CH_4 via reaction 3 can be used as an indication of proximity to the flame. Figures 4.28 and 4.29 illustrate this convective transport by contour plots of temperature on an iso-surface of reaction 3 rate of 0.001 kgmol/m^3 s, with the tube bank removed for clarity. This is not intended to exactly represent the flame surface, as the reaction rate is an order of magnitude less than the maximum in both domains; however this reaction rate indicates that LES distributes reactive species and heat outside of the mean flow much more so than k-ε modeling.

Figure 4.28: Contours of Temperature (K) on Iso-surface of Reaction 3 Rate = 0.001 [kgmol/m^3 s] for Run 8

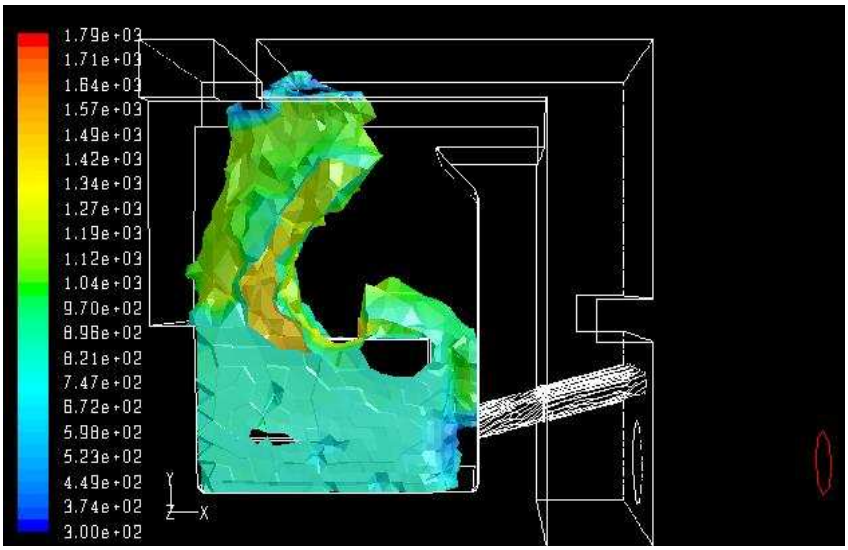

Figure 4.29: Contours of Temperature (K) on Iso-surface of Reaction 3 Rate = 0.001 [kgmol/m^3 s] for Run 9

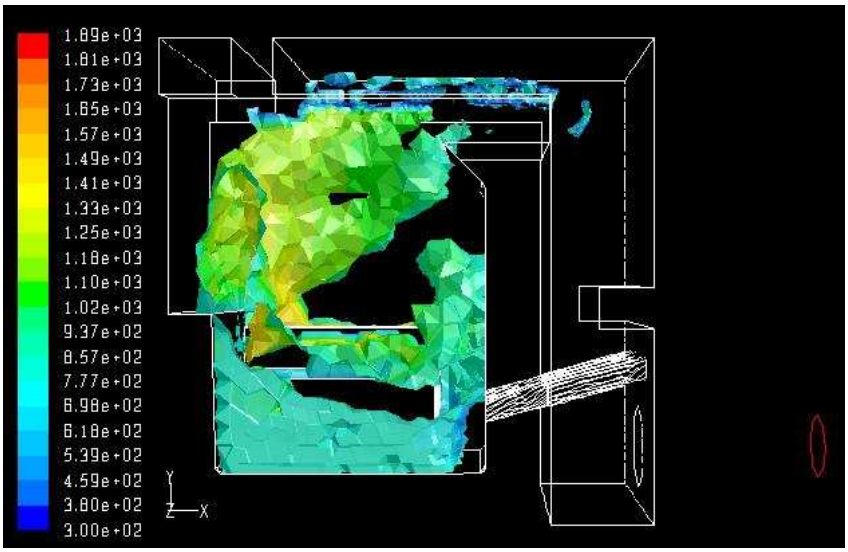

Using visualization of the fluid particle pathlines, the mean flow of each run may be examined. Figures 4.30 and 4.31 show the pathlines of runs 8 and 9 colored by particle ID number, with adjacent pathlines skipped for visual clarity. While no new objective conclusions may be drawn from the pathline visualization, additional context is provided for the previous two determinations. In run 8, the smooth trajectories within the so called 'dead

zone' of appear unrealistic and the large scale circulation zone above the firebox air inlet is too coherent for the expected chaotic motions within the OWHH. This circulation prevents lateral dispersion of heat and species seen in Figures 4.22, 4.23. and 4.28. By comparison, pathlines of run 9 show the advantage of directly modeling the large scale turbulent structures, in the capture of chaotic motion expected resulting in thermal transport and the best agreeing firebox temperatures with experimental data. This physical realism comes at a computational cost however, at over 25,000 iterations.

Figure 4.30: Pathlines for Run 8

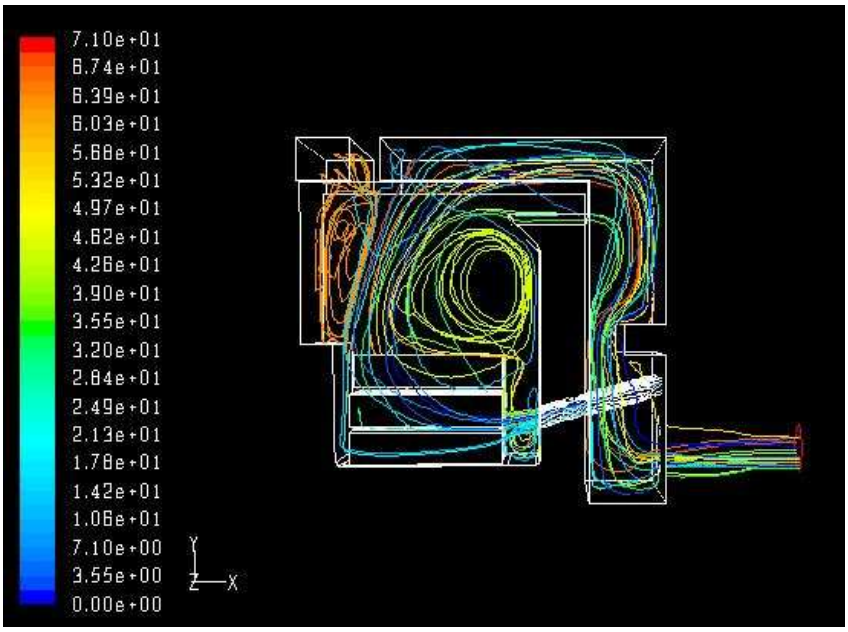

Figure 4.31: Pathlines for Run 9

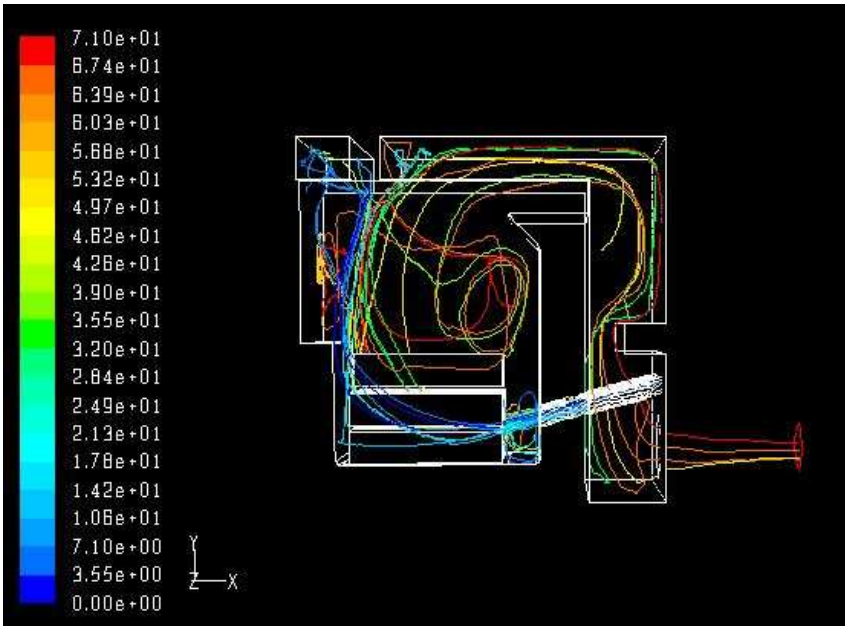

The degree in which flow field is filtered per equations 2.55 and 2.56, the subgrid filter length, is shown on a midpoint contour in Figure 4.32. This length represents the smallest length scale of the resolved eddies, those smaller are modeled. Not surprisingly, the largest resolved eddies occur within the 'dead zone', with large eddies also resolved within the firebox and the stack entrance region. The scale is inches rather than meters due to the scaling of the grid. While LES is computationally expensive, filtering provides resources only where they are needed.

Figure 4.32: Run 9 Z-dir Contour of Subgrid Filter Length [in]

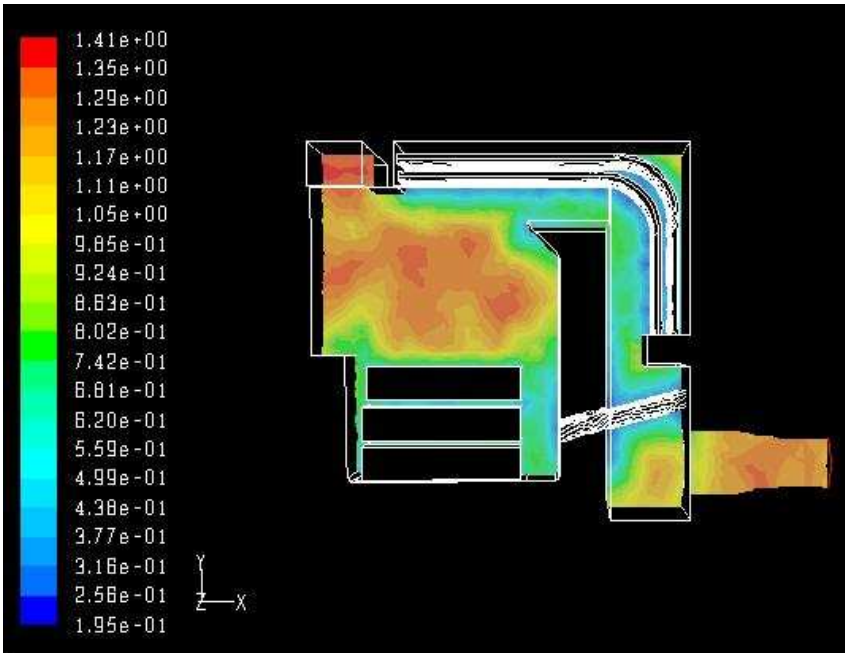

The goal of this exercise is not to identify which simulation is best suited to create a comprehensive model of the OWHH from which to draw specific data points, rather it is to determine which model provides the best platform from which to explore the relative success of an operational or physical modification strategy with respect to PM formation. Additionally, it is important to select a modeling technique that requires the least amount of assumptions, while providing reasonably accurate results at a low computational cost. Overall, all models showed good agreement with measured data with a marked tendency to overestimate firebox temperatures, and thus combustion efficiencies. This caused gross underestimations of CO emissions, with best agreement seen from modeling scenarios which CO is one of the major species in the modeled fuel mixture. The steady state equilibrium based mixture fraction model provided reasonable solutions at a low computational cost, however transient finite rate/eddy dissipation models provided better agreement with internal temperatures. Summaries of the relative pros and cons of each scenario are outlined in Table 4.2.

As evident by measured stack concentrations of O_2 and CO, previous stoichiometric analysis, simulated fuel species emissions, and simulation results indicating chemistry-limited combustion, the primary issue at hand is to reach or surpass a system-wide stoichiometric

air-to-fuel ratio. Additionally, it is much simpler to simulate and test the effects of changed operation rather than physical modifications, reaching the proverbial low-hanging fruit. It is known that combustion within the Model 100 is mixing-limited as well, indicated by fuel rich operation with measured exhaust concentrations of O_2, this is to be addressed after the effects of additional firebox air are known.

Table 4.2: Comparative Summary of Benchmark Model Runs

Run (s)	Pros	Cons
1,10	• Quick convergence of 2D domain yielding reasonable agreement with data	• Loss of in-plane gradients • Overestimation of k and ε in 2D • Difficulty in modeling tube bank • Soot modeling proved not useful for this study
2	• Simplicity of single-species fuel yields stable solutions in less time than other 3D runs	• Equilibrium chemistry approach overestimates internal temperatures and CO oxidation
3	• Pyrolysis mechanism models influence of wood surface radiation over fuel emission rate providing more realistic distribution of volatilization	• Requires arbitrary ceiling to prevent runaway • Unstable numerical behavior requires reduced enthalpy under-relaxation factor thus slowing solution greatly • Does not allow for matching of observed to simulated burn rate
4, 5	• Mixture based fuel yields better agreeing exhaust CO concentrations, due to treatment as boundary 'fuel'	• Has drawbacks of run 2 with less experimentally accepted fuel composition and less stable solution
6	• Better agreement with stack temperatures (due to con), therefore there is no clear advantage over runs 4 & 5	• Mixture has low fuel value, causing overestimated stack O_2 concentrations and CO oxidation
7	• Flamelet based look up table allows incorporation of non-equilibrium chemistry with mixture fraction model	• Scalar dissipation rates are low in benchmark flow field, due to combination of low turbulent intensities, fuel rich operation, and poor O_2 distribution, therefore results are similar to that of the equilibrium case at a larger computational cost • Good fit for better defined, higher Re, fuel lean operation
8	• Finite-rate/eddy dissipation combustion captures has best agreement with internal temperature data • Ability to highlight mixing-limited and chemistry-limited regions	• Unsteady simulation requires a much longer simulation without a clear advantage over steady state simulation • O_2 and CO consumption overestimated
9	• LES better capture large scale structures and resulting convective transport than k-ε • Best agreement with measured firebox temperature	• Same cons as run 8 with significantly longer simulation times

Chapter V: Operational Modifications

Throughout the benchmarking analysis and simulation, it was made clear that the low hanging fruit with respect to improving combustion efficiency, thus PM emissions reductions, is to assure the Model 100 operates at a stoichiometric air-to-fuel ratio throughout the peak pyrolysis period, the first 30 minutes of burn. Analytical and simulation tools outlined in the previous chapter allow for predictions to be made about the effects of additional firebox air on the performance of the Model 100. Operationally speaking, there are other methods in which PM emissions maybe be reduced during Method 28 testing, including but not limited to: longer preheat of the OWHH, removal of accumulated PM and creosote on the tube bank surface, use of thoroughly seasoned wood (minimize free water), and so forth. These operational methods mentioned are more superficial and outside of the purpose of this study compared to increased firebox air, and therefore will not be addressed by this section.

While it is simple to isolate the effects of increased air on the peak pyrolysis burn within a simplified analysis or CFD simulation, it is not so easy experimentally. As discussed in Section 2.1.3, the increase in O_2 and the resulting increase in temperature resulting from improved combustion has marked effects on the feedback mechanisms of the first three stages of wood combustion. To minimize such effects, a cordwood rather than cribwood set of test data used for analysis and later experimentation due to its reduced pyrolysis rates.

5.1 Experimental Testing & CFD Simulation

To assess the effects of increased firebox air on the Model 100, experimental testing and CFD simulation are used in conjunction. Simulation allows for identification of whether mixing-limited combustion improves with increased air and testing reveals the effects of added air on burn rate, efficiency, and potential unintended consequences.

5.1.1 Test Method, Simulation Details, and Boundary Conditions

A Douglas Fir cordwood Category 4 Test Method 28 is performed with a variable speed draft induction fan is used to provide additional firebox air. The test was performed

within the requirements of the Test Method, with the exception of the required length of preburn. The off, low, and high fan settings, 0.058, 0.111, and 0.131" H_2O static respectively, are used in succession during the first 45 minutes of the burn. There are marked transient effects and the shifting of wood combustion phases will have an affect on results, however as trends are sought not accurate data points, this is acceptable.

Simulations are performed with the modeling methods of run 1 at peak pyrolysis and with cordwood geometry. As chemistry is assumed to freeze upon heat extraction at the tube bank, the shortcomings of run 1 of overestimating stack temperatures and underestimating the tube bank's effect on the flow field are not important, the dynamics within the firebox are.

The burn rate and thermal boundary conditions are the same as that in the benchmarking simulations and the appropriateness of this decision will be determined after the testing. Approximating the Douglas Fir cordwood per the ultimate analysis in Table 2.1 with a moisture content of 16.6 % on a wet basis, inlet mass fluxes of air are determined for a range of $0.64 \leq \varphi \leq 1.16$, and averaged inlet values for k and ε are determined per Appendix C.

5.1.2 Experimental Testing and Simulation Results

During the test the induction fan was switched from off to low and low to high at the 22nd and 40th minute respectively. Perhaps due to the resolution of measurements and the delay of pyrolysis feedback mechanisms, the effect of the increased firebox air is not discernable on the burn rate, as shown in Figure 5.1 as the total scale reading. The calculated φ, done similarly as in Chapter 4 with measured CO and CO_2 concentrations, registers a slight increase and then sudden increase at the two switches of fan settings seen in the same figure. Firebox and stack temperatures show the same effect as φ, seen in Figure 5.2, with the secondary temperatures presumably lagging due to transient effects of the tube bank surface temperatures on longer time scales. The marked dip and eventual rise in firebox temperatures at the switch to the high setting is likely caused by initial quenching of the flame by increased flow of cold air and higher strain rates. If the wood was not within the preheated refractory, this may have been enough to extinguish combustion permanently. The increase in stack temperatures is not a good sign as it indicates reduced efficiency. The

internal fluid loop does not respond as quickly to the increased heat release as do the gases, resulting in wasted heat released out the stack.

Figure 5.1: Scale Reading and Calculated Phi for Experimental Testing

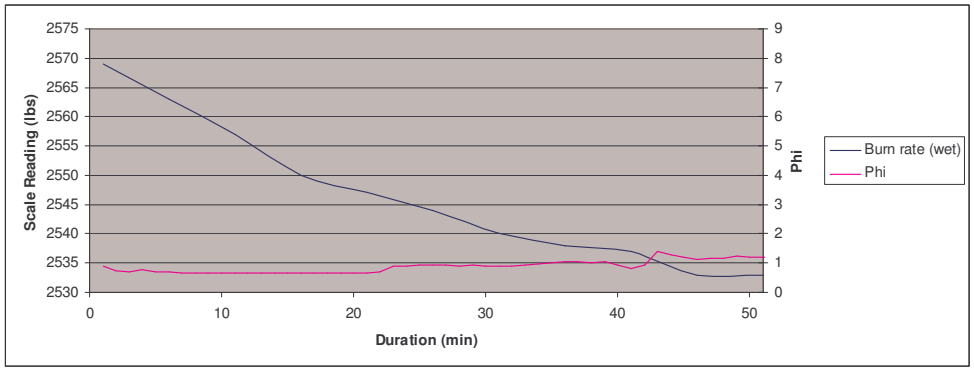

Figure 5.2: Internal Temperatures for Experimental Testing

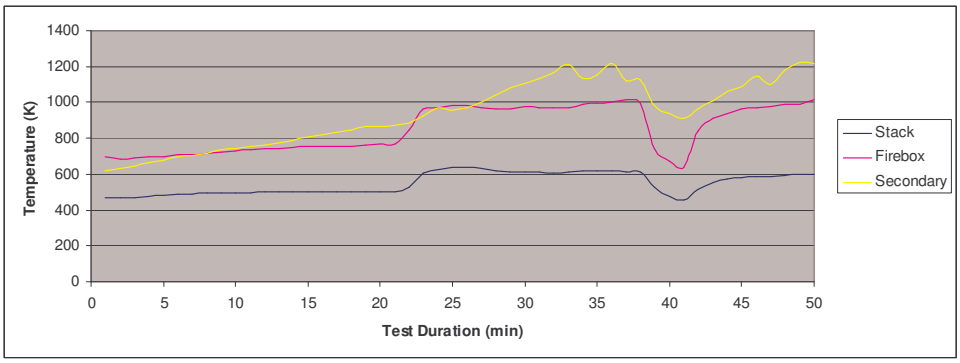

This marked effect is also seen in the measured stack dry concentrations of CO_2 and CO in Figure 5.3. While CO_2 production is less affected by increased firebox O_2, CO oxidation is a useful indicator. While the immediate reduction at the 22nd minute is expected by increased φ and thus temperatures, the spike at the 40th minute provides further support for the temporary extinction theory. As the flame is temporarily quenched near the air inlet ports awaiting re-ignition, the 'fuel' CO released during pre-combustion gas phase pyrolysis escapes and lower post-flame temperatures do not oxidize CO as efficiently. The temperature sensitivity of CO oxidation is apparent by the wide temperature troughs and the comparatively sharp CO spikes.

Figure 5.3: Dry Gas Mole Fractions of CO_2 and CO for Experimental Testing

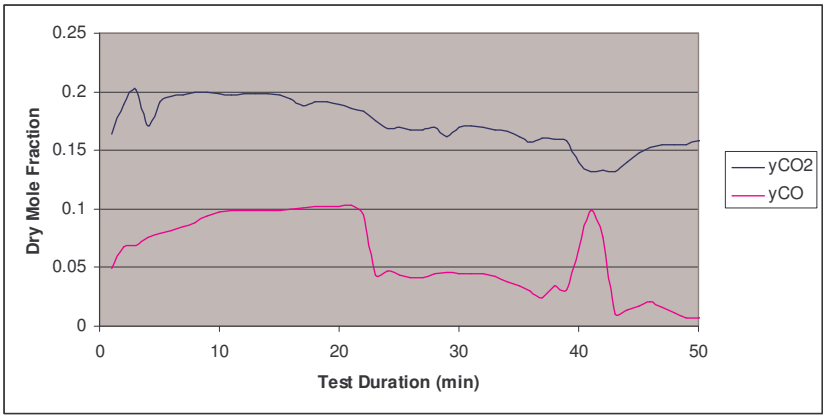

Internal temperatures of eight simulations of increasing φ are compared to points from the experimental data set in Figure 5.4. Rather than time average over data points, instantaneous values of φ calculated from the measured exhaust composition were used. Transient effects are ignored and data points are selected away from changes in fan settings, at the 17th, 28th, 34th, and 48th minute.

Figure 5.4: Internal Temperatures of Experimental Test Data and Simulations vs. Phi

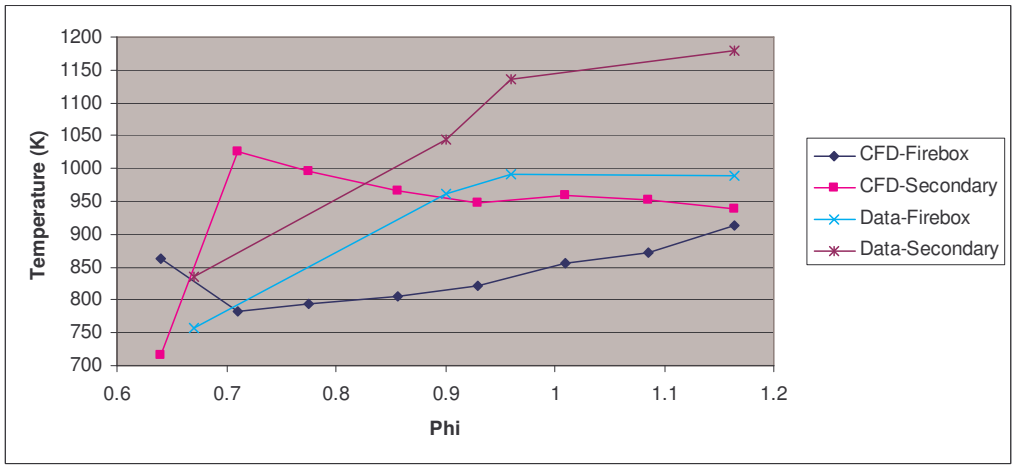

To be expected, the measured firebox temperatures reach a maximum in the vicinity of φ = 1.0, however secondary temperatures continue to increase into lean conditions. This indicates the operation is mixing-limited as well, as the increase in secondary temperatures beyond the stoichiometric air-to-fuel ratio suggests post-flame combustion of fuel-rich

parcels. Simulation firebox temperatures gradually rise with φ, with the exception of φ = 0.64 due to the large scale firebox circulation drawing portions of the exhaust into the thermocouple location. Secondary temperatures do not follow the trend of the test data, as lower values of φ register higher temperatures due to increased circulation due to buoyancy and begin to decrease beyond φ = 1.0 due to cooling of the exhaust by excess air. Indeed, this supports that beyond φ = 1.0, the Model 100 is mixing-limited as the exhaust gases should behave this way if fuel species were not being emitted. These fuel species escaping may be limited to those observed in testing, PM and CO, however it is unlikely based upon benchmark simulation emission of CH_4 and H_2.

While simulation-based internal temperatures suggest O_2-limited combustion, as firebox temperatures rise and secondary temperatures fall beyond φ = 1.0, use of the mixture fraction model can give insight into mixing-limited post-flame behavior. With use of the assumed shape PDF, the variance of Z is a direct indicator of fuel/oxidizer mixing. The larger the variance of a cell, the wider the range of possible stoichiometric compositions as a direct result of poor mixing, be it due to the flow field or gradients of the mixture fraction. To diminish the influence of the latter, a plane is created between the hot water side manifold (0.0 m) to the lip of the air side of the firebox (0.65 m) and is considered the plane just prior to heat extraction. The mixture fraction variance is plotted along this plane in Figure 5.5 for the eight values of φ.

Figure 5.5: Mixture Fraction Variance Along Entrance to Tube Bank

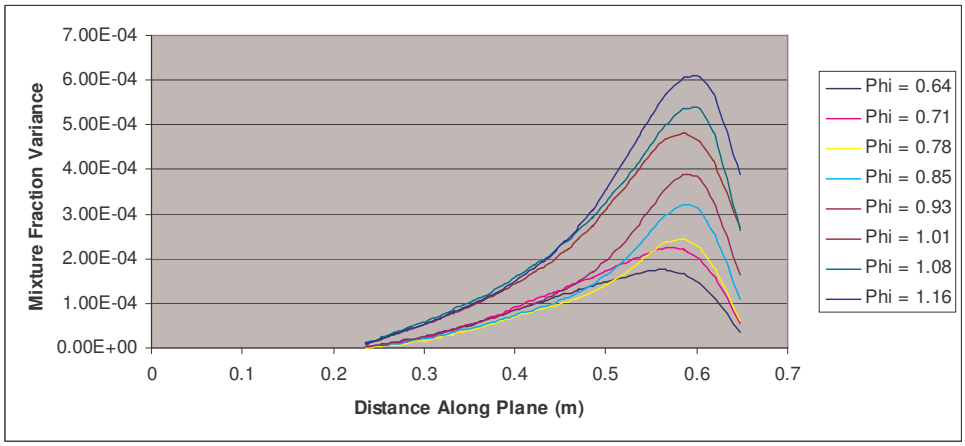

The peak in $Z_{variance}$ is reached in streamlines from the flame tip and steadily increases with air added to the firebox. As the influences of species gradients are minimized at this location, this is considered largely a result of internal geometry and the initial fuel and oxidizer mixing. It is expected that during OWHH operation that as a result of the increased firebox air, solid phase pyrolysis rates increase, creating fuel rich parcels. Mixing is additionally worsened by excessive strain rates as a result of increased buoyancy, that quench lower portions of the flame.

5.2 Certified Test Results and Analysis

After it was demonstrated that $\varphi = 1.0$ and above could be reached with the installed draft induced fan, it was set on high and a full Method 28 test was performed with Douglas Fir cordwood. All four categories of burn were performed, however only the results of the Category 4 are of interest for this study, as it is what analysis and simulations are based upon.

Figure 5.6: Internal Temperatures for Certified Testing

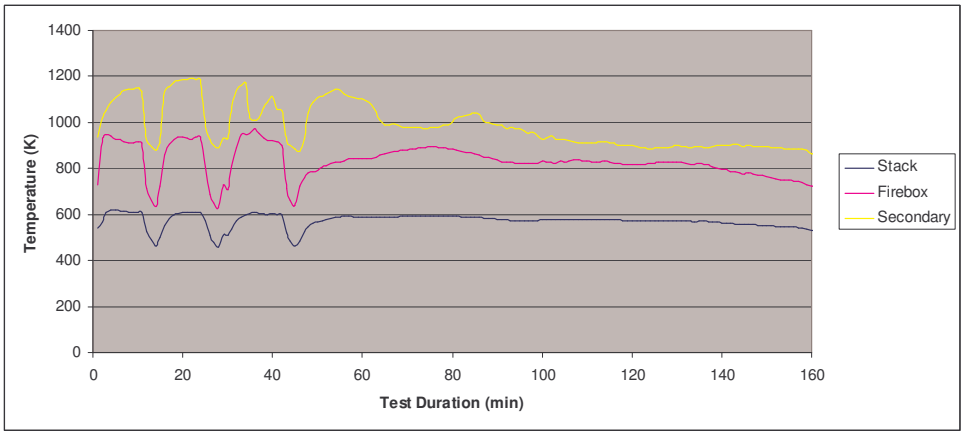

As anticipated by experimental testing, Figure 5.6 shows the increased internal temperatures, with the three troughs due to damper activation. The stack temperature remained around 600 K for the majority of the burn, at the same plateau it reached in Figure 5.2. With negligible skin losses, calculated per Figure 4.10, the efficiency of heat extraction will have to be addressed and the burn rate subsequently reduced.

Figure 5.7: Dry Gas Mole Fractions of CO_2 and CO and Phi for Certified Testing

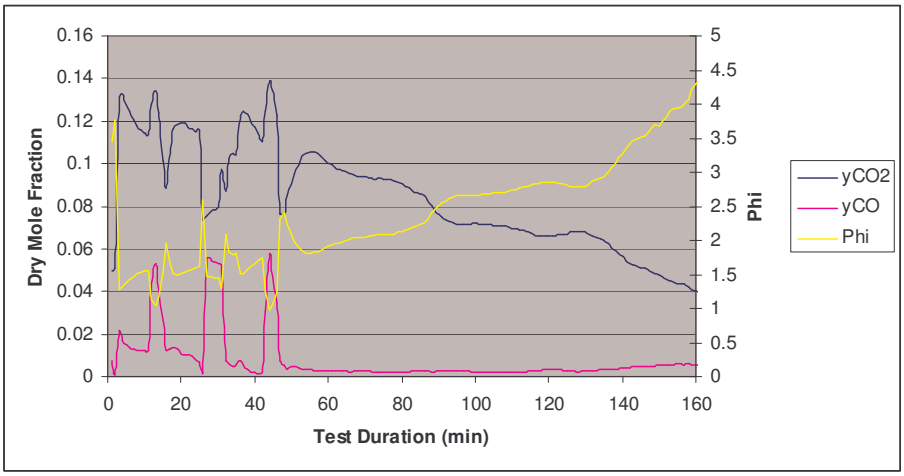

Seen in Figure 5.7, with the increased firebox O_2, CO oxidation improved greatly when compared to the benchmark crib and experimental testing, Figures 4.3 and 5.3 respectively. Additionally, stoichiometric analysis per Appendix A indicates $\varphi > 1.0$ for the duration of the burn, with the exception of the 44th minute due to the damper activation. CO_2 dry mole fractions are lower by over 5% on average, with the assumption of minimal stack fuel species emissions, indicates excess air operation as well. While temporally spaced PM sampling was not performed as it was in benchmark testing, test-wide PM emissions improved from 0.3 lb PM/MMBtu input to 0.213 lb PM/MMBtu input, based upon a previous cordwood certified Category 4 Method 28 test. It should be noted that the aforementioned previous test was 290 minutes, showing a marked increase in burn rate.

Figure 5.8: Calculated and Measured Heat Transfer to Internal Fluid Loop

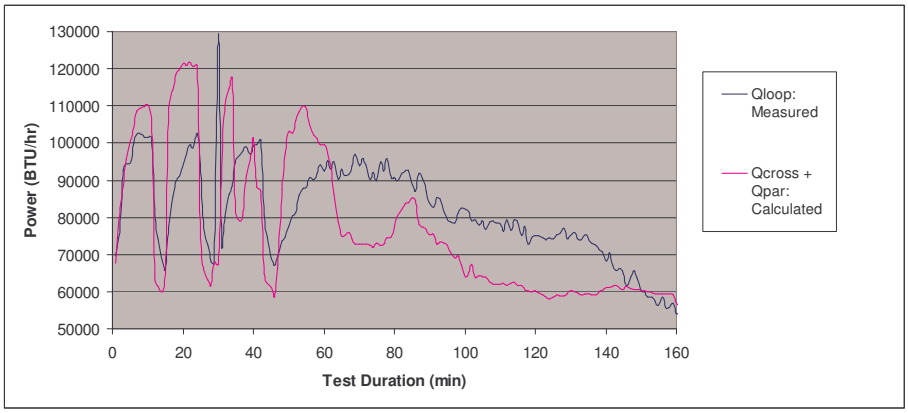

Performing the internal heat transfer analysis of Appendix B continues to provide good agreement with the measured heating output. However it is apparent that the assumptions are not appropriate for use with damper activation, one of several reasons in which Category 4 tests are the focus of this study. The delayed response of the internal fluid loop to exhaust temperature swings could easily be a study of its own. That said, use of this analysis technique will continue.

Figure 5.9: Energy Budget During Certified Testing

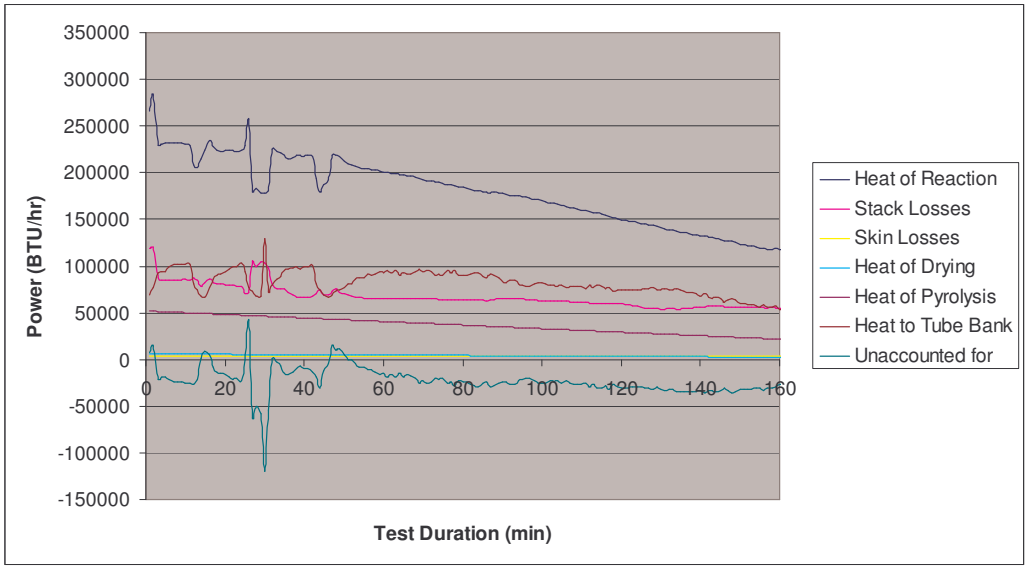

The energy budget analysis of Appendix B seen in Figure 5.9 reveals an improvement in efficiency, as heat to the tube bank, not stack losses, receives the most energy for the majority of the first hour, as opposed to the benchmark testing in Figure 4.10. Despite larger deviation in the 'unaccounted for', indicating an over-allocation of heat, this quantity is only 8.9% of the heat of reaction on average for the first hour. Skin losses and the heat of drying remain negligible compared to other heat flows and sinks.

5.2.1 Subsequent Cribwood Test Results

With hopes of similar results despite known increases in burn rate and the difference between cordwood and cribwood surfaces and surface area-to-volume ratios, full certified Method 28 testing was performed with White Oak cribwood and the high fan setting. For

the Category 4, as expected, temperatures increased with the peak measured 1,280 K in the firebox. Additionally, the calculated φ was above 1.0 for the test duration, as shown in Figure 5.10. Dry mole fractions of CO were reduced by 37.2% and the heating rate to the tube bank was increased by 100.2% on average for the first 30 minutes. However, the burn time was reduced from 150 to 65 minutes and most importantly PM emissions increased, in lb PM/MMBtu input, by 40.4%.

Figure 5.10: Phi During Cribwood Certified Test - Category 4

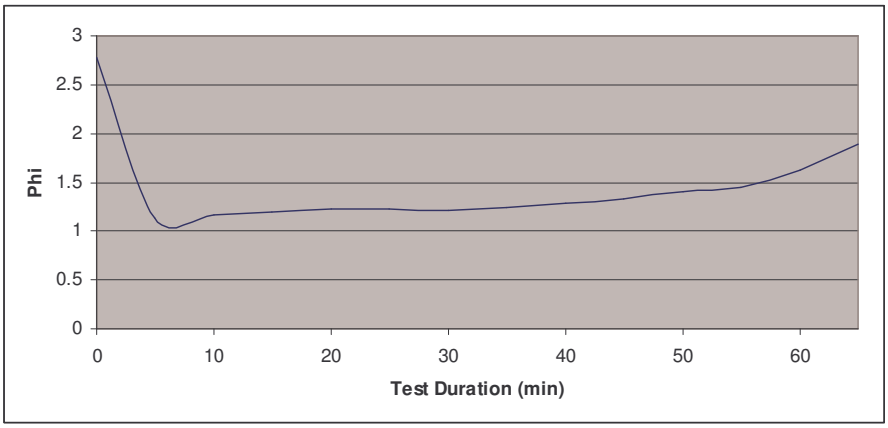

5.3 Operational Modifications Discussion

While it is simple to state that it does not take CFD simulation to conclude that more air introduced into a fuel rich combustion environment will improve efficiency and thus emissions reductions, it is evident that the identification of the Model 100 as also mixing-limited is valuable for future improvements. This is apparent in the success in the cordwood testing, but the failing of the cribwood testing despite consistent φ above 1.0.

Upon determination that the induction fan provided sufficient air to reach stoichiometric conditions, subsequent testing allowed for analysis and suggestions for further improvement, which are as follows:

(1) The observed increases in stack temperature indicate poor efficiency and reductions in burn time are not desirable for consumers. The unit must be 'tuned' such that firebox air is reduced for longer burn times and the tube bank must be redesigned for more efficient heat extraction.

(2) In addition to item 1, the firebox air must be metered to prevent run away solid phase pyrolysis, as seen in the above cribwood test. Without radical redesign of the OWHH overall, this may require staged combustion such that a fuel rich firebox generates steady rates of PM and CO that are later oxidized in a secondary zone.

(3) The increase in secondary temperatures for $\varphi > 1.0$ in cordwood testing suggests mixing-limited reactions despite excess air, providing an opportunity for PM and CO post-flame oxidation via flow obstructions and/or secondary air placement. To accommodate this, the exhaust path out of the firebox must be lengthened.

Chapter VI: Physical Modifications

Addition of firebox air in the previous chapter achieved stoichiometric conditions for the duration of the Category 4 test, however gains made with the cordwood test only. It seems that the current OWHH design cannot be at or above stoichiometric conditions during cribwood testing without drastically increased burn rate and PM emission rates. The combustion field is strongly mixing-limited when $\varphi > 1.0$, and the increased solid phase pyrolysis rates worsen PM emissions. This feedback mechanism exacerbates with increased firebox air, leading to higher firebox temperatures due to complete combustion, which drive pyrolysis rates up and increase buoyancy (superficial velocities), which reduce the residence time of condensed PM between formation and heat extraction.

The loss of efficiency and increased mixing problems can be addressed in tandem by enlarging the post-combustion zone, with a pollution mitigation rather than prevention strategy. This is easier to implement experimentally as well, as it will not require redesign of the firebox. This zone cannot be lengthened without reconsideration of the tube bank, which is an opportunity for gains in efficiency. Upon lengthening of the post-flame path, mixing-limited and/or fuel rich parcels can be oxidized with the use of flow obstructions and secondary air placement respectively. The iterative implementation of physical modifications is to be addressed in this section, with a focus on the cribwood test.

It should be noted that physical modifications are limited to simple add-ons to the existing production unit. Unlike the tube bank, which its redesign allows for post-combustion additions, the exterior shell and the firebox are not to be fundamentally redesigned.

6.1 Analysis of Alternative Designs

With the benchmark and increased air test data along with the analytical tools developed previously, a lot of ground can be covered prior to simulation and experimentation. To facilitate an extended post-combustion zone and the use of flow obstructions and secondary air placement, first the tube bank must be redesigned. Following that, use of different flow obstructions are to be discussed, analysis may be performed on jet

penetration of secondary air into the mean exhaust flow, and the expected CO oxidation may be determined.

6.1.1 Tube Bank Redesign

From the analysis of Appendix B.1 and the resulting Figure 4.8, it is apparent that cross-flow external convective transfer is significantly more efficient than the parallel flow regime, that is estimated as 65.8% of the current design configuration. Taking a second look at the Model 100 geometry, seen in Figure 6.1, it is evident that the current tube bank configuration, especially the parallel flow regime portion, takes up a lot of post-flame space. To lengthen the post-combustion path prior to heat extraction, the feasibility of a completely cross-flow tube bank, perpendicular to the mean flow and placed in the rear of the OWHH near the cold side fluid manifold, will be assessed.

Figure 6.1: Internal Geometry of the Model 100

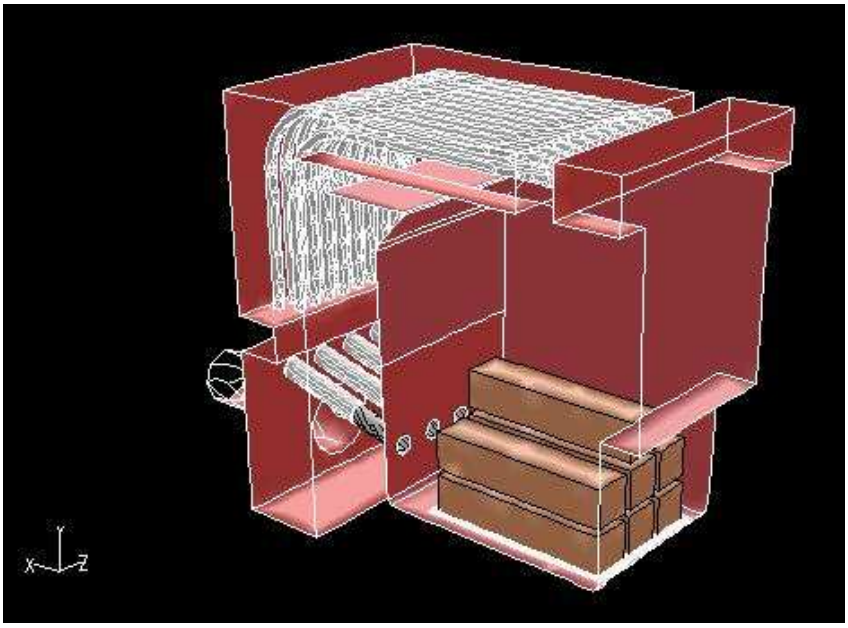

Due to physical restrictions of the exterior shell, the firebox, and required insulation leaving a 5", a bank of three tubes wide (in x-direction) will be examined. While the same outer tube diameters are used, due to the geometric restrictions, the staggering dimensions will be changed from the original tube bank to two diameters apart in the x-direction and

one in the y-direction with the center of the inner staggered tube at the midpoint of the latter dimension. Due to required manifold dimensions, the tube lengths are fixed at 19.5".

The dependency of external surface area on the heat delivered for the entirely cross-flow tube bank will be determined through the analysis of Appendix B.1. Two data points will be used as boundary conditions, the 15th minute of the benchmark and cordwood excess air test. Through the change in the tube arrangement, several factors have changed from previously analysis in the heat transfer calculations which are as follows: equation B.5 results in a factor of 3 rather than 2 for u_{max} and the two preceding constants in equation B.7 are changed to 0.97 and 0.3937 respectively [32]. The calculated heat rate delivered as a function of external surface area is shown in Figure 6.2 for the two data sets, which reported actual heat rate delivery of 61,919 and 65,909 BTU/hr respectively. The Model 100 tube bank has an exterior surface area of 1.976 m^2, set as the upper bound for this study.

Figure 6.2: Heat Rate Delivered to Tube Bank vs. Surface Area

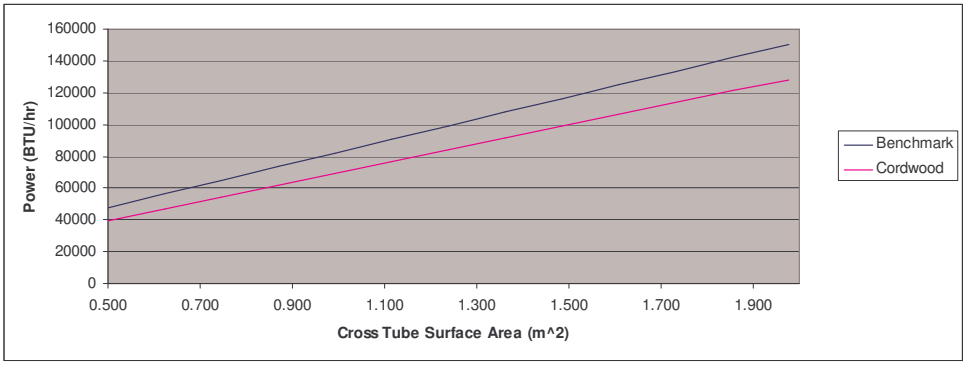

The clearance between the bottom of the cold side manifold and the top surface of the Model 100 is 22.5", which will be used as a limit on the amount of tube rows. With the target heat output at 100,000 BTU/hr for the Category 4, the range between 1.238 m^2 and 1.484 m^2 applies between data points. This is a conservative estimate, allowing for idealizations in output estimation, as the recorded Model 100 outputs at this point were much lower and the target 100,000 BTU/hr is test averaged. These surface areas correspond to roughly 30 and 35 tubes, or 20 and 23 rows. The former configuration fits snugly within the height constraint, however the latter would require a lowering of the air inlets.

Figure 6.3: Photos of Original and Redesigned Tube Banks

Taking into account manufacturing considerations, a tube bank of smaller ¾" outer diameter tubing was used, with 21 rows of 32 tubes total with an external surface area of 1.468 m^2. The original and redesigned tube banks are shown in Figure 6.3. At a reduction in materials, opening of the post-combustion path, and it is expected by conservative estimates that the increase in efficiency will maintain the desired heat output.

6.1.2 Flow Obstructions

A common method of increasing the mixing and encouraging settling of particulates in a flow field is the use of baffles. With the removal of the hot side manifold and overhanging tube bank, a hollow shelf, or 'airbox', is placed directly over the firebox. This allows for a distinct transition between the firebox and the post-combustion zone, the possibility of secondary air injection, and the placement of baffles atop the airbox. This overall configuration is seen in Figure 6.4, one of the modification scenarios tried in this section.

Figure 6.4: Internal Geometry of Airbox and Baffles of Configuration 1

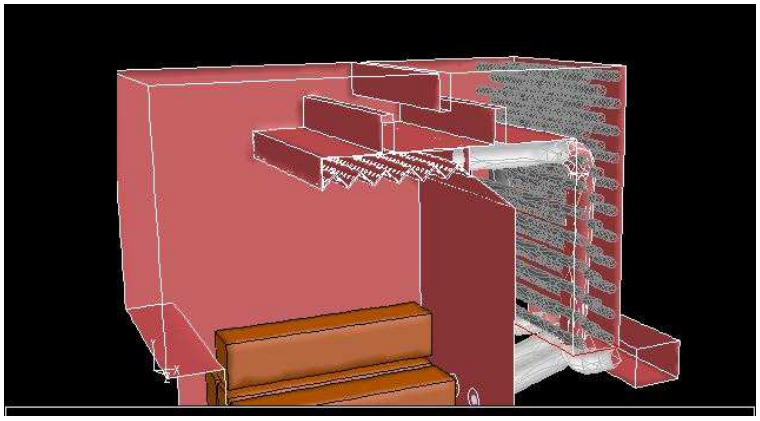

In principle, the baffles aid mixing through increased vorticity and circulation, and they aid PM emissions reductions through impaction upon the surfaces, via departure from mean flow pathlines and maximizing particle residence times in the hot oxidizing post-combustion environment. While these physical modifications require the use of an air inlet blower, sized at 216 cfm at 0" WC static pressure, baffle configurations should be considered with a minimal pressure drop in mind. Two styles of baffles are considered, vertically oriented as seen in Figure 6.4 and horizontally oriented similar to an impaction style particulate separator. The experimental baffles used are made of vermiculite.

6.1.3 Secondary Air Jet Penetration

The establishment of a distinct post-combustion region allows for staged combustion, reducing firebox air to below $\varphi = 1.0$ to prevent excessive solid phase pyrolysis and introducing secondary air later to fuel lean conditions, that is $\varphi > 1.0$ for the system. The two methods of secondary air placement tried are overfire air, injection from a serrated grate above the flame from the airbox seen in Figure 6.4, and post-combustion jets.

For the use of secondary air jets, penetration into the mean flow is crucial, otherwise the secondary air and the fuel rich post-combustion gases will be stratified. Used in the study of coal-fired boilers, equation 6.1 provides an estimate of the jet penetration based upon the cross-wise mean flow velocity, jet exit velocity, and the jet diameter [19]. One jet configuration used is jets on vertical face of the airbox end penetrating into the plane between the firebox and entrance into the post-combustion zone.

$$\frac{z}{d_o} = \left(\frac{V_{cross}}{V_{jet}}\right)^{2.24} \left(\frac{x}{d_o}\right)^{2.63} \qquad \text{Equation 6.1}$$

Using the average exhaust flow from benchmark testing during peak pyrolysis and the cross-sectional area of this vertical plane, the cross-wise mean flow velocity is 0.967 m/s. With a jet diameter of 3/8" and equation 6.1, Figure 6.5 is shown with distances in inches. The axial distance is from the jet exit (0.0") to the front wall (17.5"). From the jet exit center to the ceiling is a height of roughly 8", with which it is expected that the jet will have to reach the front wall in half that distance, suggesting a minimum required jet exit velocity of 32 m/s.

Figure 6.5: Jet Penetration For Various Exit Velocities

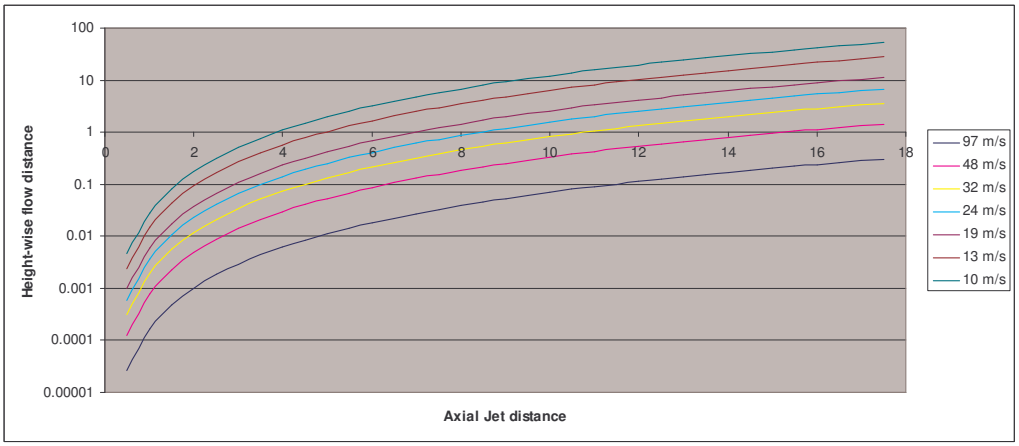

6.1.4 CO Oxidation

Cordwood and cribwood testing showed reductions in CO emissions upon increases in φ, however the overestimation of CO oxidation within simulations can be anticipated. As a supplement to the simulation results, the goal is to get an approximate idea of the post-combustion temperatures required to sustain CO oxidation.

For a given local temperature, H_2O, and O_2 concentrations, equation 4.6 is integrated to derive the rate of CO consumption as a function of time. The consumption is determined as a reduction by a factor of 10, which covers the range from peak pyrolysis to

the char oxidation dominated stage during benchmark testing. As this mechanism is not useful in fuel-rich environments, the data for temperatures and species concentrations are from the $\varphi > 1.0$ cordwood test on the Model 100. Save for the damper event, the peak CO production is assumed as from the 5th to 25th minute. As the chemistry assumed to freeze upon heat extraction, the species mole fractions measured at the stack are approximated as equal to those at the firebox exit plane.

As seen with the PM oxidation analysis, CO oxidation rates are heavily temperature dependent seen in Figure 6.6. Plotted for each minute of the test data set is the residence time at a given temperature required to reduce CO concentrations by a factor of 10. With the advent of the airbox, the center pathline of an unobstructed fluid parcel of 0.88 m with a mean flow velocity of 0.967 m/s used previously resides approximately 0.91 s in the post-combustion zone. For reference, the average dry gas mole fraction of O_2 for this data set is 0.0752. As a rule of thumb, temperatures below 850 K are considered not conducive for CO oxidation.

Figure 6.6: Time to Oxidize CO by Order of Magnitude

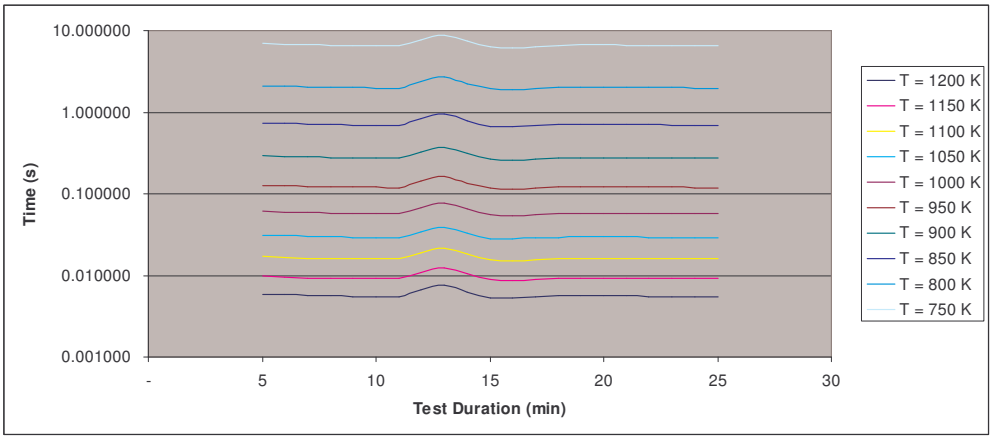

6.2 CFD Simulation of Redesigned Geometries

With the redesign of the new tube bank, the post-combustion zone is lengthened giving an opportunity for simulation and testing of many permutations of airbox designs, baffle configurations, and secondary air placement. Additionally, the clear distinction

between the firebox and post-combustion zone allows for a staged combustion with a firebox operating fuel rich, preventing the results of Section 5.2.1 testing.

As this portion of the study went on, measurement techniques became more sophisticated and physical modifications became more complex. With goals beyond that of this particular study, validation testing was not restricted to Category 4 cribwood tests. Three configurations will be examined for brevity, which are illustrative towards the mechanisms discussed previously and reveal different simulation behavior than of that seen in benchmarking analysis. These redesigns require the use of a blower at the air inlet(s) sized at 216 cfm at 0" WC static pressure.

6.2.1 Outline of Experimental Geometries and Preliminary Simulation

Throughout this section, the three configurations are referred by number, increasing in chronology of experimentation. Considering the problems that arose out of the firebox stoichiometry of $\varphi > 1.0$ during cribwood tests, the first task is to split the inlet air into firebox and secondary air. The outer two firebox inlet ports are plugged and tubing extends the air up to the airbox inlets. During initial experimental testing, the firebox and airbox inlets shared a common blower as was the case in configuration 1. Later, for testing of configurations 2 and 3, dedicated firebox and airbox blowers were installed, allowing for a known split of air injection. In addition to splitting the inlet air, with the intent of a production OWHH with only one blower, the two firebox inlet ports were reduced in diameter on the burn side from 2" to 1" in configuration 1, and to ¾" in configurations 2 and 3. Along with the use of the redesigned tube bank seen in Figure 6.3, these are the commonalities between the three experimental geometries.

6.2.1.1 Secondary Air Placement

With the opening of post-combustion volume originally taken up by the hot side manifold and tube bank, the use of an airbox as seen in Figure 6.4 offers three advantages: placement of a shelf over the flames creates a longer exhaust path for post-combustion CO and PM oxidation, diverting firebox air to the hollow airbox allows for secondary air injection, and the top of the airbox may support flow obstructions such as baffles. The

three configurations studied vary by their placement of secondary air. Configurations 1 injects the secondary air down upon the flame through a serrated grate shown in Figure 6.3, with the intent of disrupting the mean flow with quick post-flame oxidization of PM and CO. Configuration 2 injects air through 5 3/8" jets spaced along the vertical face of the airbox, as discussed in Section 6.1.3. Rather than run the risk of quenching post-flame reactions as in configuration 1, these jets will introduce air at the boundary between the firebox and post-combustion zone with sufficient momentum to penetrate the mean flow. Configuration 3 injects air from the top side of the airbox through 14 3/8" jets placed in gaps between the baffles, to be discussed in the following section.

6.2.1.2 Baffle Design

The two baffle configurations, commonly seen use in industrial dust control devices, are gate style (vertically oriented) and impaction style (horizontally oriented) baffles. With each come their advantages and disadvantages, impaction style baffles have a higher pressure drop, however gate style baffles would not improve lateral mixing as well [14].

For the gate style baffles, flow visualization can be used to quickly evaluate baffle configuration options without the need for time-consuming experiments. Three baffles were selected as a compromise between enhancing mixing and adding hardware. The goal is to determine the configuration that maximizes particle residence times, via departure from mean flow pathlines, while minimizing the total pressure drop.

Figure 6.7: Pathlines & Particle Trajectories for Flush (Top) & Non-flush (Bottom) Gate Style Baffles

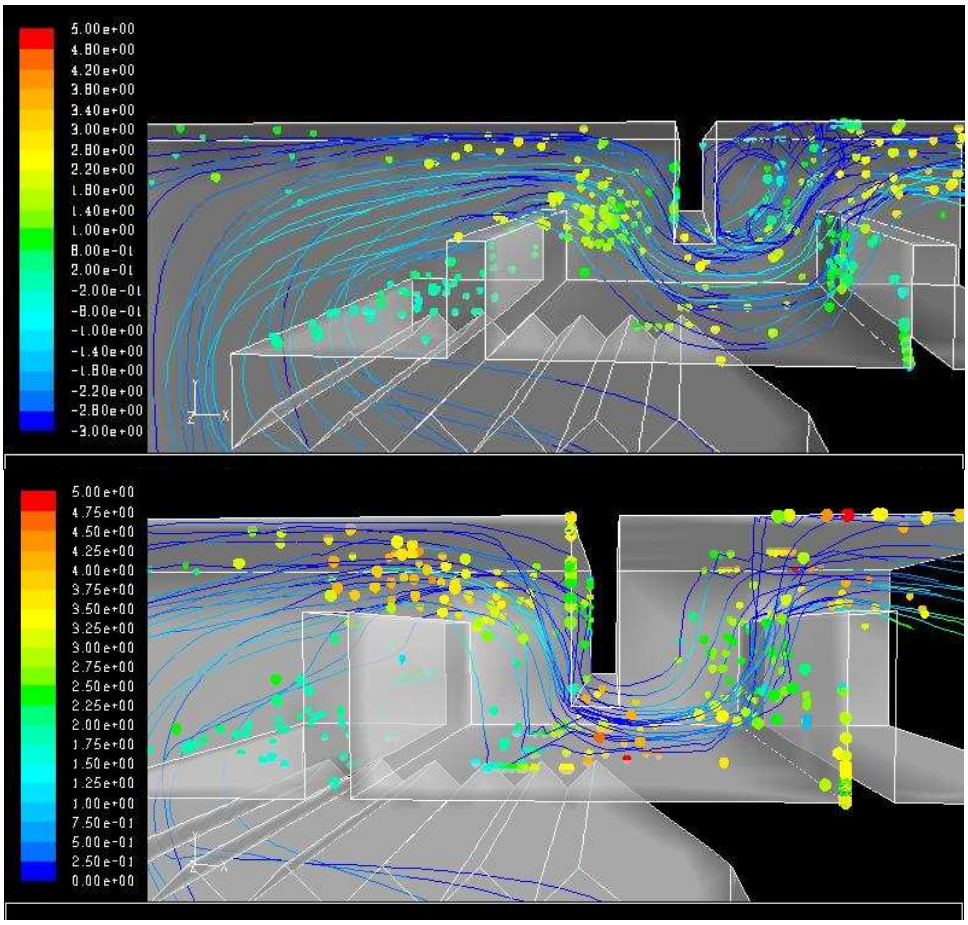

A non-reacting simulation is performed for various configurations, with air at typical exhaust mass flow rate of 0.1 kg/s observed during experiments with the blower, laden with inert 1 μm particles of density 1,500 kg/m^3. While there was little difference between configurations of up-down-up or vice versa, Figure 6.7 illustrates the difference between baffles that extend 1" into and that are flush with the vertical midpoint of the flow path. The figure shows the pathlines of the flow field as solid lines colored by velocity magnitude and the particle positions, exaggerated in size for clarity and colored by x-velocity, after 10 s of time-stepping. Note that the both graphics are scaled such that the particles are colored by the upper scale and the pathline velocity magnitudes are colored by the lower scale. Lower x-velocities of the particles and locations outside of pathlines, including wall impaction, are desired. There is little distinction between the two configurations with

respect to dispersion of particles outside of the mean flow pathlines, however the non-flush baffles exhibit the tendency of pathline compression and stratification past the baffle tip. This increases particle x-velocities, thus reducing residence times, and reduces circulation zones that entrain particles as seen after the second flush baffle. Additionally, the non-flush baffles have a pressure drop of 0.096" WC greater than the flush baffles. Therefore the flush baffles were selected for implementation.

Five rows of impaction style baffles were selected, with the configuration seen in Figure 6.8. As was the case with the gate style baffles, dimensions were limited by available materials. While CFD simulation could be used to optimize the spacing and/or the gap width of this configuration, this impaction style configuration was used in conjunction with secondary air jets within the gap spacing. Convective mixing scales with the square of the characteristic length, thus these gaps of smaller cross sectional area than the gate style offered a clear opportunity.

Figure 6.8: Rendering of Impaction Style Baffle Configuration

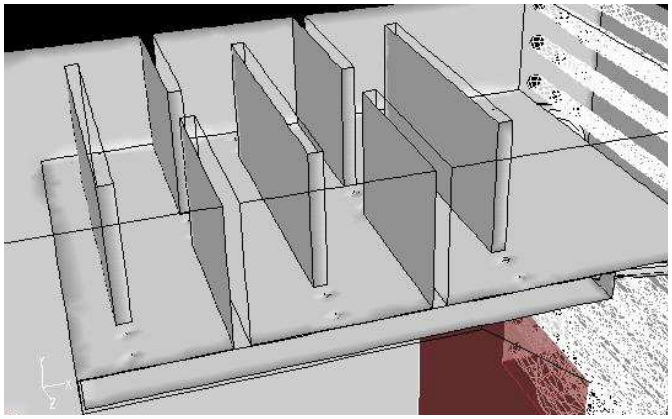

Like that in configuration 2, secondary air injection through these gaps in configuration 3 must be optimized for maximum penetration at minimum pressure drop. The jet penetration analysis is not appropriate in this context, due to the high degree of vorticity between these baffle gates preventing an accurate assessment of the 'mean flow', the calculations will provide gross overestimates of the needed penetration velocity. Additionally, the mixing induced by these baffles will aid in vertical transport of injected air beyond that of the jet momentum. That said, the advantage of two 3/8" diameter jets versus one 1/2" diameter jet is determined. Cold flow simulations with airbox and firebox

inlet conditions of 98 and 58 cfm respectively are performed, and two jets versus one jet results in a decrease in average jet static pressure drop by a 16.6% and in average jet face velocity by 11.7%. As it should be noted that the differences in static pressures is 1.1 kPa as opposed to 10 m/s, the dual jet configuration is selected. It offers higher jet velocities at a reasonable cost of pressure drop.

6.2.2 Simulation Setup and Results

In all three configurations, the firebox air is reduced through diversion to the airbox and use of smaller firebox port diameters, however in the cases of configurations 1 and 2, firebox temperatures may rise as a result of near post-flame combustion and induce pyrolysis rates similar to those seen in the previous cribwood test.. It should be noted that between the $\varphi > 1.0$ cribwood test and the benchmarked test was only a difference in the test averaged mass flux of air by 20.7% as calculated by equation B.3 and the observed burn rate, indicating the nonlinear response of the system to increased firebox air. That said, the simulations are run with a burn rate, $\dot{m}_{wet}$, of 0.0101 kg/s with the benchmark fuel load moisture content, corresponding to that of the $\varphi > 1.0$ cribwood test. As was the case with operation modification simulations, raw data points are not as important as observed trends, especially with pre-test simulation. Therefore, these configurations will use this maximum pyrolysis rate to simulate the worst-case-scenario. Mass fluxes of inlet air for configuration 1 to the airbox and firebox combined is 120 cfm, based upon the blower capacity and the measured static pressure of the cold OWHH. The mass fluxes of the airbox and firebox are 70 cfm and 60 cfm respectively for configurations 2 and 3, similarly based upon preliminary cold measurements. The airbox and firebox were not equipped with dedicated blowers and orifice meters until after the testing of configuration 1. Turbulent parameters are calculated per Appendix C as done previously.

Full reacting simulations will be run using the methodology of run 8, due to the accuracy with respect to internal temperatures and the ability to distinguish between chemistry-limited and mixing-limited regimes. While LES provided the best agreement with internal temperatures during benchmark simulations, the computational cost is prohibitive. Due secondary air injection from small ports in the post-combustion zone, a much more

refined grid in these regions than was required by Model 100 simulations. Configurations 1, 2, and 3 had grids consisting of 252,696, 138,116, and 190,643 cells respectively, with a direct correlation between grid size and the amount of secondary air injection ports. Without use of PM formation and oxidation modeling and in anticipation of overestimated CO oxidation based upon fuel-rich benchmark simulation results, the minimum temperatures required for oxidation determined in sections 4.2.3 and 6.1.4 in these fuel lean simulations, placing further requirement on effective internal temperature modeling. Due to the volume of those produced, many graphics from these simulations not placed within this chapter are in Appendix D. Those referred to in the text are included, however additional context for determinations and discussions are provided by these omitted graphics.

Internal temperatures and dry gas stack species mole fractions for the three configurations are shown in Figures 6.9 and 6.10 respectively. As with all the 3D simulations and tests in this study, the temperatures reported are averages of two thermocouples within the same z-direction plane. With respect to data sampling and previous results, the 'Baffle In' thermocouple is the same location as the 'Secondary' location and the 'Baffle Out' thermocouple, recording the temperature prior to heat extraction by the redesigned tube bank, is located per Figure 3.3.

Figure 6.9: Internal Temperatures for Simulations of Physical Modifications

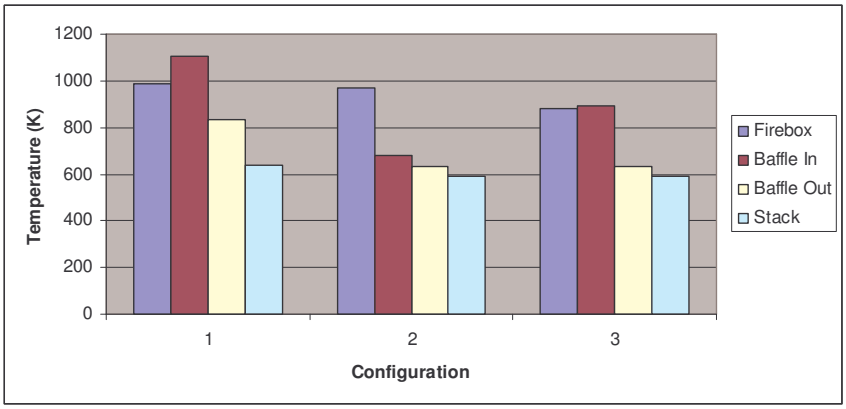

The placement of the secondary air is of critical importance with respect to simulated internal temperatures, which in turn drive chemistry-limited reactions. Configurations 1 and 2, due to air injection onto and across the opening of the firebox respectively, have much larger firebox temperatures than that of configuration 3, which

operates effectively fuel-rich until the post-combustion zone. Now that secondary air injection is employed with enhanced mixing via baffles, high firebox temperatures are not necessarily a good thing. So called runaway pyrolysis, seen in the $\varphi > 1.0$ cribwood test with a measured peak temperature was 1,280 K, is not likely to occur with any of these configurations. Baffle In temperatures are lower than that measured or simulated during benchmarking. With respect to PM oxidation seen in Figure 4.11, configuration 2 is below the upper limit for significant reductions of 773 K. The advantage of higher O_2 concentrations in the post-combustion zone by these configurations is minimal for these lower temperatures. Stack concentrations are a sufficient gauge for this analysis; as O_2 mole fractions upon entrance to the baffles on to the stack vary little for configuration 2 due to the large focused secondary air delivery and its diluting effects. Baffle In temperatures rise from firebox temperatures in configurations 1 and 3 indicating post-combustion reactions, however reduce at the Baffle Out location largely due to dilution as well. It may be inferred from temperatures alone that the secondary air injected in all three configurations is excessive to the point of detrimental dilution, however the overestimation of simulation techniques on CO oxidation suggests an experimental determination on the exact appropriate amount of secondary air to be injected. Stack temperatures show relative agreement, however as with operation modifications modeling these simulations are primarily concerned with the domain up until heat extraction.

Figure 6.10: Dry Gas Mole Fractions for Simulations of Physical Modifications

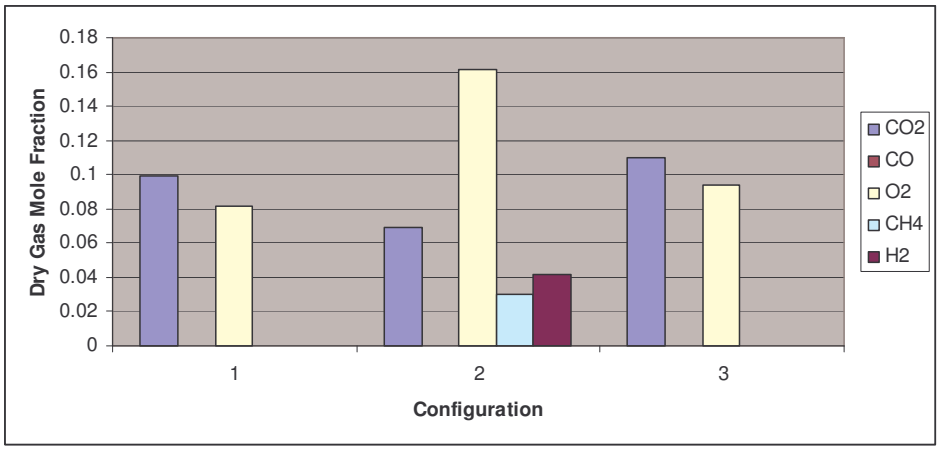

The diluting effect of the secondary air is also seen in Figure 6.10, as CO_2 mole fractions have more than halved and the system runs with significant excess O_2. Most interesting is the large O_2 concentration in configuration 2, presumably due to the same concentrated dilution effect seen with Baffle In temperatures. The fast reduction in temperatures at the firebox-Baffle In interface quenches combustion with subsequent mixing and temperatures comparable to configuration 3 unable to provide the activation energy, indicated by large stack O_2 and fuel species concentrations. While unsurprising that CO oxidation was overestimated by runs 1 and 3, it is noticeable that the forward reaction 4 was sufficient to consume CO but the fuel species were not in an oxygen rich environment. All else being equal, configurations 1 and 3 should report the same stack concentrations of CO_2 and O_2, however it should be noted that these are vertex averages of the domain outlet for which configuration has almost an order of magnitude between the vertex maximum and minimum O_2 mole fraction. Based upon these results, the configuration 2 method of air injection is the least successful of maintaining high post-combustion temperatures.

To determine the performance of each baffle configuration, in the absence of a mixture fraction variance, eddy mixing time scale, k/ε, will be used as a metric of turbulent mixing. As outlined in Chapter 2, the eddy dissipation model postulates that reaction rate kinetics is inversely proportional to this time scale, k/ε. The inverse of this time scale, the dissipation rate, is plotted on midpoint lines along the z-direction at the entrance to the baffles and tube bank, with a reference from run 8 of the benchmark simulations using a height-wise midpoint. The comparison between the three configurations before and after the baffles and the benchmark case at the plane prior to heat extraction is shown in Figure 6.11.

Figure 6.11: Eddy Dissipation Rates for Physical Modifications & Benchmark Run

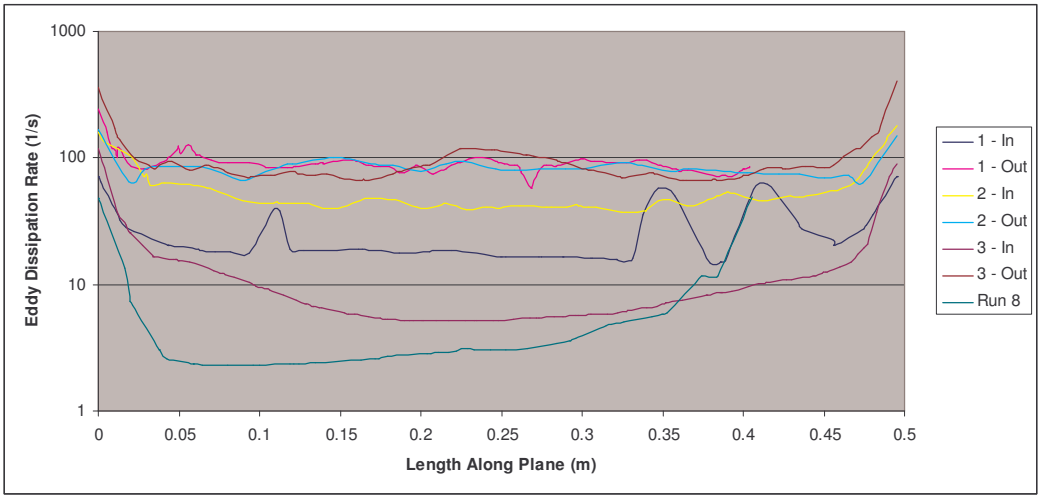

The greatest gain in turbulent mixing, by use of this metric, is configuration 3. Comparing the mixing gains of configurations 1 and 2, for the same gate style configuration, indicates the advantage of post-combustion reactions as well. The gain is small for configuration 2, however the magnitude is higher than that of the benchmark case due to the secondary air jet penetration near the Baffle In location. Overall, use of baffles has a clear advantage in turbulent mixing, with the impaction style baffles providing the largest gain in mixing and maximum eddy dissipation rates.

6.3 Experimental Test Results and Analysis

There were several experimental parameters that did not match those anticipated during simulation, as to be expected. The actual inlet air for configuration 1 was 82 cfm compared to 120 cfm modeled. The airbox and firebox inlet air for configurations 2 and 3 were 58 cfm/71 cfm and 65 cfm/71 cfm respectively compared to the 60 cfm/70 cfm modeled. Due to a temporary scarcity of cribwood pieces of the required length, to match typical fuel loads of between 60 – 68 lbs (wet), 8 16" long 4 x 4 pieces rather than the typical 7 20" long 4 x 4 pieces were used during the configuration 3 test.

While interesting for comparisons of simulations, the test data of configuration 1 is sparse due to limited measurement equipment at the time, therefore much of this section will concern the results from configuration 2 and 3 testing. Internal temperatures and dry gas

stack species were not measured for the configuration 1 test. Figures 6.12 and 6.13 display the measured quantities for all three configurations, the heat output as calculated per equation B.25, and the stack temperatures respectively. The longer burn rate coupled with significantly lower stack temperatures of configuration 3 versus 1 indicates gains in efficiency despite comparable heat output rates. It should also be noted that the redesigned tube bank does not have a problem reaching the target of 100,000 BTU/hr.

Several items predicted by simulation stand out. The dilution effects seen during configuration 2 simulation appear to have affected the system efficiency while maintaining high stack temperatures. The burn rates, seen as the test durations, are in order of decreasing predicted firebox temperature. Configuration 3, with fuel-rich firebox operation, has the longest burn rate.

Figure 6.12: Heat Output to Internal Loop for Physical Modifications Testing

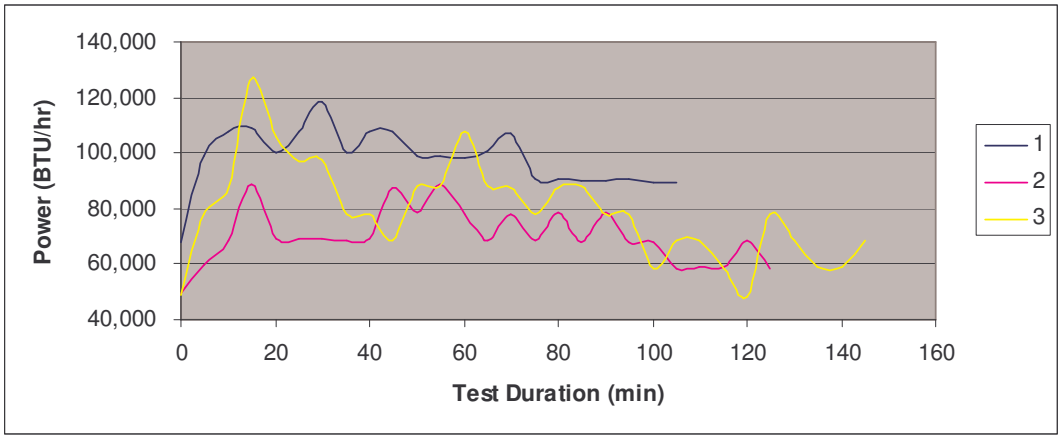

Figure 6.13: Stack Temperatures for Physical Modifications Testing

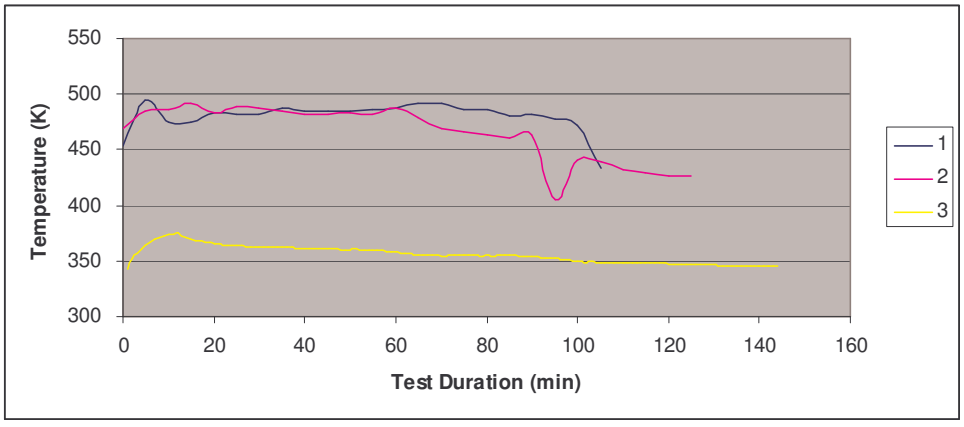

Internal temperatures recorded for the first hour of configurations 2 and 3 are shown in Figure 6.14 and it is evident that the simulations tended to underestimate temperatures. This could be one of many reasons: direct CO oxidation in the simulation takes place only in the vicinity of the cribwood whereas it is likely to occur strictly in the post-combustion region as it is a gas phase pyrolysis product that may not form until outside of the firebox, internal surface temperature boundary conditions were based upon benchmarked test data and this assumption may be inappropriate, and that exothermic PM oxidation in the post-combustion zone is not modeled but may be significant in is region as evident by the highest temperatures recorded in the Baffle Out region. These high Baffle Out temperatures in configuration 3 with the reduced stack temperatures are again a testament to its efficiency and rule out the possibility of reduced stack temperatures primarily via dilution.

Figure 6.14: Internal Temperatures of Configurations 2 and 3

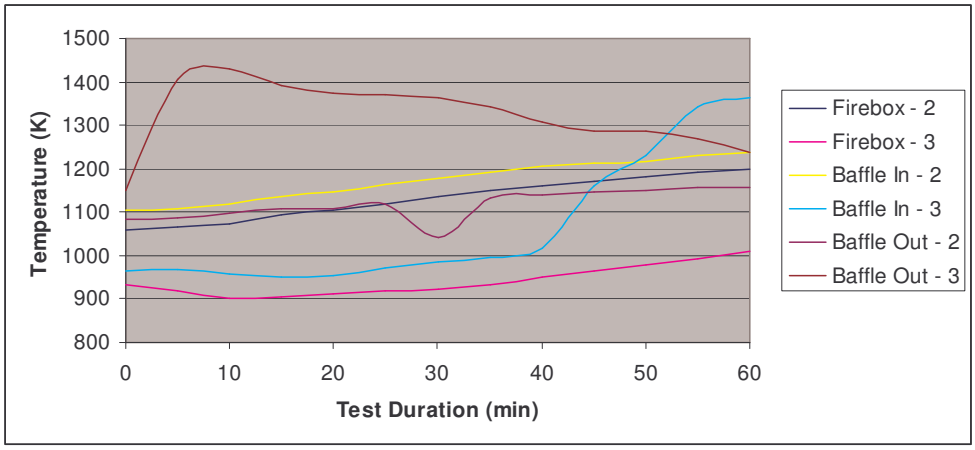

The equipment used during experimental testing measured O_2 and CO directly, rather than CO and CO_2 as done during certified testing. The dry gas stack mole fractions are shown in Figure 6.15 for configurations 2 and 3. Stack O_2 concentrations for configuration 3 are much higher than simulated expectations. This may be due to the overestimated burn rate of the simulation, based upon the so called runaway pyrolysis test as a worst case scenario, thus overestimating the CO_2 concentrations. This is a likely explanation, as the 5th to 25th minute average wet burn rate of the test compared to the simulation is 0.00755 kg/s to 0.0101 kg/s in a simulation that produced trace CO. Measured

CO reduced greatly between configurations 2 and 3, anticipated by simulated high Baffle In temperatures despite overall underestimation of measured internal temperatures.

Figure 6.15: Dry Gas Mole Fractions of CO and O_2 from Testing

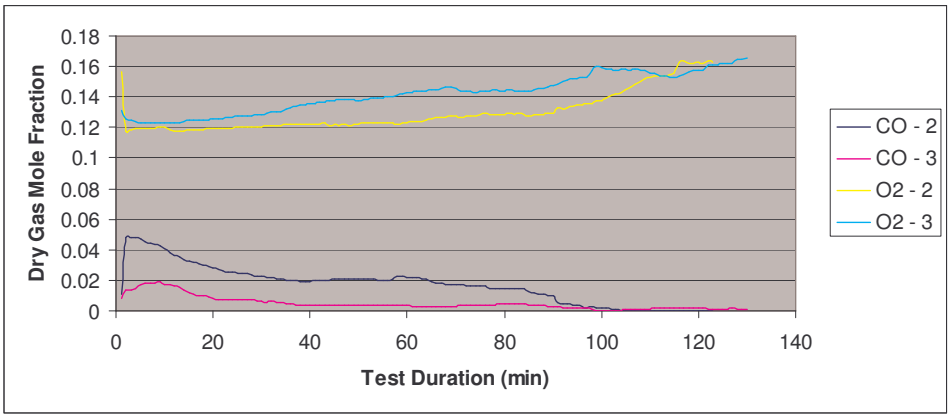

Through the stoichiometric analysis of Appendix A of these two data sets, the system-wide φ is calculated and shown in Figure 6.16 out to the 110th minute. It is not surprising that both are above φ = 1.0 for the burn duration, however with this analysis the firebox φ can be calculated as well. The 5th to 25th minute averaged value is $\varphi_{firebox} = 1.085$ for configuration 3 and $\varphi_{firebox} = 0.844$ for configuration 2. As desired, configuration 2 achieves true staged combustion, with fuel-rich firebox operation, however the post-combustion mixing is insufficient. The challenge remains to reduce airbox air to an acceptable level, balancing mixing and air injection with overall efficiency.

Figure 6.16: Calculated Phi for Physical Modifications Testing

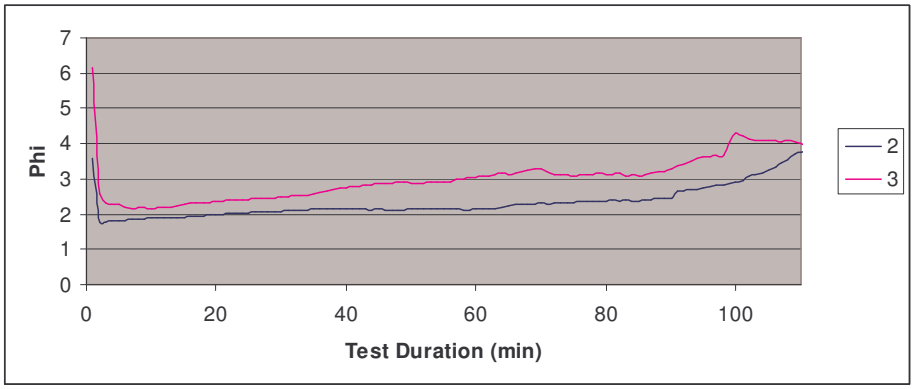

A PM sampling train like that of Test Method 28 was not employed during these experimental tests, thus no measurements of PM emissions were made. The somewhat subjective measured of visual opacity suggests gradual improvement in PM emissions for each configuration. An observed opacity of 0% was recorded for the 30th, 25th, and 15th minute of the configuration 1, 2, and 3 tests respectively.

6.4 Summary of Physical Modifications

The strength of CFD as a design tool lies in its ability to test new ideas involving the experimental configuration or the operating parameters without necessarily running each as a new experiment. By using the model to develop targeted experiments, and then using the results of the experiments to suggest new modeling ideas, we are able to cover much more ground than would be possible using trial and error experiments alone. Likewise, given the complexity of the system the use of only the model, and no experiments, runs the risk of the model not being rooted enough in physical reality to make the results useful for moving ahead. The alternation of experiment and modeling provides the fastest and most accurate means of moving ahead toward the goal of low emissions and high heat recovery efficiency.

The results clearly showed the advantages of an extended post-combustion zone compared to the original design. The new, compact heat exchanger and the addition of the airbox shelf provided many opportunities for enhanced mixing via flow obstructions and staged combustion via secondary air injection. Upon addressing the $\varphi < 1.0$ problem identified in the previous chapter, turbulent mixing was increased through the use of two different baffle styles. The design decisions for the gate and impaction style were dependent on flow field physics and secondary air penetration respectively, and were addressed prior to full simulation with a cold-flow simulation. Full reacting simulation and experimental testing confirmed configuration 3 as the most efficient and CO oxidizing design. It is expected, based upon observed opacity sustained Baffle Out temperatures both simulated and measured, that this configuration also superior in reduction of PM emissions compared to the other configurations and the original design.

Chapter 7: Concluding Remarks

7.1 Wood Combustion

After a thorough but far from exhaustive discussion of wood structure, chemistry, and its combustion it should be evident to the reader that the study of wood combustion is far from mature despite its legacy as one of man's oldest technologies. Despite the discrepancy between benchmark modeling techniques, the largest source of modeling error throughout this study are the approximations made with respect to wood combustion. The dynamics do not lend themselves well to time averaging of experimental quantities nor does the fuel to chemical approximations of its structure and resulting thermal degradation. Techniques and approximations were adopted from the current literature, often in good agreement with test data, however must question if it is even indeed possible to have a comprehensive model of wood combustion.

While we did not focus strongly on the topics, PM formation and oxidation are also not mature fields. Benchmark modeling results of BC PM emissions grossly underestimated PM emissions, thus the reduction in PM emissions was attacked mostly through the proxy metrics of combustion efficiency, by virtue of temperature, species concentrations, reaction rates, or metrics of mixing. As a portion of the potentially unattainable comprehensive wood combustion model, OC PM formation and oxidation are very sensitive to pyrolysis rates, temperatures, wood composition, and moisture content. Only through recent innovative optical techniques has the study of the OC PM itself brought to light details about its morphology, chemical composition, and physical behavior.

Acknowledging the current theoretical and analytical barriers to a complete understanding of wood combustion, if renewable energy is to be taken seriously and locally generated, this subject will continue to be ripe for discoveries and breakthroughs.

7.2 CFD Simulation

The benchmarking analysis was as much to determine an acceptable method to model the Model 100 OWHH as it was a comparative analysis of CFD simulation techniques. The fluid mechanics of buoyant diffusion flames requires great care when CFD

modeling, however the large domain and varied geometry of an OWHH requires a compromise between accuracy and computational cost. The 10 runs performed were done so to directly compare several methods of simulation: 2D vs. 3D, steady state vs. transient, a surrogate fuel vs. a mixture based fuel, equilibrium vs. flamelet mixture fraction modeling, mixture fraction combustion vs. finite rate/eddy dissipation chemistry modeling, fixed mass flux vs. a pyrolysis algorithm based boundary conditions, and k-ε vs. LES.

Analysis and observations provided boundary conditions and results showed mixed agreement with test data. Combustion efficiency was consistently overestimated in the form of higher flame temperatures and lower CO emissions. While there was no direct superiority of one method over another, LES coupled with finite rate/eddy dissipation modeling resulted in the solution with the best agreement with internal temperatures and was naturally effective in capturing the characteristic large scale rotational structures seen in buoyant plumes. Concluding this benchmarking study is a summary table outlining the pros and cons of each model run, and may prove useful beyond the CFD simulation of OWHH operation in addition to simulation techniques discussed throughout this chapter.

7.3 OWHH PM Emission Reductions and Further Recommendations

In one way this study succeeded in its primary goal rather abruptly, in the reduction of PM emissions to meet the EPA Phase 1 emissions level of 0.6 lb PM/MMBtu from the Model 100. Benchmark analysis of test data suggested a $\varphi < 1.0$ during peak pyrolysis and operational modification simulation coupled with certified cordwood testing showed that operating at $\varphi < 1.0$ for the test duration reduces PM emissions to compliant levels, thus certifying the Model 100. However, as goes the law of unintended consequences, stack temperatures rose, burn rates increased, and subsequently efficiencies dropped.

A cribwood test with the same increase in φ was performed, and while CO emissions reduced and heating rates increased, the burn rate skyrocketed and PM emissions increased from the previous non-compliant weight by 40.4%. The low hanging fruit was picked, however the true issue with this OWHH was magnified, its worsened fuel and oxidizer mixing. The key problems to be readily addressed in physical modifications were: lengthening and segregating a post-combustion zone where high temperatures could be maintained for post-flame mixing and PM burnout. Part of the additional space was

obtained by generating a more compact, more efficient heat exchanger design. A feedback mechanism was observed in which additional air placed on the wood bed led to an increased burn rate, which in turn shortened burn time, reduced efficiency, and harmed post-flame mixing. The solution was to split air injection, which placed reduced air on the bed and added air above the flame to provide burnout without accelerating bed combustion. This design allowed the enhancement of post-combustion mixing through the use of baffles and secondary air jet placement. Through an iterative (and often overlapping) analysis, simulation, and experimentation cycle, an optimal design including impaction style baffles and secondary jet placement within the gaps was selected.

If this selected physical modification or something like it is put into a production unit, several items must be addressed:

(1) The airbox air must be reduced to a minimum acceptable level of injection/mixing to increase efficiency via decreased dilution.

(2) This maintained split of airbox and firebox air was only possible through use of dedicated blowers. Rather than tune the delivery system and fan for an intended split, staged combustion might be achieved through use of an airbox blower and exposed natural draft firebox inlets. Testing of configuration 2 resulted in a $\varphi_{firebox}$ of 0.844, which is near that of the benchmark peak pyrolysis seen in Figure 4.5.

(3) While not addressed by this study due to limitations in allowable physical changes, the firebox air delivery should be more symmetrical with respect to the wood load.

7.4 Final Thoughts

Use of OWHHs for clean domestic sources of heat, and potentially power, is a viable alternative energy source that is currently available. This study has shown the ways in which these systems can achieve reduced emissions, both in typical (cordwood) and certification (cribwood) applications. The successful management of the pyrolysis rates via metered firebox air and improvements in post-combustion PM and CO oxidation required a combined pollution prevention and mitigation strategy. In addition, this study has shown the success in application of commercial CFD software to non-traditional applications. While many of the models and techniques used are validated against and better suited for

well-defined CH_4 turbulent jet flames, the simulations of this study have proven remarkably versatile to be applied to the chaotic and primordial phenomena that is a wood fire.

Bibliography

1. Adanez, J.; de Diego, L. F.; Garcia-Labiano, F.; Abad, A.; Abanades, J. C.; *Ind. Eng. Chem. Res.*, **2001**, *40*, 4317-4323.

2. Afgan, N. H.; Beer, J. M editors, *Heat Transfer in Flames*. Scripta, Washington DC, 1974.

3. Andrae, M. O.; Gelencser, A; *Atmospheric Chemistry & Physics*. **2006**, *6*, 3131-3148.

4. Bai, X.S., Griselin, N.; Klason, T.; Nilsson, J.; *CFD Modeling of Biomass Combustion in Small-Scale Boilers - Final Report*; Division of Fluid Mechanics, Department of Heat and Power Engineering, Lund Institute of Technology, Lund, Sweden, 2002.

5. Bain, R.L.; Amos, W.A.; Downing, M.; Perlack, R.L.; U.S. Department of Energy, National Renewable Energy Laboratory, *Biopower Technical Assessment: State of the Industry and Technology*, 2003.

6. Bilger, R.W.; *Combustion Science and Technology*, **1976**, *13*, 155-170.

7. Bhaskar Dixit, C.S.; Paul, P.J.; Mukunda, H.S.; *Biomass and Bioenergy*, **2006**, *30*, 684-691.

8. Bourne Jr., Joel K. *Green Dream*, National Geographic, October 2007

9. Bura, Renata. PSE 406 Class notes Fall 2007: used with permission.

10. Burke, S.P.; Schumann, E.W.; *Combustion Symposium, Industrial and Engineering Chemistry*, **1928**, *20*, 998-1004.

11. California Climate Action Registry *Appendix to the General Reporting Protocol: Power Utility Reporting Protocol,* April 2005, pg 17.

12. Çengel, Y.A.; Boles, M.A.; *Thermodynamics: An Engineering Approach*, 4th Ed. McGraw-Hill: San Francisco, CA, 2002.

13. Cheremisinoff, P.N.: Morresi, A.C.; *Air Pollution Sampling & Analysis Handbook*. Ann Arbor Science Publishers, Inc. Ann Arbor, MI. 1978.

14. Cooper, C.D.; Alley, F.C.; *Air Pollution Control*, 3rd Ed. Waveland Press, Inc. Prospect Heights, IL. 2002.

15. Cox, G.C. "Basic Considerations". *Combustion Fundamentals of Fire*. Ed. Cox, G.C. Academic Press, Inc: San Diego, CA, 1995.

16. Diamond, Jared. *Guns, Germs & Steel: The Fates of Human Societies*. W.W. Norton & Company, New York, NY, 1997.

17. Fernandez-Pello, A.C. "The Solid Phase". *Combustion Fundamentals of Fire*. Ed. Cox, G.C. Academic Press, Inc: San Diego, CA, 1995.
18. Ferziger, J. H.; Peric, M.; *Computational Methods for Fluid Dynamics*, 3rd Ed.; Springer: New York, NY, 2002.

19. Field, M. A., D. W. Gill, B. B. Morgan, P. G. W. Hawksley: *Combustion of Pulverized Coal*. The British Coal Utilization Research Association, Leatherhead, UK, 1967.

20. Fine, P.M.; Cass, G.R., Simonett, B.R.T.; *Environmental Science Technology*, **2001,** *35*, 2665-2675.

21. Fitzpatrick, E.M.; Ross, A.B., Bates, J.; Andrews, G.; Jones, J.M.; Phylaktou, H.; Pourkashanian, M.; Williams, A.; *Process Safety and Environmental Protection, Institution of Chemical Engineers*, **2007**, *85 (B5)*, 430-440.

22. *FLUENT 6.3 User's Guide*, 2006

23. Galgano, A; Di Blasi, C.; *Combustion & Flame,* **2004**, *139*, 16-27.

24. Galgano, A; Di Blasi, C.; Horvat, A; Sinai, Y; *Energy & Fuels*, **2006**, *20*, 2223-2232.

25. Galgano, A; Di Blasi, C.; *Progress in Computation Fluid Dynamics*, **2006**, *6*, Nos. 4/5, 287-302.

26. Glassman, I.G, *Combustion*; 2nd Edition. Academic Press: New York, NY, 1987.

27. Goos, A. W., "The Thermal Decompositoin of Wood" *Wood Chemistry,* Vol. II, ACS Nomograph Series No. 97, 2 Ed., Reinhold Pub. Co., New York (1952) PYROLYSIS BOOK

28. Gregory P. Smith, David M. Golden, Michael Frenklach, Nigel W. Moriarty, Boris Eiteneer, Mikhail Goldenberg, C. Thomas Bowman, Ronald K. Hanson, Soonho Song, William C. Gardiner, Jr., Vitali V. Lissianski, and Zhiwei Qin. http://www.me.berkeley.edu/gri_mech/

29. Hearth, Patio & Barbecue Association, http://www.hpba.org/uploads/pics/GenSys.jpg

30. Howard, J.B.; Williams, G. C.; Fine, D. H.; *14th Int'l Symposium on Combustion*. **1973,** 975.

31. Huttenen, M.; Saastamoinen, J.; Kilpinen, P.; Kjäldman, L.; Oravainen, H.; Boström, S.; *Progress in Computation Fluid Dynamics*, **2006**, *6*, Nos. 4/5, 200-208.

32. Incropera, F.P., DeWitt, D.P.; *Introduction to Heat Transfer*, 4th Ed.; John Wiley & Sons: New York, NY, 2002.

33. Janse, A.M.C.; de Jonge, H.G.; Prins, W.; van Swaaij, W. P. M.; *Ind. Eng. Chem. Res.* **1998**, *37*, 3909-3918.

34. Jones, W. F.; Whitelaw, J. H.. *Combustion and Flame,* **1982**, *48:1*, 26.

35. Kronenburg, A.; Bilger, R.W.; Kent, J.H.; *Combustion and Flame*, **2000**, *121,* 24-40.

36. Launder, B. E.; Spalding, D. B.; *Lectures in Mathematical Models of Turbulence. Academic Press*, London, England, 1972.

37. Magnussen, B.F.; Hjertager, B.H.; *16th International Symposium on Combustion*, *The Combustion Institute,* **1976**.

38. Muñiz, L.; Mungal, M.G; *Combustion & Flame.* **2001**, *126*, 1402-1420.

39. Northeast States for Coordinated Air Use Management (NESCAUM), *Outdoor Hydronic Heater Model Regulation*, January, 29, 2007.

40. Peters, M.S.; Timmerhaus, K. D.; West, R.E.; *Plant Design and Economics for Chemical Engineers*, 5th Ed. McGraw-Hill: New York, NY, 2003.

41. Peters, N. *Turbulent Combustion.* Cambridge University Press: Cambridge, UK, 2000.

42. Pope, S. B. *Turbulent Flows.* Cambridge University Press: New York, NY, 2000.

43. Puget Sound Clean Air Agency, http://www.pscleanair.org/airq/burnban/

44. Shafizadeh, F.; Chin, P. S.; "Thermal Deterioration of Wood." *Wood Technology: Chemical Aspects.* Ed. Goldstine, I.S. ACS Press, Washington DC, 1977.

45. Simmons, R.F. "Fire Chemistry." *Combustion Fundamentals of Fire.* Ed. Cox, G.C. Academic Press, Inc: San Diego, CA, 1995.

46. Tesner, P. A. Snegiriova, T. D., and Knorre, V. G.: *Combustion and Flame.* **1971**, *17*, 253.

47. Tieszen, S. R, *Annual Review of Fluid Mechanics.* **2001**, *33*, 67-92.

48. Tillman, D.A.; Rossi, A.J., Kitto, W.D.; *Wood Combustion: Principles, Processes, and Economics*; Academic Press: New York, NY, 1981.

49. Turns, S.R.; *An Introduction to Combustion*, 2nd Ed.; McGraw Hill: Boston, MA, 2000.

50. U.S. Department of Commerce, National Institute of Standards & Technology, *Fire Dynamics Simulator Version 4: Technical Reference Guide*, 2006.

51. U.S. Department of Energy, Energy Information Administration, *A Look at Residential Energy Consumption in 2001*, 2001

52. U.S. Department of Energy, Energy Information Administration http://www.eia.doe.gov/cneaf/solar.renewables/page/trends/table11.html

53. U.S. Department of Energy, Office of Biological and Environmental Research & Office of the Biomass Program, *Breaking the Biological Barriers to Cellulosic Ethanol: A Joint Research Agenda*, 2006.

54. U.S. Environmental Protection Agency, *Method 5G: Determination of Particulate Matter Emissions from Wood Heaters (Dilution Tunnel Sampling Location)*

55. U.S. Environmental Protection Agency, *Test Method 28: Measurement of Particulate Emissions and Heating Efficiency of Outdoor Wood-Fired Hydronic Heating Appliances*

56. Welker, J.R.. "The Pyrolysis and Ignition of Cellulosic Materials: A Literature Review." *Pyrolysis of Polymers: Volume 13 Fire and Flammability Series* Ed. Hilado, C.J.. Technomic Publishing Co.: Westport, CT, 1976.

57. Wheeler, Elisabeth. Dept. of Wood and Paper Science, North Carolina State University, http://legacy.ncsu.edu/classes/wps202002/intro/wood.html

Appendix A

General Fuel Chemistry Calculation

Goal: Calculate amount of air delivered to firebox based upon a generic fuel composition and measured CO_2 and CO dry gas compositions.

Generic Reaction (with CO):

$$C_wH_xN_yO_z + \overline{MC}H_2O_{(\ell)} + \omega(O_2 + 3.76N_2) \Rightarrow \alpha CO_2 + (w-\alpha)CO + \left(x/2 + \overline{MC}\right)H_2O + (y/2 + 3.76\omega)N_2$$

Equation A.1

after O atomic balance: $\omega = \frac{1}{2}(\alpha + w + x/2 - z)$

Note: for stoichiometric conditions without CO, $w = \alpha$ and the stoichiometric coefficient of O_2 is $\omega^* = \frac{1}{2}(2w + x/2 - z)$.

Excess Air Generic Reaction:

$$C_wH_xN_yO_z + \overline{MC}H_2O_{(\ell)} + \Theta\omega(O_2 + 3.76N_2) \Rightarrow \alpha CO_2 + (w-\alpha)CO + \left(x/2 + \overline{MC}\right)H_2O + (y/2 + 3.76\Theta\omega)N_2 + \beta O_2$$

Equation A.2

after O atomic balance: $\beta = \frac{1}{2}(\Theta - 1)(\alpha + w + x/2 - z)$

Dry Exhaust Gas Mole Fractions:

$$y_{CO_2} = \frac{\alpha}{w + y/2 + (2.38\Theta - 1/2)(\alpha + w + x/2 - z)}$$ Equation A.3

$$y_{CO} = \frac{w - \alpha}{w + y/2 + (2.38\Theta - 1/2)(\alpha + w + x/2 - z)}$$ Equation A.4

algebraically solving both mole fractions for α:

$$\frac{y_{co_2}\left[w+y/2+(2.38\Theta-1/2)(w+x/2-z)\right]}{1-y_{CO_2}(2.38\Theta-1/2)}=\frac{y_{co}\left[w+y/2+(2.38\Theta-1/2)(w+x/2-z)\right]-w}{-1-y_{CO}(2.38\Theta-1/2)}$$

Θ is now determined in terms of known quantities, along with the stoichiometric coefficients of the chemical equation above. With respect to true stoichiometry, without exhaust CO, the molar equivalent ratio φ is defined as:

$$\varphi=\frac{\Theta\omega}{\omega^*} \qquad \text{Equation A.5}$$

Appendix B

Energy Balance of Model 100

Goal: Derive an analytical approach to assessing the performance of the OWHH. This analysis will provide internal boundary conditions and serve as a rule-of-thumb for analysis of CFD results. This Appendix will focus on use of preliminary results, however the same method is to be applied to further studies.

Note that for consistency in equation reporting, $q \equiv$ [kJ/kg] and $\dot{Q} \equiv$ [W].

B.1 Internal Heat Transfer

Internal locations of the Model 100 are labeled as follows, reproduced from Chapter 3:

Figure B.1: Labels of Thermocouple Locations

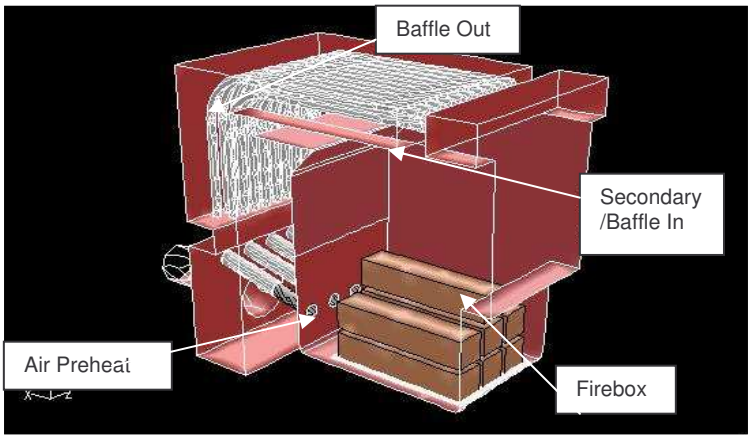

The quantities measured during testing to be used are the CO and CO_2 dry gas stack concentrations (used to generate stoichiometric coefficients and mass air-to-fuel ratio from Appendix A), $T_{firebox}$, T_{2ndry}, T_{stack}, P_{stack} (static), and Δm_{tot}. The planar areas at the outlet and the prior to the tube bank are 0.0324 m^2 and 0.1006 m^2 respectively.

The total mass flow through the system is calculated at the stack, using the average velocity from the turbulent Poiseuille flow relationship [41]. The stack diameter, static pressure drop, and section length are known. The viscosity is approximated with Sutherland's equation for N_2, seen in equation B.2 with T_{ref} = 288 K and μ_{ref} = 1.711E-5 kg/m-s. Lastly, the total system mass flow the averaged face velocity, cross-sectional area, and the local density of the stack, found assuming ideal gas behavior with an the assumed molecular weight of N_2, the measured stack temperature, and the measured stack static pressure as shown in equation B.3. Assuming steady state behavior, the face velocity through the 'secondary' plane, just prior to the tube bank, may be calculated seen in equation B.4, using the same assumptions and analogous measured quantities.

$$u_{avg,stack} = \left[\frac{D\Delta p}{0.0158 L \rho} \left(\frac{\rho D}{\mu} \right)^{1/4} \right]^{-4/7} \qquad \text{Equation B.1}$$

$$\mu = \mu_{ref} \left(\frac{T}{T_{ref}} \right)^{3/2} \frac{T_{ref} + 107}{T + 107} \qquad \text{Equation B.2}$$

$$\dot{m}_{tot} = \left(\rho u_{avg} A \right)_{stack} \qquad \text{Equation B.3}$$

$$u_{2ndry} = \frac{\dot{m}_{tot}}{(\rho A)_{2ndry}} \qquad \text{Equation B.4}$$

The tube banks are to be broken into two distinct zones based upon simplified convective heat transfer, the cross flow zone and the parallel flow zone. Convective heat transfer will be calculated with cross flow over a staggered tube bank and parallel flow over a flat plate respectively. The cross flow zone will be the exposed region directly above the firebox, extending 16" from the hot side manifold. The remaining portion of the tube bank will be the parallel flow zone. While it is a gross approximation that the flow will be purely perpendicular and then instantaneously purely parallel to the tube bank, this allows for ease of estimation.

For exterior cross-flow over a staggered tube bank, the Reynolds number is calculated using the maximum velocity, which is determined by equation B.5 [32] as a function of the external tube diameter and distance between the tube centerlines. The tube

bank within the Model 100 has spacing of one tube diameter laterally and depth wise, thus the maximum velocity is twice the far field velocity.

$$u_{\max} = \frac{S_T}{S_T - D} u_{2ndry} = 2u_{2ndry} \qquad \text{Equation B.5}$$

$$\mathrm{Re}_{D,\max} = \frac{u_{\max} D}{\nu_{cross}} \qquad \text{Equation B.6}$$

To determine the external heat transfer coefficient h, the average Nusselt number as a function of the Reynolds and Prandtl numbers, valid for $1{,}000 < \mathrm{Re}_D < 20{,}000$, $0.7 < \mathrm{Pr} < 500$, is calculated per equation B.7. The Prandtl number is defined in equation B.8. The coefficients are for a bank of two rows deep and Pr_s is the Prandtl number at the tube surface [32]. The convective heat transfer coefficient is determined per equation B.9.

$$\overline{Nu}_D = (0.76)(0.35)\,\mathrm{Re}_{D,\max}^{0.6}\,\mathrm{Pr}^{0.36}\left(\frac{\mathrm{Pr}}{\mathrm{Pr}_s}\right)^{1/4} \qquad \text{Equation B.7}$$

$$\mathrm{Pr} = \frac{\nu}{\alpha} \qquad \text{Equation B.8}$$

$$h_{cross} = \frac{\overline{Nu}_D k_{cross}}{D} \qquad \text{Equation B.9}$$

The radial heat flux (W/m^2) of the cross-flow portion, assumed to be constant throughout this section, is determined from a 1-D radial convective and conductive combined resistance for a single tube, in equation B.10.

$$\dot{Q}_r'' = \frac{T_{2ndry} - T_{H_2O}}{\frac{1}{2\pi r_i L h_{H_2O}} + \frac{\ln r_o / r_i}{2\pi k_{pipe} L} + \frac{1}{2\pi r_o L h_{cross}}} \qquad \text{Equation B.10}$$

The heat transfer coefficient for the water flow, which is typically at 10 gallons per minute through the 19 tubes, is assumed to be laminar. At the assumed fully developed flow

and constant external, thus internal, temperatures, the average Nusselt number relation for water is $\overline{Nu}_D = 3.66$. As properties for water vary little between the typical hot and cold side of the internal loop, between 40°C and 70°C, the average heat transfer coefficient for the water will be calculated from the hot side, where the initial heat extraction occurs, at $h_{H2O} = 128.2\ W/m^2K$. The cross flow surface temperature via the convective heat transfer equation B.11 is determined. From this surface temperature, the total convective heat transfer may be calculated in equation B.12. As the exposed cross flow tubing experiences surface radiation that is non-negligible, but small compared to convection, the total heat transfer contains a radiation component.

$$T_{s,cross} = T_{2ndry} - \frac{\dot{Q}_r''}{2\pi r_o L h_{cross}} \qquad \text{Equation B.11}$$

$$\dot{Q}_{cross} = h_{cross} A_{cross,tot} \left(T_{2ndry} - T_s\right) + \varepsilon\sigma A_{cross,tot} \left(T_{2ndry}^4 - T_s^4\right) \qquad \text{Equation B.12}$$

From the methods of Appendix A, the stoichiometric coefficients of the dry gas species: N_2, O_2, CO, and CO_2 are found along with the instantaneous mass air-to-fuel ratio. To determine the temperature entering the parallel flow region, a mixture based C_p is found based upon the calculated dry mole fractions of CO, CO_2, O_2, and N_2, third order polynomial fit C_p coefficients [12], and the average molecular weight in equation B.13. The coefficients of the C_p polynomial for said gaseous species are outlined in Table B.1, which are of the form $C_{p,i} = a + bT + cT^2 + dT^3$ [kJ/kmol K].

$$T_{par} = T_{2ndry} - \frac{\dot{Q}_{cross}}{\dot{m}_{tot}\left(C_{p,avg} \big/ MW_{avg}\right)_{cross}} \qquad \text{Equation B.13}$$

Table B.1: Coefficients for C_p Calculation [12]

Coefficient\Specie	CO2	CO	H2O	N2	O2
a	22.26	28.16	32.24	28.9	25.48
b	0.05981	0.001675	0.001923	-0.00157	0.0152
c	-3.5E-05	5.37E-06	1.06E-05	8.08E-06	-7.2E-06
d	7.47E-09	-2.2E-09	-3.6E-09	-2.9E-09	1.31E-09

To determine the parallel flow Reynolds number for the flat plate approximation, equation B.14 is used. Assuming that the parallel flow along the flat plate is laminar, the average Nusselt number is found with equation B.15 [32].

$$\mathrm{Re}_L = \frac{u_{2ndry} L}{\nu_{par}} \qquad \text{Equation B.14}$$

$$\overline{Nu}_L = (0.664)\,\mathrm{Re}_L^{0.5}\,\mathrm{Pr}^{1/3} \qquad \text{Equation B.15}$$

The total convective heat transfer of the parallel flow portion is found identically to that of the cross flow portion from this point: determining h_{par} as in equation B.9, $\dot{Q}_L^{"}$ is calculated using the cold side T_{H2O} as in equation B.10, the surface temperature for the parallel regime is determined similarly from equation B.11, finally leading to $\dot{Q}_{par}$ as calculated in equation B.12 without a radiation component. As the parallel flow region is not exposed to the firebox, and also is constricted by insulation and tight geometry, radiation is not expected to contribute significantly to $\dot{Q}_{par}$. The total heat transfer to the internal loop will be the sum of $\dot{Q}_{cross}$ and $\dot{Q}_{par}$, which is a conservative estimate.

B.2 First Law Energy Budget

An idealized first law energy budget of the OWHH, assuming steady state behavior and thermodynamic and chemical equilibrium, is approximated visually by the cartoon in Figure B.2 reproduced from Chapter 4. The material flows are indicated by the arrows and external heat flows are indicated by the curved lines. Internally, the heat of reaction is a source and the heats of pyrolysis and drying are treated as sinks. No work is performed by the OWHH. The resulting energy balance is shown in equation B.16.

Figure B.2: Cartoon of OWHH Energy Budget

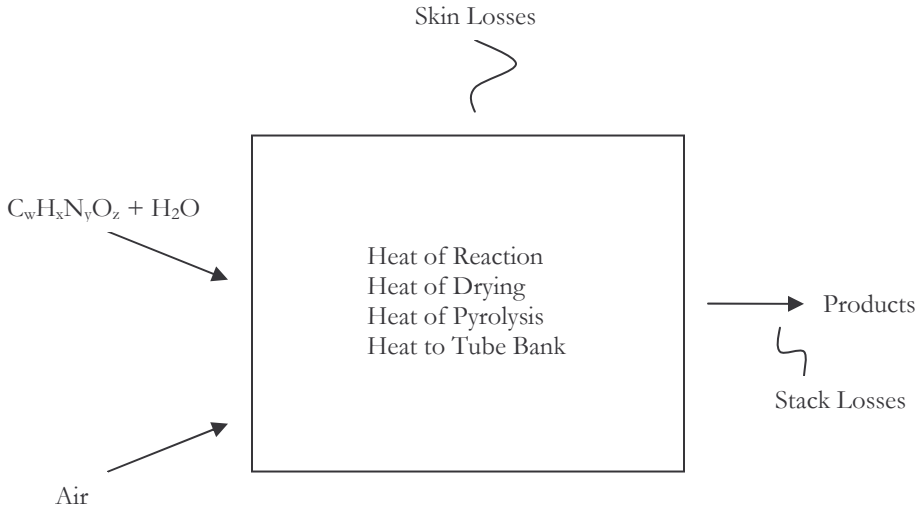

$$\dot{Q}_{rxn} = \dot{Q}_{stack} + \dot{Q}_{skin} + \dot{Q}_{dry} + \dot{Q}_{pyr} + \dot{Q}_{loop} \qquad \text{Equation B.16}$$

B.2.1 Heat of Reaction

To determine the heat of reaction, the overall chemistry is modeled by equation A.2. From the stochiometric molar coefficients determined via Appendix A, q_{rxn} is then determined by equation B.17 on a per 100 kg wet wood basis. Heats of formation for the gaseous species [12] and the heat of formation for wood [5] are found in the literature. The wood enters the system at the observed Firebox temperature and the air enters the system at an observed preheated air temperature of 650 K. The firebox of the OWHH is assumed to be at atmospheric pressure. The instantaneous burn rate is determined by creating a trendline for the scale readings throughout the test, which is the mass loss of wet wood, denoted as $\dot{m}_{wet}$. From $\dot{m}_{wet}$, we may determined the total heat of reaction, $\dot{Q}_{rxn}$, with equation B.18.

$$q_{rxn} = q_p - q_r = \sum N_p\left(\bar{h}_f^o + \bar{h} - \bar{h}^o\right)_p - \sum N_r\left(\bar{h}_f^o + \bar{h} - \bar{h}^o\right)_r \qquad \text{Equation B.17}$$

$$\dot{Q}_{rxn} = (1000)\dot{m}_{wet}q_{rxn}/100 \qquad \text{Equation B.18}$$

A variable C_p approach is used to compute the sensible heat, using third order polynomials for each species as used previously. The range of C_p over the expected firebox and stack temperatures of observed tests is between 400 K < T < 950 K (≈ 250°F < T < 1,250°F). The variability of C_p over this range for the species of interest is shown in Figure B.3. The variability is acceptable for the expected accuracy of this analysis.

Figure B.3: C_p Variability Over Observed Firebox & Stack Temperature Range

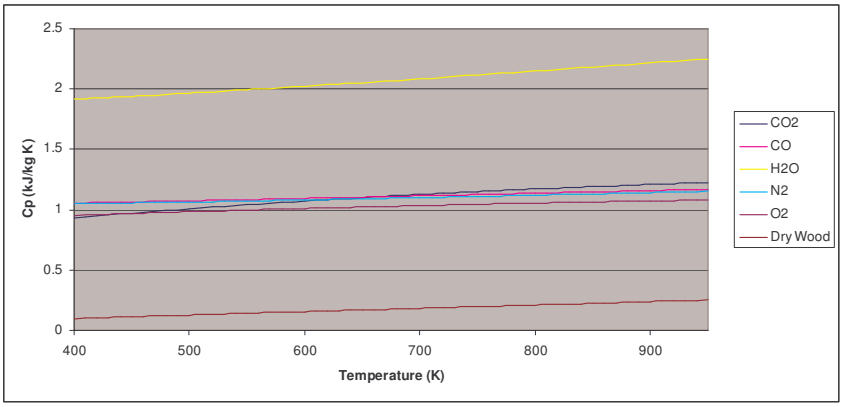

B.2.2 Stack and Skin Losses

The heat loss at the stack, $\dot{Q}_{stack}$, the heat released when the products are brought down to the ambient temperature. This idealized ambient state is denoted as q_∞, and is characterized by complete combustion (no CO present) and liquid water at the ambient temperature. The stack losses are calculated as shown in equation B.19.

$$\dot{Q}_{stack} = (1000)\dot{m}_{wet}(q_p - q_\infty)/100 \qquad \text{Equation B.19}$$

Skin losses are determined using free convection relationships and the radiation equation 2.20, measured surface temperatures, and the ambient temperature. The individual skin losses are calculated for each exterior face: the front or door side, the back side, the top, and the left and right from the perspective of the front side. The skin losses are approximated by Nusselt numbers calculated as empirically based functions of the Grashof number, which is defined in equations B.20, and the Prandtl number. The Grashof number

contains the volumetric thermal expansion coefficient, β, which is defined as T^{-1} for ideal gases. The Nusselt number relationship for an upper-surface horizontal heated plate is used for the top side and a vertical heated plate is used for the remaining faces, outlined in equations B.21 and B.22 respectively [32]. The characteristic dimension L is the longest length of each respective plate.

$$Gr_L = \frac{g\beta(T_s - T_\infty)L^3}{\nu^2} \qquad \text{Equation B.20}$$

$$\overline{Nu}_{L,vert} = \left\{ 0.825 + \frac{0.387(Gr_L \Pr)^{1/6}}{\left[1 + (0.492/\Pr)^{9/16}\right]^{8/27}} \right\}^2 \qquad \text{Equation B.21}$$

$$\overline{Nu}_{L,hor} = 0.15(Gr_L \Pr)^{1/3} \qquad \text{Equation B.22}$$

The heat transfer coefficients for the vertical and horizontal heated plates are determined in a similar fashion as equation B.9, and from which the skin loss for each side is determined as done in equation B.12. $\dot{Q}_{skin}$ is calculated as the sum of these individual heat losses.

B.2.3 Heat of Drying and Pyrolysis

The heat of drying and pyrolysis are necessary sinks to be included, which permit the release of the gas phase volatile species and are assumed to be functions of $\dot{m}_{wet}$ and internal temperatures only. While this assumption is expected to be reasonably accurate as the as drying and pyrolysis fronts are observed to move radially towards the center of a log at constant rates, as shown in Figure 2.11, it is expected to break down upon entering the char oxidation dominated portion of the burn. $\dot{Q}_{dry}$ is calculated as in equation B.23, which q_{dry} is from equation 2.3. $\dot{Q}_{pyr}$ is determined empirically as a function of the wet burn rate $\dot{m}_{wet}$, as in equation B.24 for C = 0.3 at peak pyrolysis [31].

$$\dot{Q}_{dry} = (1000) q_{dry} \dot{m}_{wet}$$ Equation B.23

$$\dot{Q}_{pyr} = 10^6 \dot{m}_{wet} / C$$ Equation B.24

B.2.4 Heat to Internal Loop

The heat transferred to the internal water loop is determined as a function of the hot and cold side measured temperatures and the volumetric flow rate. $\dot{Q}_{loop}$ is calculated per equation B.25, with temperatures in °F, flow rate in gallons per minute, and the correction factor of 500 for English to SI units and an assumed water density.

$$\dot{Q}_{loop} = (500) \dot{V} \left(T_{H_2O,hot} - T_{H_2O,cold} \right) \qquad \dot{V} = gpm, T_{H_2O} = °F$$ Equation B.25

Appendix C

Determination of k-ε Boundary Conditions

Goal: Determine boundary condition values for k and ε for the air inlets.

Underlying Theory:

The turbulent intensity and length scale for assumed fully developed duct flow is defined by the following empirical relationships [22], for L=D for round ducts:

$$\frac{u''}{u_{avg}} = 0.16(\mathrm{Re}_D)^{-1/8} \qquad \text{Equation C.1}$$

$$\ell = 0.07L \qquad \text{Equation C.2}$$

From these quantities, the estimated inlet turbulent kinetic energy and dissipation rate are found through the following relationships, for C_μ=0.09 [22]:

$$k = \frac{3}{2}\left[u_{avg}\left(\frac{u''}{u_{avg}}\right)\right]^2 \qquad \text{Equation C.3}$$

$$\varepsilon = C_\mu^{3/4}\frac{k^{3/2}}{\ell} \qquad \text{Equation C.4}$$

Appendix D

Graphics from Physical Modification Simulations

Figure D.1: Z O_2 Mole Fraction Contours for Configuration 1

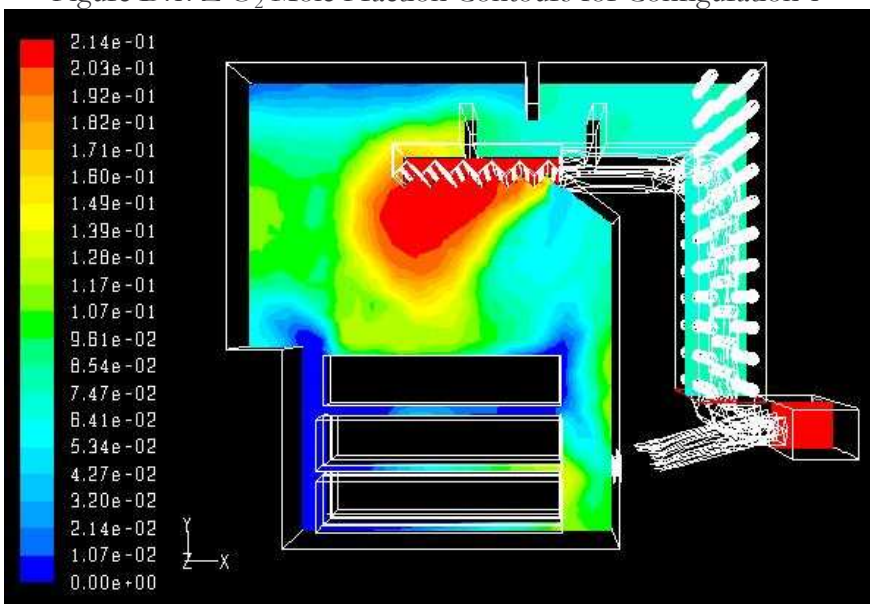

Figure D.2: Z O_2 Mole Fraction Contours for Configuration 2

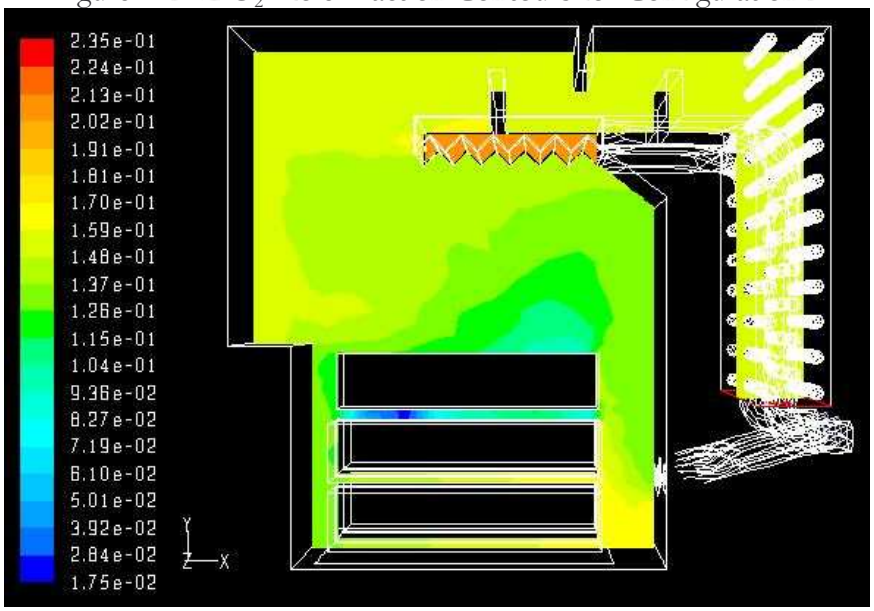

Figure D.3: Z O_2 Mole Fraction Contours for Configuration 3

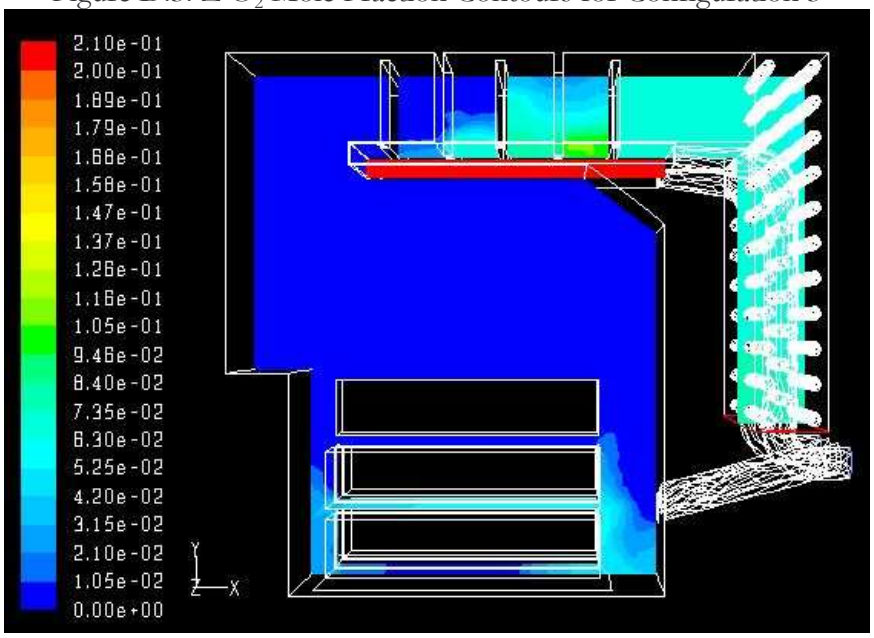

Figure D.4: Z Temperature (K) Contours for Configuration 1

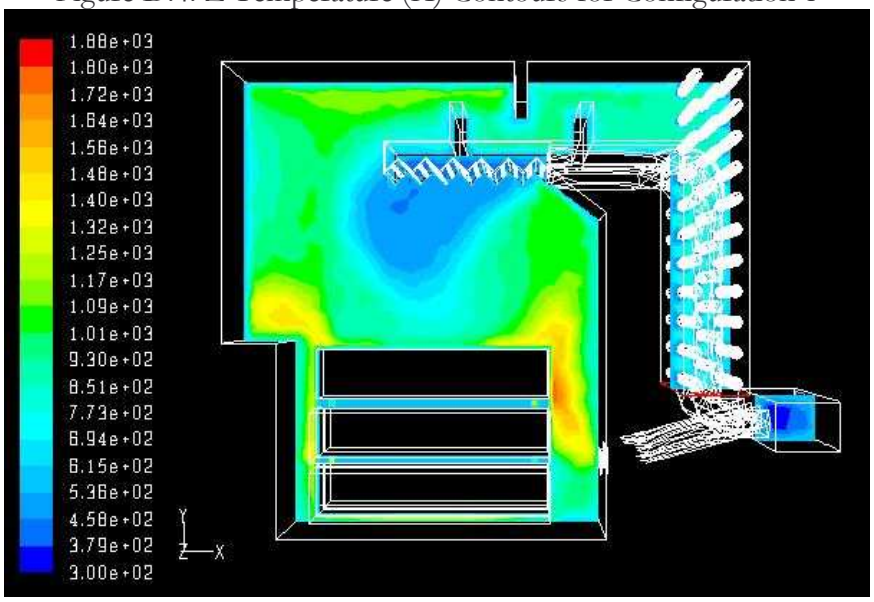

Figure D.5: Z Temperature (K) Contours for Configuration 2

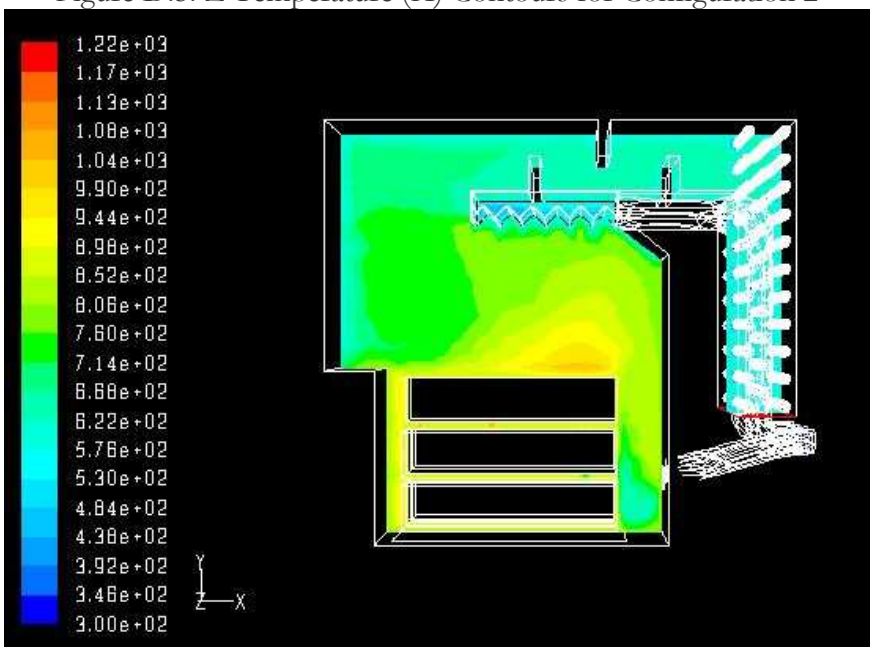

Figure D.6: Z Temperature (K) Contours for Configuration 3

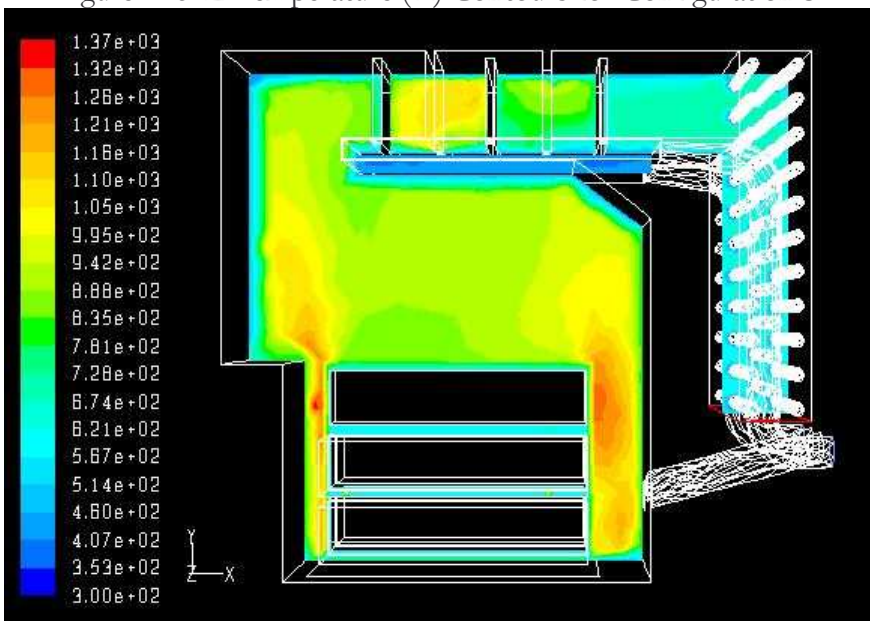

Figure D.7: Pathlines for Configuration 1

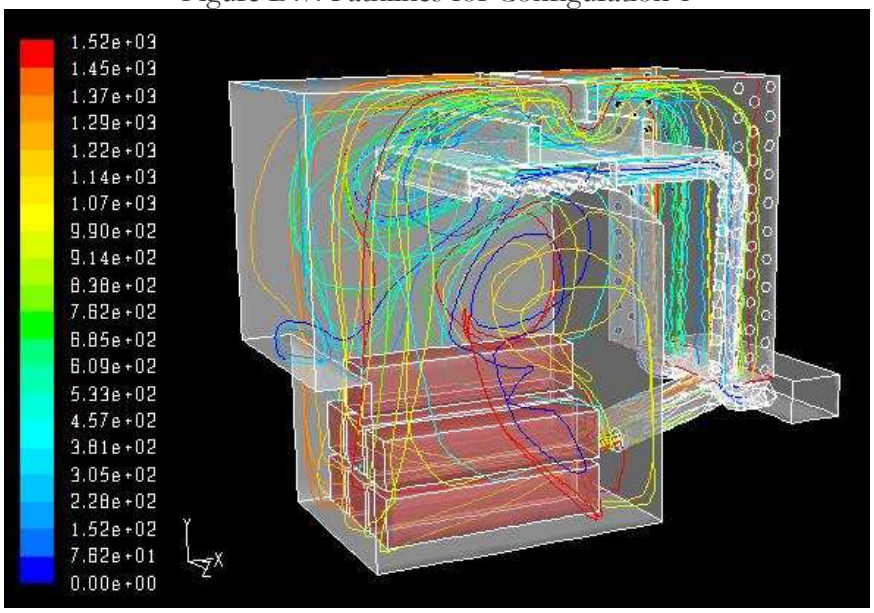

Figure D.8: Pathlines for Configuration 2

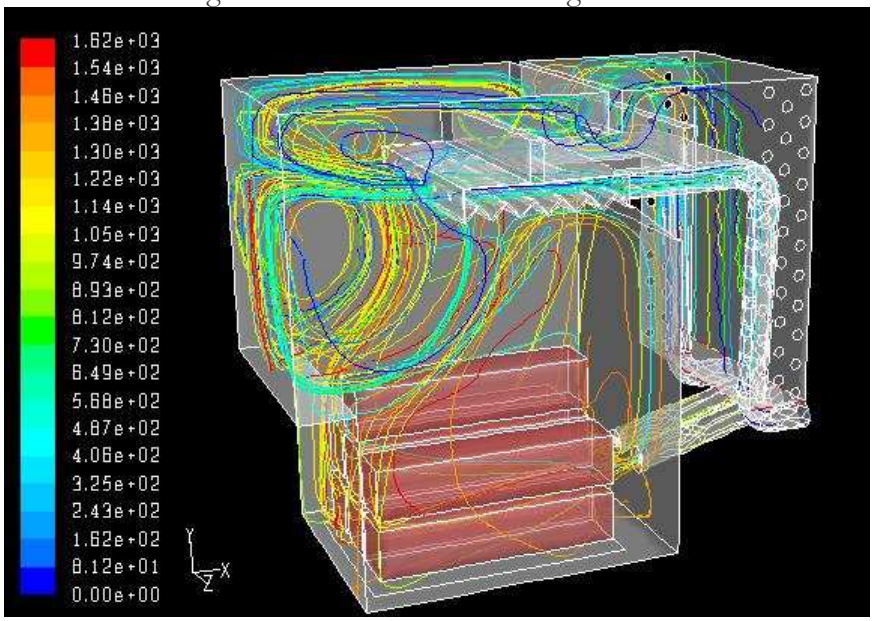

Figure D.9: Pathlines for Configuration 3